Important Notice

THE UNIVERSITY OF CALGARY

Three-component and three-dimensional seismic imaging

by

Shaowu Wang

A THESIS
SUBMITTED TO THE FACULTY OF GRADUATE STUDIES
IN PARTIAL FULFILMENT OF THE REQUIREMENTS FOR THE
DEGREE OF MASTER OF SCIENCE

DEPARTMENT OF GEOLOGY AND GEOPHYSICS

CALGARY, ALBERTA
AUGUST, 1997

THE UNIVERSITY OF CALGARY
FACULTY OF GRADUATE STUDIES

The undersigned certify that they have read, and recommend to the Faculty of Graduate Studies for acceptance, a thesis entitled "Three-component and three-dimensional seismic imaging" submitted by Shaowu Wang in partial fulfilment of the requirement for the degree of Master of Science.

Supervisor, Dr. D. C. Lawton
Department of Geology and Geophysics

Co-supervisor, Dr. J. C. Bancroft
Department of Geology and Geophysics

Dr. E. S. Krebes
Department of Geology and Geophysics

External Examiner, Dr. R. J. Torrence
Department of Mathematics and Statistics

Date

ABSTRACT

A fast 3-D converted-wave depth-variant common conversion point binning method was first developed for constant velocity medium and then modified for depth-variant velocity model. The new algorithm is fast while not losing the accuracy of the CCP binning. A 3-D converted-wave numerical model demonstrated its feasibility.

The prestack migration and migration velocity analysis provided a new approach to converted-wave (*P*-*S*) processing and imaging. In the prestack migrated CCSP gather, the asymmetry of the *P*-*S* ray path is "removed", therefore some conventional processes for *P*-*P* can be applied to *P*-*S* processing. The new approach is very fast, flexible and stable. The 3-D physical model and 2-D field data examples proved these features.

With the aid of a 3-D *P*-*S* physical modeling dataset, two processing flows for converted-wave were evaluated. One is the conventional converted-wave processing flow with CCP binning, *P*-*S* NMO and poststack migration. The other is the processing flow with converted-wave prestack migration.

ACKNOWLEDGMENT

I wish to express my sincerest gratitude to my supervisor, Dr. Don C. Lawton, who has from the very onset, been an immutable source of guidance and inspiration. I received from him valuable suggestions, candid appraisals and miscellaneous critiques which continually updated my standpoint and infused new ideas into my research work.

I would like to thank my co-supervisor Dr. John C. Bancroft for his guidance and counsel during the course of my work, especially in the work of converted-wave prestack migration and migration velocity analysis.

Unocal Canada Ltd. very generously donated the seismic data to the CREWES Project.

I am grateful to Dr. Rob R. Stewart for his suggestive discussions. I would like to thank Dr. Helen Isaac for her great help in the processing of the 3C-3D physical model data set.

I thank the members of The CREWES Project, especially Mr. Eric Gallant for his wonderful support in physical modeling, Mr. Henry Bland and Mr. Darren Foltinek for their helpful assistance in ProMax programming and other supports.

I am thankful to Mr. Mark Lane, a former member of The CREWES Project, for his great help and collaboration.

The financial support from the CREWES sponsors is very appreciated.

Finally, I like to express my special appreciation to my wife, Xiao-Fang Li, for her patience and encouragement.

TABLE OF CONTENTS

LIST OF TABLES

LIST OF FIGURES

LIST OF ABBREVIATIONS

2-D	Two-Dimensional
3-C	Three-Component
3-D	Three-Dimensional
3C-3D	Three Component and Three Dimensional
3C-2D	Three Component and Two Dimensional
ACCP	Asymptotic Common Conversion Point
AVE	Average
CCP	Common Conversion Point
CCSP	Common Conversion Scatter Point
CMP	Common Middle Point
CSP	Common Scatter Point
DMO	Dip Moveout
MMO	Migration to Multiple Offset
NMO	Normal Moveout
P-wave	Compressional Wave
S-wave	Shear Wave
P-P	From Incident *P*-wave to Reflected *P*-wave
P-S	From Incident *P*-wave to Reflected *S*-wave
RMS	Root Mean Square
V_p	*P*-wave Velocity
V_s	*S*-wave Velocity
V_{ps}	*P-S* converted-wave velocity
γ	Velocity Ratio of *P*-wave and *S*-wave
$\overline{\gamma}$	Average Velocity Ratio of *P*-wave and *S*-wave
TZO	Transformation to Zero Offset
VSP	Vertical Seismic Profile

Chapter 1 - Introduction

1.1 Background

Three-dimensional (3-D) seismic acquisition has been becoming an essential tool in seismic exploration and development in the last decade. Exploration companies have turned to the 3-D method to optimize investment and minimize risk (Buchanan, 1992). The interpretation of 3-D converted-wave (*P-S)* data can not only enhance the interpretation results of *P*-wave data, but can also provide independent information, such as another image of the subsurface, and illumination of an interface which may not have a *P*-wave velocity contrast, but which may have an *S*-wave velocity contrast. Including converted-wave data into our interpretation may lead to a fully integrated interpretation of structure, lithology, porosity and reduction in the risk of finding hydrocarbons (Tatham and Stoffa, 1976; Tatham, 1982; Tatham et al., 1983; Tatham and Goolsbee, 1984; Tatham and Stewart, 1993).

1.1.1 The difference between *P-P* and *P-S* data acquisition and processing

The acquisition, processing and interpretation of 3-D *P*-wave seismic data has been fully developed in recent years. However, for converted-waves, the 3-D processing flow is in early development. Because of the asymmetric characteristic of the *P-S* raypaths shown in Figure 1-1, its processing is much more difficult than the pure *P*-wave processing.

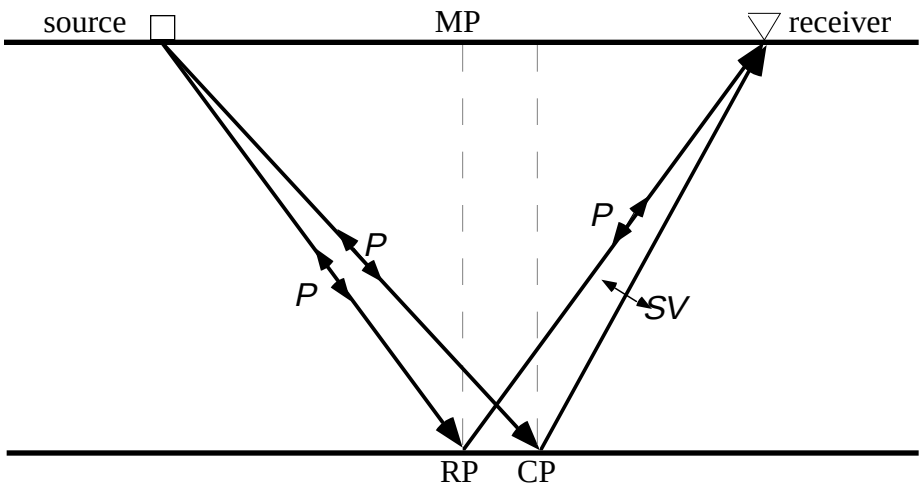

FIG.1-1. Diagram of *P-P* wave and *P-S* wave ray paths.
RP: *P-P* reflection point; CP: *P-S* conversion point

For an isotropic medium with a flat reflector, the *P-P* raypath is symmetric, whereas the *P-S* raypath is asymmetric due to the fact that the *S*-wave velocity is lower than the *P*-wave velocity. Moreover, their polarization directions are also different. The polarization direction of *P*-wave is in ray path direction and the polarization direction of *S*-wave is perpendicular to the ray path. Hence, for 3-D and three-component (3-C) data acquisition, not only the vertical component, but also the in-line (receiver-line) and cross-line (shot-line) horizontal components are recorded, in order to obtain radial and transverse components with respect to the source-receiver azimuth. For conventional *P-P* recording, source-receiver offsets can be from zero-offset to reasonably large offsets, but for mode-converted waves, data with moderate offsets are most useful (Lawton, 1993), according to the principle of partitioning of wave energy on a reflector. After data have been collected from a field survey or from a physical modeling experiment, correct processing procedures (or flow) are important to obtain the optimum image of the subsurface. Due to the asymmetry of *P-S* raypaths, data acquisition and processing for *P-S* data differ from that for pure *P*-wave data.

The key step in 3-D *P-S* data processing is the concept of common conversion point (CCP) binning. Asymptotic CCP stacking and depth-variant CCP stacking for 2-D converted-wave surveys have been developed by the CREWES Project in recent years (Eaton and Stewart, 1989). For 3-D converted-wave surveys, azimuth has to be taken into account in CCP binning. In order to enhance *P-S* wave energy and improve signal-to-noise ratio to obtain good stacked data, component rotation (Lane et al., 1993), converted-

wave NMO (Slotboom et al, 1990) and modal separation of *P-P* wave energy and *P-S* wave energy (Dankbaar, 1985; Lane et al., 1993) are applied.

1.1.2 Comparison between physical and numerical modeling

Physical modeling and/or numerical simulation are often used to evaluate the feasibility of experimental design and data processing without the cost of field acquisition (Chen and McMechan, 1993; Ebrom et al., 1990; Chon and Turpening, 1990). Physical modeling is a very useful way to evaluate experimental design, data processing algorithms and interpretation methods in that the model and acquisition geometry are controlled, yet the data have many of the characteristics of field data (Chen and McMechan, 1993). In physical modeling, discretization in numerical modeling is not needed, approximations and assumptions may be avoided, and roundoff errors do not accumulate. Furthermore, compared to numerical modelling methods, physical models suffer from all of the experimental errors that plague actual field work, such as positioning uncertainties, dynamic-range limitations and undesired (but real) interfering events (Ebrom et al., 1990).

1.1.3 Review of converted-wave CCP binning

In the implementation of 3-D converted-wave data processing flow, some algorithms have to be developed. Among them is the common conversion point (CCP) stacking or binning. Lane and Lawton (1993) have developed a 3-D asymptotic CCP algorithm. For both 2-D and 3-D converted-wave CCP binning methods, although asymptotic CCP binning is simple and fast, it is only a first-order approximation of the true conversion point. Conventional binning parameters for asymptotic CCP binning lead to periodicities in both offset and fold (Eaton et al., 1990). Furthermore, when the source line interval is an integer multiple of the group interval multiplied by the average V_P/V_S ratio, empty bins occur. Although the choice of an optimum bin size can solve this problem, these bins are always larger than conventional bins with a size of half the group interval (Lawton, 1993). Tessmer and Behle's (1988) depth-variant CCP binning method is accurate for a simple horizontally layered medium. However, because the calculation is complicated and must be done for each binned time sample, the method is very time-consuming. A generalization of Tessmer and Behles's method was described by Taylor (1989) to take into count of the source and receiver elevations or depths. Therefore, the method is also suitable to Vertical Seismic Profile (VSP) CCP binning or stacking.

To speed up Tessmer and Behle's depth-variant CCP binning algorithm, Zhong et al. (1994) proposed a so-called one step CCP stacking technique. They claim that the

technique enables the accomplishment of reflection point migration, non-hyperbolic moveout and CCP stacking in one step. It is actually no more than another approach of depth-variant CCP stacking. They pre-calculate the horizontal distances (D) of the conversion points to the source-receiver midpoints for the given offset bins, and all of the time samples at the given velocity (*P-P* and *P-S* waves) control points and store them in an interpolation table. In the implementation of CCP stacking, for a given input trace, D value for each time sample is obtained by looking up the interpolation table. In some situations, this algorithm can speed the depth-variant CCP stacking processing, but in 3-D case, if the number of velocity control points, the number of offset bins and the number of samples are large, the algorithm needs very large computer memory to store the pre-computed table and the 3-D interpolation is also very slow. The size of the interpolation table can be reduced by increasing the offset bin spacing, but this is at the expense of reducing the CCP stacking accuracy.

1.1.4 Conventional 3C-3D prestack imaging

In order to get an optimum image of the subsurface structures using converted-waves, another important process is converted-wave migration and migration velocity analysis. Migration in general is a process that attempts to reconstruct an image of the original reflecting structure from energy recorded on input seismic traces. Prestack migration is a direct process that moves each point sample into all the possible reflection positions, and invokes the principles of constructive and destructive interference to recreate the actual image. An alternate description of the migration process starts by selecting an output migrated sample. All input traces are searched to find energy that contributes to the output sample. This second description is the basic of Kirchhoff migration (Bancroft et al., 1995) .

The conventional procedure for converted-wave imaging is dip moveout (DMO), velocity analysis, normal moveout (NMO), CCP stacking and poststack migration (Harrison, 1992; Cary, 1994). Because of the difference between the *P-P* and *P-S* raypaths, DMO processing for converted-waves is much more complex than that for *P-P* waves and Kirchhoff-style DMO algorithm seems to be the only appropriate choice (Deregowski, 1982; Harrison, 1992). For *P-S* wave velocity analysis and normal moveout correction, a time-shifted hyperbolic moveout approximation has to be made (Slotboom et al, 1989, 1990).

To achieve the common reflection point stacking by DMO processing, the conventional approach is to apply DMO processing after NMO correction. But any velocity

error in NMO correction may affect the DMO processing results. This is why in 1986, Stolt expressed the desire for an operator "which migrates the unstacked data, but leaves NMO and stack alone". Due to this kind of motivation, Forel and Gardner (1987 and 1988) introduced a DMO-NMO algorithm for *P-P* data processing in a constant velocity medium. As the first step, the algorithm converts a given trace from two-way travel time (t), offset (2h) domain into (t_1, k) domain, in which t_1 is the transformation of time (t) and k is the transformed offset (2h). The calculation of k and t_1 are both velocity-independent and depth-independent. In (t_1, k) domain, the relationship between t_1 and k becomes hyperbolic even for the event from a dipping reflector. So the velocity analysis in (t_1, k) domain is dip-independent. It can be applied to any ensemble of traces no matter what the variations in azimuth and offset may be. Then, the zero offset trace is obtained by standard velocity analysis and stack. The amplitude preservation for this kind of DMO processing was also discussed by Gardner and Forel (1990). Because the calculations of t_1 and k are depth-independent and velocity-independent, the method is very fast. Only a bulk time shift and a re-assignment of transformed offset for a given input trace are needed to transform a trace from (t, 2h) domain into (t_1, k) domain. If the application of this method is followed by poststack migration, it is equivalent to prestack migration of any data set. The limitation of this algorithm is that it is accurate only for constant velocity model and the poststack migration is needed to migrate the seismic reflection to its true position.

The application of Gardner's method to 3-D data set, however, suffers from an irregular distribution of the traces within a CMP bin, due to the fact, that the velocity independent DMO operator in a constant velocity model is the same as that in the 2-D case, and the line segments from source to receiver, which intersect the bins, do not necessarily pass through the bin centers. So, Ferber (1994) used the similar "offset redefinition trick" to create data sets which mimic high fold, bin-center adjusted, field data sorted into common-midpoint gathers. This is the so-called migration to multiple offset (MMO) method. This algorithm is also velocity-independent, but it is a prestack time migration method and can be used to process any 2-D or 3-D data set. The migration velocity can be obtained by performing conventional velocity analysis to the MMO CMP gathers. This method is theoretically based on the same assumption as Gardner's DMO, i.e. the constant velocity model. This assumption is broken down if the spatial velocity variation becomes too severe.

Using the same principle introduced by Forel and Gardner (1988) for DMO processing of ordinary *P*-waves in a constant velocity medium, Alfaraj and Larner (1992) extended this method to converted-wave transformation to zero offset (TZO) processing.

In this method, the transformed offset k is the same offset-dependent parameter obtained by Forel and Gardner (1988) for ordinary waves, but the transformed time t_1 is velocity-dependent. This means the calculation of t_1 depends on the *P*-wave and *S*-wave velocities. For a constant velocity model, TZO for converted-waves has all of the advantages for *P*-wave processing. But for depth-variant velocity model, the computation of t_1 is not only velocity-dependent, but also depth (or time)-variant. Therefore, the algorithm may lose some advantages, such as simple and fast.

1.1.5 *P-P* prestack migration by equivalent offsets and CSP gathers

Prestack migration by equivalent offsets and common scatter point (CSP) gathers has already successfully been applied to *P-P* data processing (Bancroft, et al., 1994). CSP gathers are created for each migrated trace by replacing the common midpoint (CMP) gathers of conventional processing. Samples for each input trace are assigned an equivalent offset for each output scatter point position, then transferred into the appropriate offset bin of the CSP gather. By doing this, the prestack time migration is reduced to be a simple re-sort of the data into CSP gathers, and the velocity analysis on these CSP gathers becomes more effective, because the CSP gather has higher fold and a larger maximum offset than the conventional CMP gather has.

Prestack migration by equivalent offsets and common conversion scatter point (CCSP) gathers may be more attractive for 3-D converted-wave processing. After the *P-S* data are transformed into CCSP gathers by equivalent offsets, the asymmetry of the *P-S* ray paths is "removed", therefore, except all of the benefits of the prestack migration by equivalent offsets and CSP gathers in *P-P* data processing, this new algorithm can simplify the *P-S* data processing, and some algorithms, such as conventional NMO correction and semblance velocity analysis, can be applied to the CCSP gathered *P-S* data, and CCP binning is not necessary.

1.2 Objectives of the thesis

This thesis is concerned with developing processing algorithms for 3-D converted-wave data. A fast 3-D depth-variant CCP stacking method is implemented on synthetic and physical data. The algorithm is suitable to depth-variant velocity model with constant or slowly varying ratio of *P*-wave to *S*-wave velocities. A 3-D converted-wave prestack migration and migration velocity analysis by equivalent offsets and CCSP gathers is developed and implemented. A 3-D *P-S* physical modeling data set over a three-

dimensional physical model are collected. The physical modeling data are used to test 3-D converted-wave algorithms. Two 3-D converted-wave processing flows are developed and evaluated, based on the physical model data.

It is expected that the work will provide some practical and fast algorithms to converted-wave processing and gain some insight into the 3-D converted-wave processing. It is proposed that 3-D converted-wave prestack migration and migration velocity analysis can simplify converted-wave processing, and obtain a more interpretable convert-wave image.

1.3 Data sets used in this thesis

Synthetic and physical model *P*-*S* data sets, and Lousana 3C-2D field data set discussed below are used to test the processing algorithms and evaluate 3C-3D processing flows.

1.3.1 Synthetic data set

The synthetic data used in Chapter 2 and Chapter 3 to test the fast 3-D depth-variant CCP bining and prestack migration and migration velocity analysis were generated using zero-phase wavelet having a frequency spectrum of 10/15-40/50 Hz. This bandwidth is close to that recorded on typical field data. More details are discussed in Chapter 2.

1.3.2 3C-3D physical model data set

The 3-D prestack time migration and migration velocity analysis, and the 3-D converted-wave processing flows were developed and tested on a physical model data set created at the University of Calgary. This data set is further described in Chapter 4.

1.3.3 Lousana 3C-2D field data set

This field data set was used to test the prestack time migration algorithm. It was discussed in greater detail by Miller et al. (1993 and 1994).

1.4 Hardware and software used

The synthetic data were generated using the ray tracing software package of Sierra Geophysics, Inc., and the physical model data were acquired by the Elastic Wave Physical Modeling System in the Department of Geology and Geophysics at The University of Calgary. Most basic processing of the data used in this thesis was performed using the Inverse Theory and Application (ITA) and Advance Geophysical Corporation's ProMax 3-D processing packages, running on a Sun Microsystems Inc. workstation. Some special processing algorithms are from the CREWES Project's software. All text processing was done with Microsoft Word and Expressionist using Apple computers.

Chapter 2 - Fast 3-D *P-S* depth-variant CCP binning

2.1 Introduction

Stacking techniques for common reflection point data are commonly used in reflection seismology to attenuate multiples and random noise and to estimate the subsurface velocity distribution. The application of this technique to converted-waves is not as simple as for conventional *P-P* or *S-S* wave reflections, which have symmetrical ray paths. Even for simple, horizontally layered media, ray paths of *P-S* waves are asymmetric, as shown in Figure 2-1. Multiple coverage is not achieved by a common midpoint (CMP) gather, but requires use of the true wave conversion point, yielding a common conversion point (CCP) gather (Tessmer and Behle, 1988).

For a single, horizontal, homogeneous layer (Fig. 2-1), if the source-receiver offset is small relative to the depth of the conversion point, a first-order approximation for horizontal distance, *Xp*, of the conversion point from the source point is given by

$$X_p = \frac{2h}{1+V_s/V_p}, \qquad (2\text{-}1)$$

where V_p and V_S are the *P*-wave and *S*-wave velocities respectively (Slotboom and Lawton, 1989; Tessmer and Behle, 1988; etc.). Binning based on equation (2-1) is called asymptotic CCP binning. This is a considerable improvement over CMP binning, and is computationally faster than depth-variant binning (Schafer, 1992).

In order to improve the accuracy of CCP binning, it is necessary to account for the depth-variance of the conversion point trajectory. Tessmer and Behle (1988) have shown that the horizontal distance (*D*) of the conversion point from the source-receiver midpoint satisfies (Fig. 2-2) a fourth-degree polynomial equation

$$D^4+\left(Z_c^2-2h^2\right)D^2-2hkZ_c^2D+h^2\left(h^2+Z_c^2\right)=0\ , \qquad (2\text{-}2)$$

where Z_c is the layer thickness, *2h* is the source-receiver offset (Fig. 2-2), and $k=(1+V_s/V_p)/(1-V_s/V_p)$. A unique solution of *D*, which is real and satisfies the relation

$D \le h$, can be obtained explicitly.

From equation (2-2), it is clear that *D* (Fig. 2-2) is the function of offset *X*, depth *Z* and velocity ratio γ ($\gamma = V_p/V_s$). The solution for *D* is inconsistent and is computationally inefficient in conventional depth-variant CCP binning algorithm. Instead of using equation (2-2) to calculate *D* at every sample for each input trace, Zhong et al. (1994) proposed a so-called one step CCP stacking technique. They claim that the technique enables the accomplishment of reflection point migration, non-hyperbolic moveout and CCP stacking in one step. However it is still only another approach to depth-variant CCP stacking. They pre-calculate the *D* values for the given offset bins, and all of the time samples at the given velocity (*P-P* waves and *P-S* waves) control points and store them in an interpolation table. In the implementation of CCP stacking, for a given input trace, the *D* value for each time sample is obtained by looking up the interpolation table. In some situations, this algorithm can speed the depth-variant CCP stacking processing, but in 3-D processing, if the number of velocity control points, the number of offset bins and the number of samples are large, the algorithm needs very large computer memory and the 3-D interpolation is very slow. The interpolation table can be reduced by increasing the offset bin spacing, but this is at the expense of CCP stacking accuracy.

Lane and Lawton (1993) developed a 3-D asymptotic CCP algorithm. For both 2-D and 3-D converted-wave CCP binning methods, although asymptotic CCP binning is simple and fast, it is only a first-order approximation of the true conversion point. Conventional binning parameters for asymptotic CCP binning lead to periodicities in both offset and fold (Eaton et al., 1990). Furthermore, when the source line interval is an integer multiple of the group interval multiplied by the average V_P/V_S ratio, empty bins occur. Although the choice of an optimum bin size can solve this problem, these bins are always larger than conventional bins with a size of half the group interval (Lawton, 1993). Tessmer and Behle's (1988) depth-variant CCP binning method is accurate for a simple horizontally layered medium. However, because the expression for *D* (Fig. 2-2) is complicated and *D* must be calculated for each binned time sample, the method is very time-consuming.

In order to speed the algorithm while not losing the accuracy of the depth-variant CCP binning, a fast 3-D converted-wave depth-variant common conversion point (CCP) binning method was developed. In this chapter, the principle and implementation of this algorithm in a constant velocity medium are explained. The algorithm is then modified for a depth-variant velocity model. Finally the algorithm is implemented and applied to a 3-D

P-S synthetic data set.

2.2 Fast 3-D depth-variant CCP binning

Figure 2-3 is a schematic diagram showing how the new 3-D depth-variant common conversion point (CCP) binning method is designed, where Φ is the source-receiver azimuth, and ACCP is the position of asymptotic CCP location on the surface. In this diagram (Fig. 2-3), it is assumed that the data have been sorted into asymptotic common conversion points using equation (2-1), as discussed by Lane and Lawton (1993), and NMO corrections have already been applied to the data using the time-shifted hyperbolic equation given by Slotboom and Lawton (1989)

$$t = \frac{t_0}{2} + \sqrt{\frac{t_0^2}{4} + \frac{(2h)^2}{2V^2}}\ , \tag{2-3}$$

where t is the *P-S* travel time, t_0 is the zero-offset *P-S* travel time, $2h$ is the offset and V is the *P-S* stacking velocity.

For a single, horizontal, homogeneous layer, as shown in Figure 2-2, according to Snell's law, the following relationship exists:

$$\gamma^2\left(\frac{Z_c^2}{X_c^2}+1\right) = \frac{Z_c^2}{(2h\text{-}X_c)^2}+1, \tag{2-4}$$

where Z_c is the depth of the conversion point, X_c is the horizontal distance between the conversion and source points, $2h$ is the source-receiver offset, and γ is the ratio of *P*-wave to *S*-wave velocity (V_P/V_S). If Z_c is known, then by rationalizing equation (2-4), equation (2-2) can be obtained (Tessmer and Behle, 1988). However, if X_c is assumed, then the corresponding depth, Z_c, of the conversion point can be expressed as

$$Z_c = X_c(2h\text{-}X_c)\sqrt{\frac{1\text{-}\gamma^2}{\gamma^2(2h\text{-}X_c)^2\text{-}X_c^2}}\,. \tag{2-5}$$

For a constant velocity model, the corresponding *P-S* travel time t_c and zero-offset *P-S* travel time t_{0c} are given by

$$t_c = \frac{\sqrt{X_c^2+Z_c^2}}{V_p} + \frac{\sqrt{(2h\text{-}X_c)^2+Z_c^2}}{V_s}, \tag{2-6a}$$

$$t_{0c} = \frac{Z_c}{V_p} + \frac{Z_c}{V_s}. \qquad \text{(2-6b)}$$

The algorithm has three steps: first, finding the horizontal distance X_c from the conversion point to the source point; then calculating the corresponding depth Z_c; finally, mapping the samples to their new bins. Figure 2-4a and Figure 2-4b illustrate this procedure, showing a plan view, and a cross section from source to receiver, respectively.

Figure 2-4 shows that the true conversion point is always located horizontally between the asymptotic conversion point and the receiver. The shallower the conversion point, the further the true conversion point is from the asymptotic conversion point. For each trace in a given coordinate system, the source and receiver positions are known. Once the 3-D binning grid is chosen, all of the centers of the bin positions are fixed in this coordinate system. Given these parameters, the intersections of the source-receiver line and the bin boundaries can be determined. In CCP binning or stacking, only the bin number of the sample is needed. It is not necessary to know the exact surface location of a sample. By this consideration, only intersections which lie between the asymptotic conversion point (ACCP) and the receiver need be considered. For example, in Figure 2-4a, once the two intersections between the source-receiver line and the boundary of bin 2 have been found, the corresponding distances X_{c1} and X_{c2} can be calculated. Substituting the horizontal distance X_c, offset $2h$ and velocity ratio γ into equation (2-5), the corresponding depths Z_{c5} and Z_{c4} for X_{c1} and X_{c2} can be derived respectively, as shown in Figure 2-4b. Zero-offset two-way travel times t_{05} and t_{04}, corresponding to depths Z_{c5} and Z_{c4}, are calculated using equation (2-6b). Finally, the samples between time interval t_{05} and t_{04} are relocated to their new bin number, bin 2. For the example shown in Figures 2-4a and 2-4b, the equations (2-5) and (2-6b) are solved only five times for this trace.

Based on the above discussion, compared with the conventional depth-variant CCP binning, the new depth-variant CCP binning method has the following advantages. The derivation is very straightforward and the calculations of depth Z_c from X_c are simpler than that of X_c from Z_c, so the algorithm is much faster. Samples are mapped to their new CCP binning locations block-by-block, instead of sample-by-sample, so it is a very rapid way to implement the 3-D depth-variant CCP binning method.

2.3 Modification for depth-variant velocities

The above procedure can be generalized to include the more realistic case of a layered earth where the *P*-wave and *S*-wave velocities vary with depth. To simplify the discussion while retaining the general application of the conclusions, it is assumed that, although the *P*-wave and *S*-wave velocities are depth-variable, their ratio γ ($\gamma = V_p/V_s$) is constant or varying only slowly with depth. This is a good approximation for real data at common depths of interest. In equation (2-5), for a given offset and horizontal distance from the conversion point to the source, only the velocity ratio γ affects the depth Z_c of the conversion point. This means that, for a given depth, velocity ratio and offset, the conversion points maintain horizontal position regardless of *P*- and *S*-wave velocity changes. If the velocity ratio γ changes slowly with depth, then the average velocity ratio $\overline{\gamma}$ from the surface to a certain depth can be used in equation (2-5). However, in the conversion from the depth Z_c to its corresponding zero-offset two-way travel time, equations (2-6) are no longer suitable.

To convert from Z_c to its corresponding zero-offset two-way travel time, the *P*-wave root mean square (RMS) velocity (V_p^{RMS}) and converted-wave (*P*-*S*) velocity, denoted as V_{ps}^{RMS}, are assumed to be available from a velocity analysis of *P*-wave and *P*-*S* data. The *P*-*S* RMS velocity is approximately the *P*-*S* stacking velocity used in the *P*-*S* NMO correction, as given by equation (2-3).

Based on the above assumptions and definitions, the *P*-wave interval velocity (V_p) and *P*-*S* interval velocity (V_{ps}) for each time sample can be calculated by the following equation given by Tessmer and Behle (1988):

$$V_{ps(i+1)}^2 = \frac{\left(V_{ps(i+1)}^{RMS}\right)^2 t_{0(i+1)} - \left(V_{ps(i)}^{RMS}\right)^2 t_{0(i)}}{t_{0(i+1)} - t_{0(i)}}, \qquad (2\text{-}7)$$

as shown in Figure 2-5, where the subscripts *i* and (*i+1*) refer to the *i* and (*i+1*) samples respectively. Then the corresponding depths, D_p and D_{ps}, for every time sample of *P*-*P* and *P*-*S* data can be derived using the following equations:

$$D_{i+1} = D_i + \Delta t \cdot V_{i+1} \qquad i = 1 \text{ to NS} \qquad (2\text{-}8)$$
$$\textit{with } D_0 = 0,$$

where Δt is the sample rate, *i* is the time sample number, NS is the total number of

samples, V_{i+1} is the interval V_p or V_{ps} at time sample *i+1*, D_{i+1} and D_i are D_p or D_{ps} at the time samples *i+1* and *i* respectively. These D_p or D_{ps} values for the velocity control points are computed and stored in a table for later use. For the *P-P* and *P-S* data, the corresponding depths (D_p and D_{ps}) for the same time sample are different. In order to calculate the interval velocity ratio γ, the *P*-wave and *S*-wave velocities at the same depth are needed. By linear interpolation, the *P*-wave interval velocity at each reference depth (D_{ps}) can be obtained. Because the interest is in *P-S* data processing, the reference depth is chosen to be that corresponding to each time sample of the *P-S* data.

Now that the *P*-wave interval velocity and *P-S* interval velocity at the depth corresponding to each time sample of the *P-S* data have been obtained, the next step is to calculate the *S*-wave interval velocity. Again according to Tessmer & Behle (1988), the relationship between the interval *P-S* velocity and *P*-wave and *S*-wave velocities can be approximated as

$$V_{ps(i)}^2 = V_{p(i)} V_{s(i)} \,. \tag{2-9}$$

With this derived *S*-wave interval velocity, velocity ratio γ for each depth, corresponding to each time sample of *P-S* data, can be derived simply by

$$\gamma_{(i)} = \frac{V_{p(i)}}{V_{s(i)}}. \tag{2-10}$$

Then the average velocity ratio $\overline{\gamma}$ can be derived as following:

$$\bar{\gamma}_{(i)} = \frac{1}{i} \sum_{j=1}^{i} \gamma_{(j)}. \tag{2-11}$$

In equation (2-4) or equation (2-5), in order to calculate the depth Z_c for a given offset (*2h*) and horizontal distance from the conversion point to the source point (X_c), the average velocity ratio ($\overline{\gamma}$) from the surface to this depth must be known, if γ changes with depth. This gives rise to the question of how the $\overline{\gamma}$ can be obtained without already knowing Z_c. To deal with this problem, the following approximation technique is used. As shown in Figure (2-4b) and discussed above, before the calculation of Z_{c4}, the depth Z_{c5} has already been calculated. The average velocity ratio $\overline{\gamma}$ at depth Z_{c5} is used in equation (2-5) to calculate the depth $Z_{c4}^{'}$, which is the first-order approximation for the true depth Z_{c4}. Given the calculated depth $Z_{c4}^{'}$, an updated average velocity ratio $\overline{\gamma}$ at $Z_{c4}^{'}$ can be calculated. Substituting this new average velocity ratio $\overline{\gamma}$ into equation (2-5), the second-

order approximation for the true Z_{c4} can be obtained. Generally, as indicated in the assumptions, the average velocity ratio ($\overline{\gamma}$) changes very slowly with depth, so the second-order approximation can match the true depth Z_{c4} well.

The conversion of depth Z_c into its corresponding zero-offset two-way travel time is very simple. As mentioned early, for each time sample of *P*-*S* data, the depth D_{ps} is already calculated and saved in a table. By looking in this table, the zero-offset two-way travel time t_0, corresponding the calculated depth, Z_c , can be found.

2.4 Application of this new algorithm to synthetic data

This algorithm was first applied to a converted-wave synthetic data set generated by ray tracing using Sierra software.

2.4.1 Model description

As shown in Figure 2-6, the 3-D numerical model consists of four flat layers with a pyramid sitting on the top of the base layer. The cross-sections of the model in north-south and east-west directions, which are across the peak of the pyramid, are shown in Figures 2-7a and 2-7b respectively. In these two figures, the interfaces of the pyramid in north-south direction, which is defined as receiver-line or in-line direction, are symmetrical and their dip angles are 30 degrees, whereas that in east-west direction, which is defined as shot-line or cross-line direction, are asymmetrical and with dip angles of 10 and 20 degrees. The depths, *P*-wave and *S*-wave velocities of the different layers are also shown on these figures. The summit height of the pyramid is 300 m and its peak is 100 m below the second layer. The motivation to generate this kind of model was to (1) simulate a depth-variant *P*-*P* and *P*-*S* velocity model, as well as a depth variant velocity ratio; (2) to compare the images of dipping reflectors using different CCP stacking or binning algorithms; (3) to demonstrate converted-wave prestack migration and migration velocity analysis, which are discussed later in chapter 3.

2.4.2 Geometry design and data generation

The plan view of the survey is shown in Figure 2-8. There are 5 shot lines recorded with line spacing of 300 m, 25 shots per shot line and shot spacing of 100 m. For each shot, data were generated along 11 receiver lines with a spacing of 100 m, 61 receiver stations per receiver line and a receiver spacing of 50 m. The sample rate is 2 ms

and the record length is 1.5 s. In the design of the survey, the receiver line is chosen to be in north-east direction, because (1) the dip angles of the dipping reflectors of the pyramid is greater than in the other direction; (2) the bin spacing in receiver-line is smaller; (3) by doing this, spatial aliasing caused by the data can be effectively prevented. The center of the survey is exactly at the surface location of the peak of the pyramid. Here, in-line refers to receiver-line direction and cross-line refers to shot-line direction.

A 3-D *P*-*S* data set was created over the model using the geometry described above. Figure 2-9 is an example shot gather from the synthetic data. Here, only every second trace is plotted. From this shot gather, it is seen that there are three major events corresponding the three flat reflectors. For all of these events, as expected, there is no *P*-*S* energy at zero offset because no *P*-wave is converted, and it increases with the increasing offset (or the incident angle). After a certain offset, it becomes smaller when the offset increases further until reaching the critical angle, at which the *P*-*S* energy is again zero. After the critical angle, the amplitude becomes strong and the phase is reversed. The reflections from the dipping reflectors can also be seen very clearly, but it is not clear if these events are pre-critical or post-critical.

2.4.3 Comparison between asymptotic and depth-variant CCP binning

The synthetic data set was first processed by asymptotic CCP stacking. The example stacked section in the in-line direction is shown in Figure 2-10. This section is exactly at the same position as the cross section in Figure 2-7a. The velocity ratio for asymptotic CCP stacking is 2.0. As anticipated, every fourth trace is empty, because the conventional in-line bin spacing of 25 m was chosen and the source interval is an even integer multiple of the group interval multiplied by the average V_P/V_S ratio. Also, the reflections for the dipping reflectors are poorly imaged, because of the effect of dip-moveout and inaccuracy of CCP stacking.

The data are also processed using the new depth-variant CCP binning technique developed in this chapter. The example stacked section, which is at the same position as in Figure 2-10, is shown in Figure 2-11. The comparison between Figure 2-10 and the Figure 2-11 shows that the empty bins no longer exist, and more importantly, the image of the dipping reflector is improved greatly. However, careful examination of the shallowest event in Figure 2-11 shows that some traces still have zero amplitudes. This is because of the lack of near offset traces and NMO stretch mute at these CCP bins.

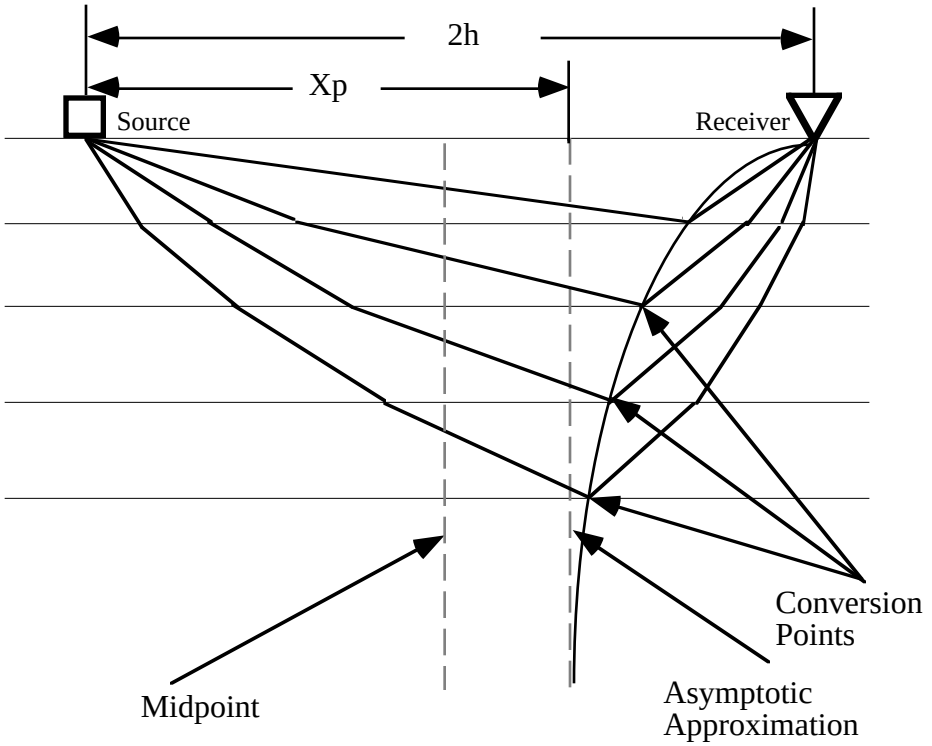

FIG. 2-1. Schematic diagram for 2-D common conversion point (CCP) binning.

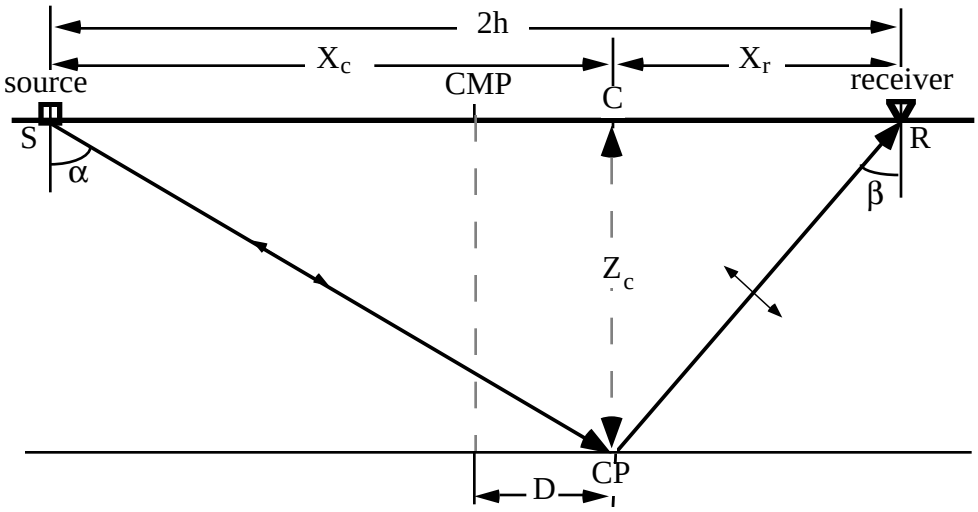

FIG. 2-2. The raypath of a converted-wave (*P*-*S*).

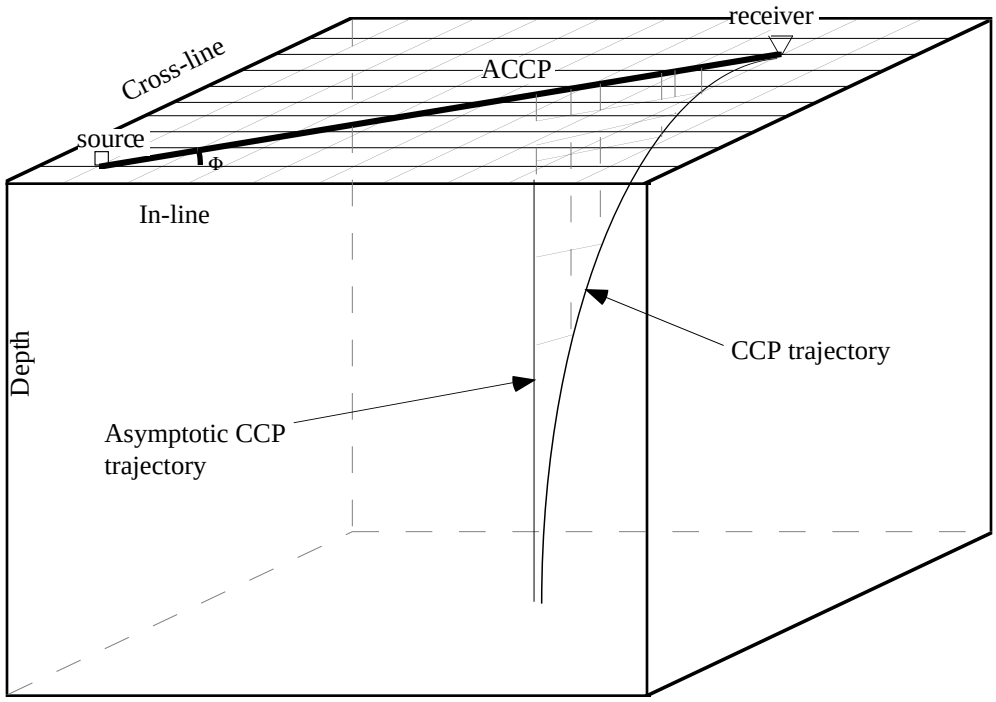

FIG. 2-3. Schematic diagram for 3-D depth-variant common conversion point (CCP) binning.

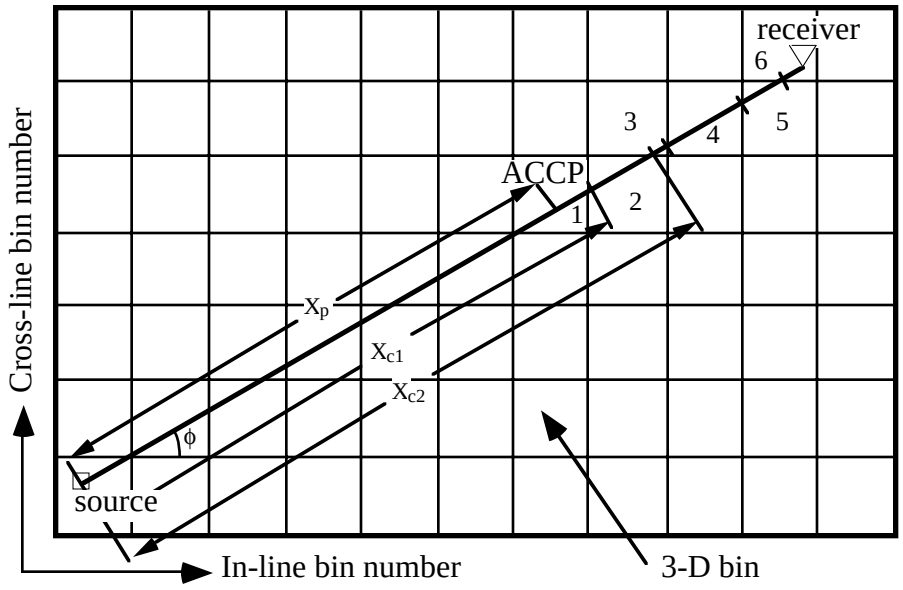

FIG. 2-4a. Plan view of 3-D depth-variant CCP binning scheme.

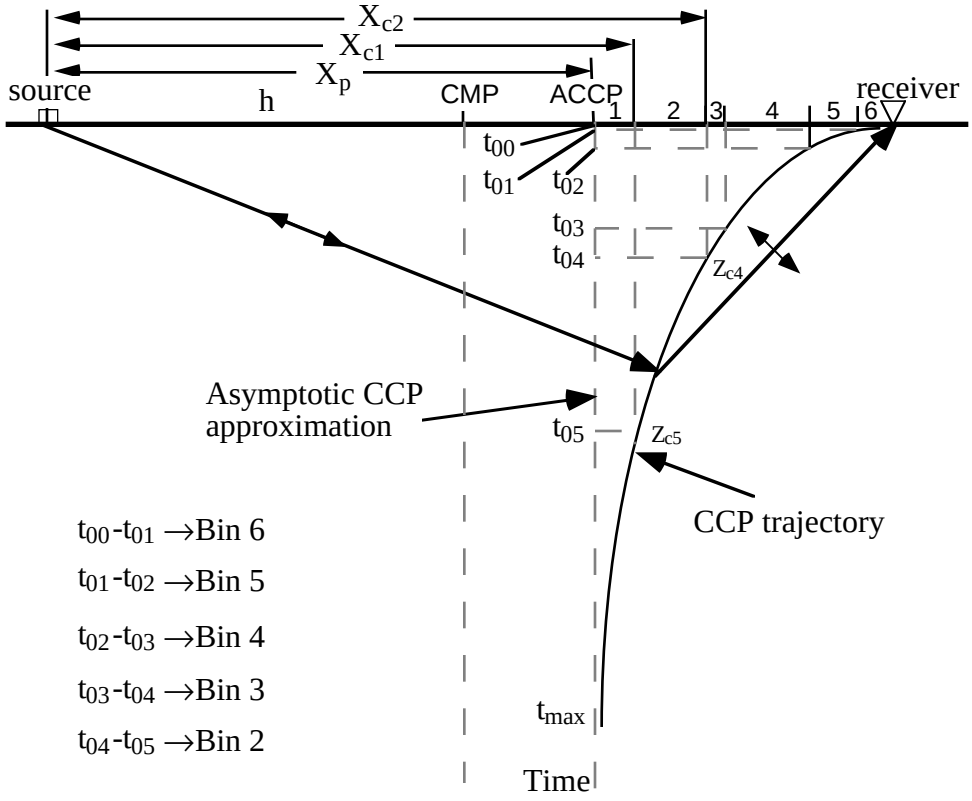

FIG. 2-4b. Cross-section in source-receiver azimuth direction showing how to implement 3-D depth-variant CCP binning method.

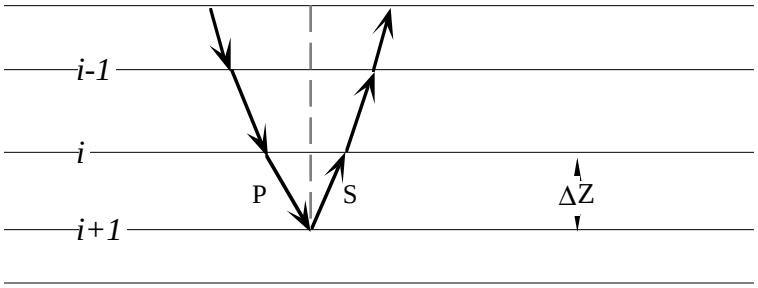

FIG. 2-5. The diagram showing the relationship of *P*-*S* velocity and *P*- and *S*-wave interval velocities.

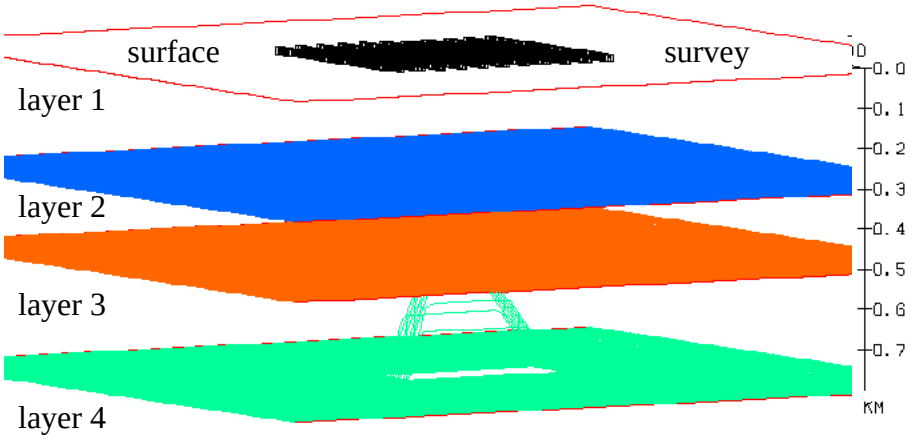

FIG. 2-6. The 3-D plan view of the four layer model showing the layers, the pyramid and the survey. The center of the survey is at the surface location of the peak of the pyramid.

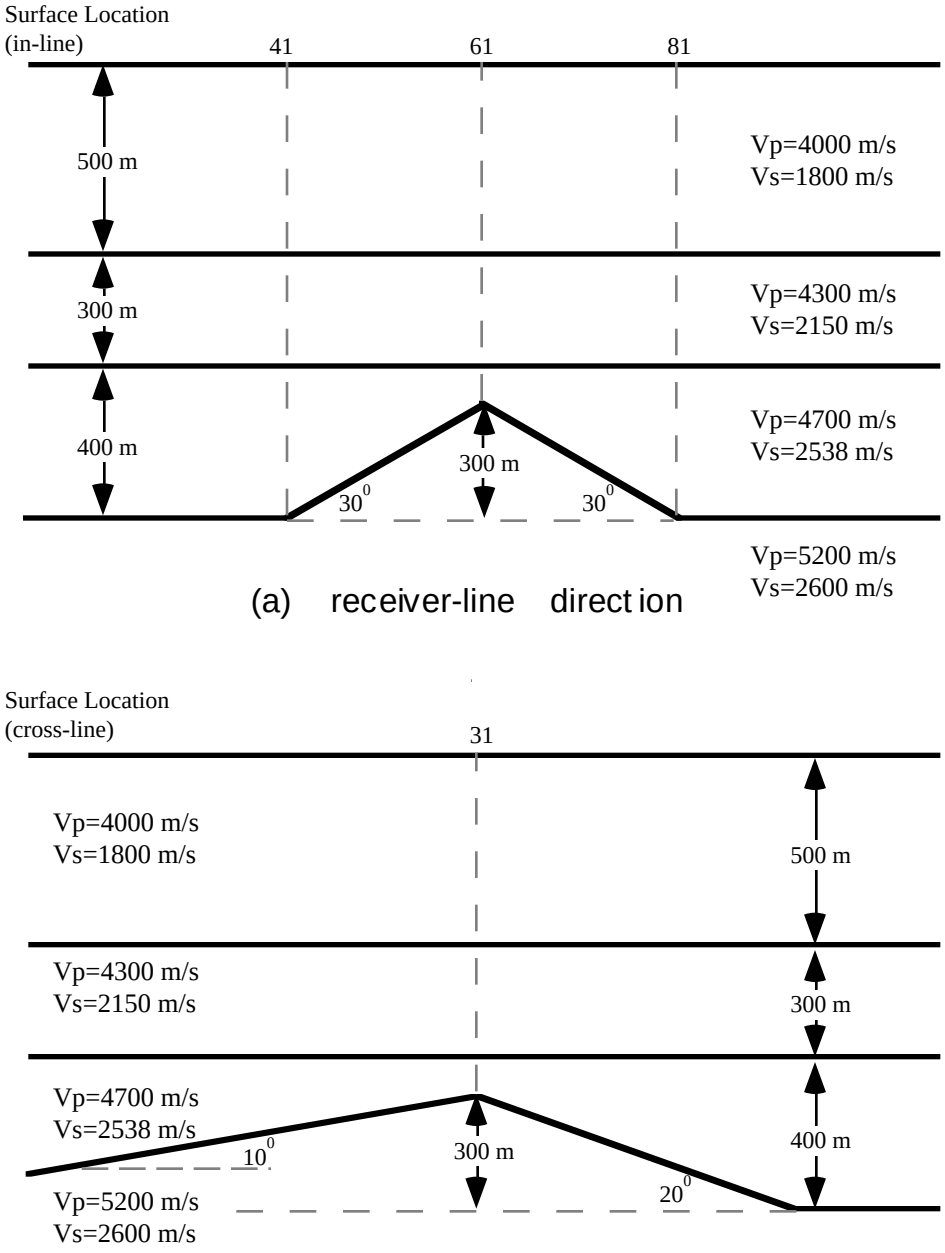

FIG. 2-7. Cross-sections of the 4-layer model. (a). the cross-section is in receiver-line direction(north-south, in-line direction) and across the center of the survey. The in-line bin interval is 25 m, and the dipping reflactors are symmetrical and their dipping angles are 30 degrees. (b). the cross-section is in shot-line direction (east-west, cross-line direction) and across the center of the survey. The cross-line bin interval is 50 m, and the dipping reflectors are asymmetrical and their dip angles are 10 and 20 degrees.

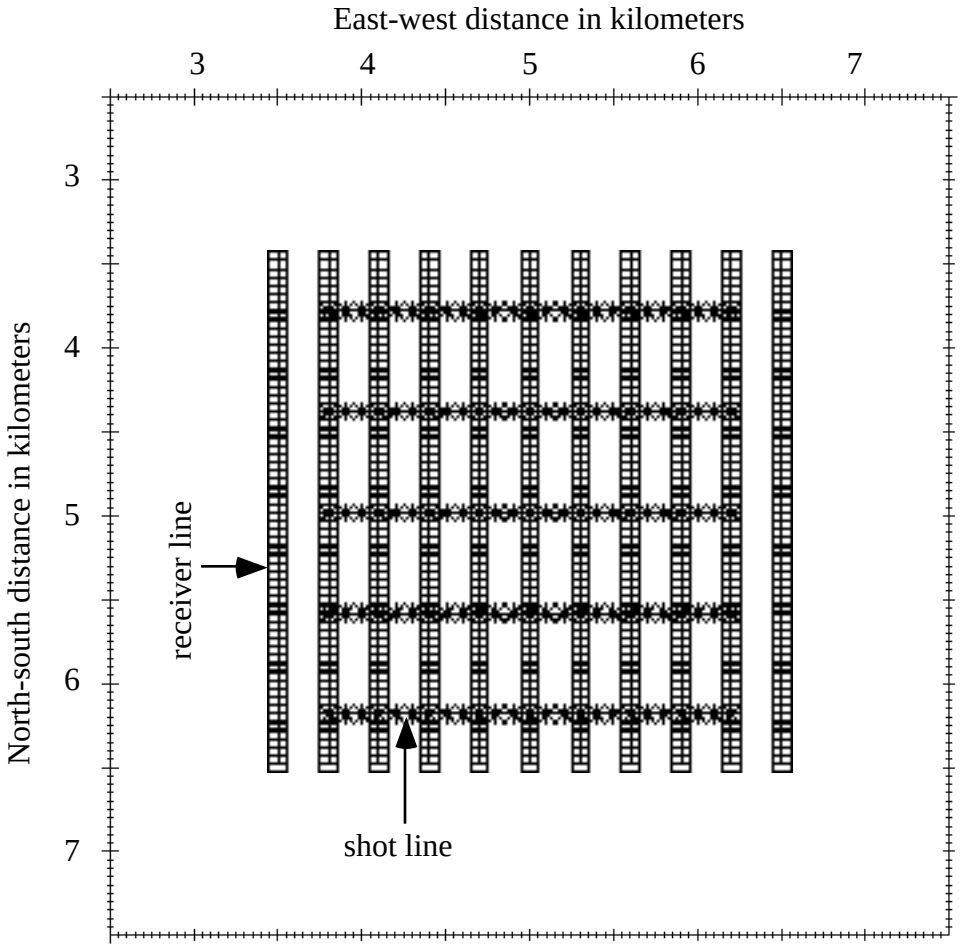

FIG. 2-8. The plan view showing the data generation geometry. The shot locations are identified by "*" and the receiver locations are by "+".

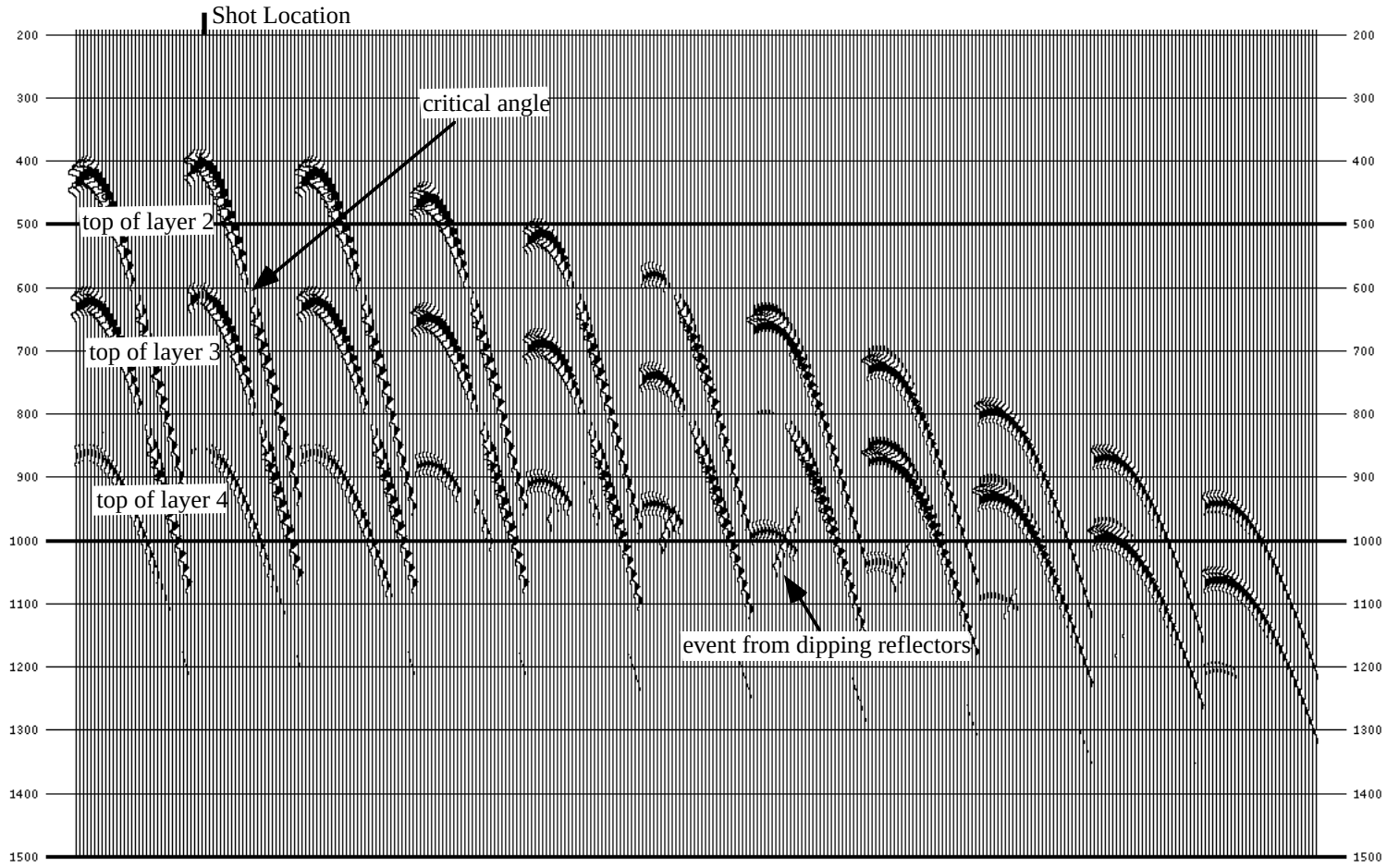

FIG. 2-9. Example of *P*-*S* shot gathers. Here only every second traces of the first shot are plotted.

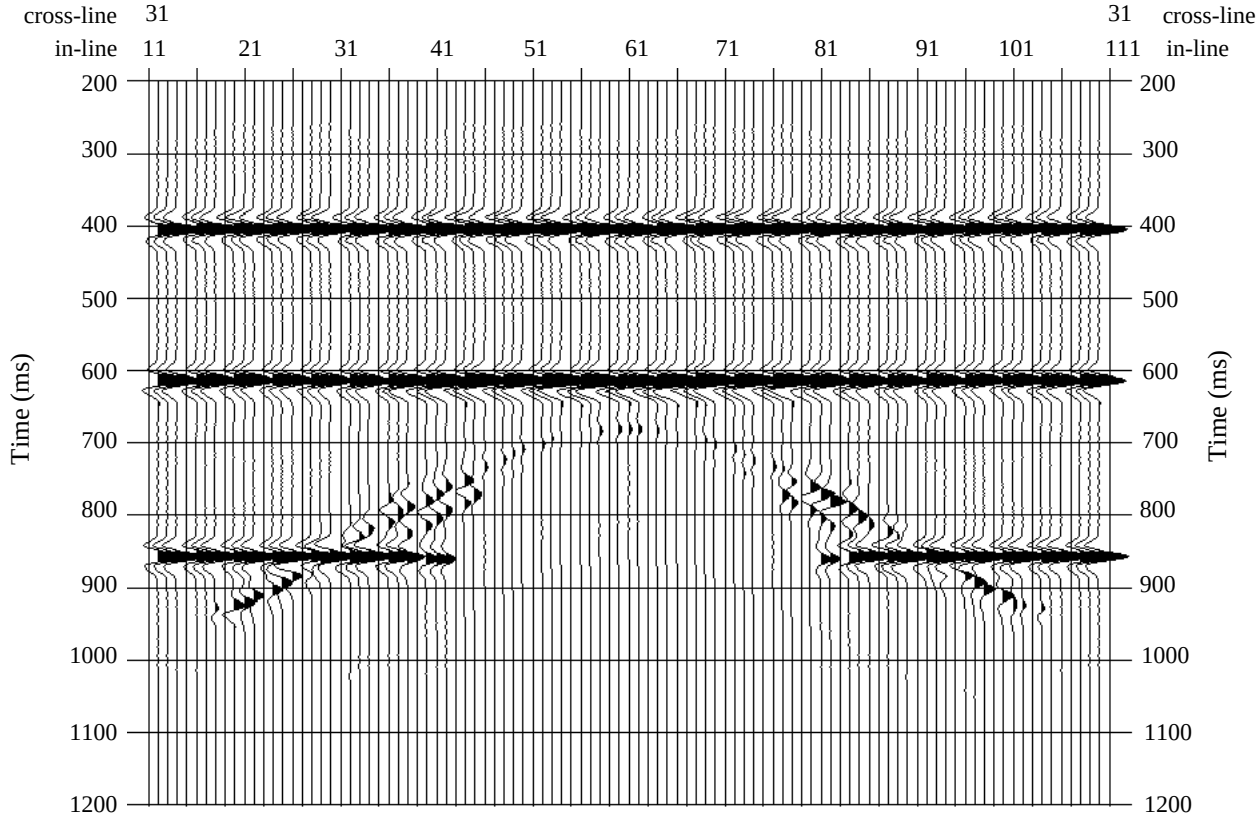

FIG. 2-10. 3-D asymptotic CCP stacked section. The cross section is at the same position and direction as the cross section in Figure 2-7(a). The velocity ratio is 2.0.

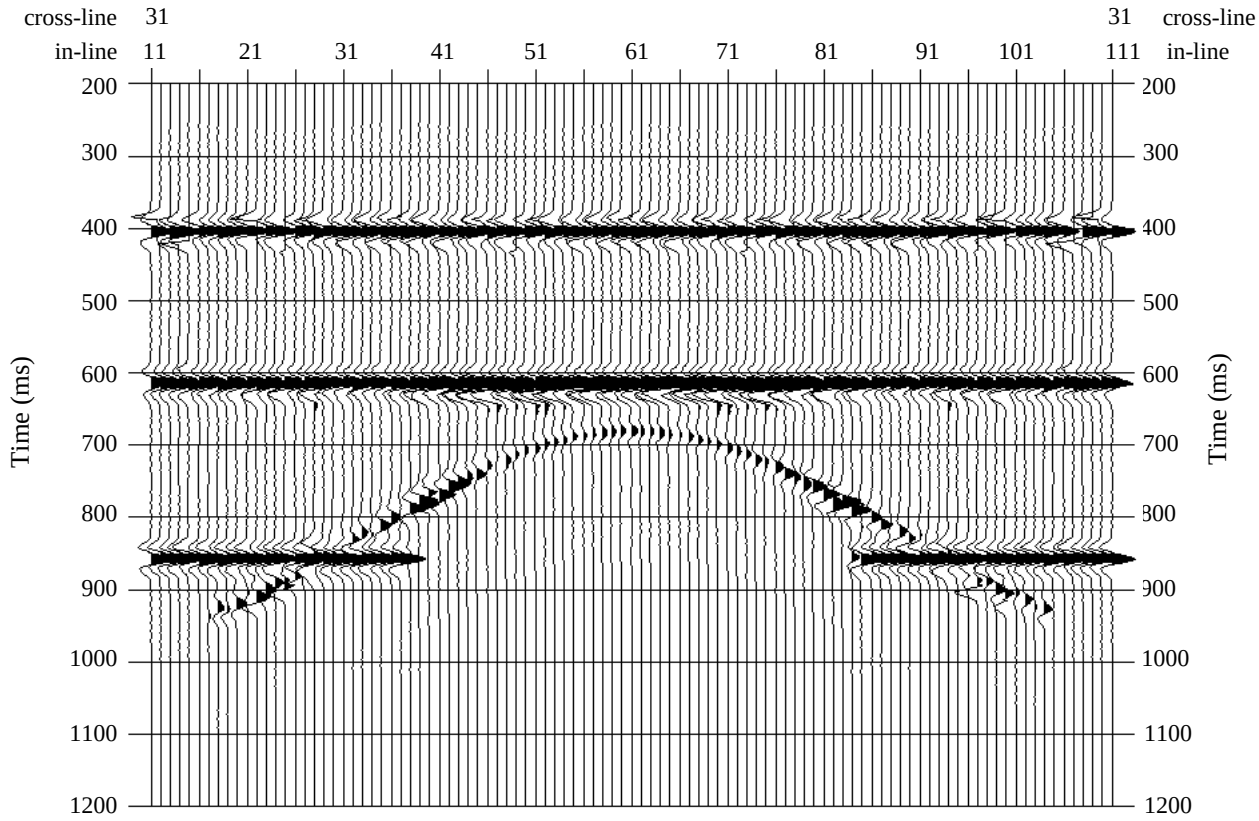

FIG. 2-11. 3-D depth-variant CCP stacked section. The cross section is at the same position and direction as the cross section in Figure 2-7(a).

Chapter 3 - Prestack time migration and migration velocity analysis

3.1 Introduction

Processes of *P-S* data may be different and more complex from corresponding *P-P* processing steps, because the *P-S* ray paths are different from those of *P-P* waves. Some special processes, such as common conversion point (CCP) binning, *P-S* NMO correction and velocity analysis, *P-S* DMO and migration, must be involved. As an alternative, one-step converted-wave prestack migration may help to simplify the processing, but in some situations it is too expensive to be practical, especially for 3C-3D data processing. In converted-wave processing, prestack migration is much more expensive than that in *P-P* wave processing, because of complexity in its kinematics. Another important factor that may discourage the use of converted-wave prestack migration is that it is very difficult to estimate the velocities in *P-S* data (Tessmer and Behle, 1988; Harrison, 1992). Prestack migration by equivalent offsets and common conversion scatter point (CCSP) gathers may assist more straight forward processing of *P-S* data (Bancroft and Wang, 1994).

Migration is a process that attempts to reconstruct an image of the original reflecting structure from energy recorded on input seismic traces. Prestack migration is a direct process that moves each sample to all the possible reflection positions, and invokes the principles of constructive and destructive interference to recreate the actual image. An alternate description of the migration process starts by selecting an output migrated sample. All input traces are searched to find energy that contributes to the output sample. This second description is the basis of Kirchhoff migration (Bancroft et al., 1995) .

Prestack migration by equivalent offsets and common scatter point (CSP) gathers, which is based on the principle of prestack Kirchhoff migration, has already been applied successfully to *P-P* data (Bancroft et al., 1994). In this method, CSP gathers are created for each migrated trace by replacing the common midpoint (CMP) gathers of conventional processing. Samples for each input trace are assigned an equivalent offset for each output scatter point position, then transferred into the appropriate offset bin of the CSP gather. By

doing this, the prestack time migration is reduced to be a simple re-sort and collection of the data into CSP gathers, and the velocity analysis on these CSP gathers becomes more effective, because the CSP gather has more fold and a larger maximum offset than conventional CMP gather has. The method proved to be simpler, faster and more flexible than the conventional approach.

Prestack migration by equivalent offsets and CCSP gathers may be more attractive for converted-wave processing. After the *P*-*S* data are transformed into CCSP gathers by equivalent offsets, the asymmetry of the *P*-*S* ray paths is "removed", and some algorithms, such as conventional NMO correction and semblance velocity analysis, can be applied to the CCSP gathered *P*-*S* data, and CCP binning is not necessary. In this chapter, I first describe the principle of *P*-*S* prestack migration by equivalent offsets and CCSP gathers, and discuss the effect of the velocity uncertainty on the accuracy of the equivalent offsets. Then I explain how to perform *P*-*S* migration velocity analysis using the conventional semblance velocity analysis tools. Finally, applications to numerical modeling data and field data are discussed to demonstrate the feasibility of this method.

3.2 Prestack time migration

3.2.1 Pseudo depth for converted waves

As shown in Figure 3-1, h_s, h_r and h_e are the source, receiver and equivalent offsets from the CCSP surface location respectively. In this figure, it is shown that the co-location E for this particular R and S can be at any position on the circle with center at Common Conversion Scatter Point (CCSP) and radius h_e. If the depth of common conversion scatter point is Z_0 and the *P*-wave and *S*-wave root mean square (RMS) velocities are $V_{p\,rms}$ and $V_{s\,rms}$ respectively, then the travel times from source (S) to CCSP (T_s) and CCSP to receiver (R) (T_r) can be expressed as

$$T_s^2 = T_{s0}^2 + \frac{h_s^2}{V_{p\,rms}^2}, \tag{3-1a}$$

$$T_r^2 = T_{r0}^2 + \frac{h_r^2}{V_{s\,rms}^2}, \tag{3-1b}$$

respectively. Where T_{s0} is the zero offset one way travel time for down-going *P*-wave and T_{r0} is the zero offset one way travel time for up-going *S*-wave.

The equation (3-1) can be rewritten as following:

$$T_s^2 = \frac{\left(Z_{s0}^{'}\right)^2 + h_s^2}{V_{p\,rms}^2}, \tag{3-2a}$$

$$T_r^2 = \frac{\left(Z_{r0}^{'}\right)^2 + h_r^2}{V_{s\,rms}^2}. \tag{3-2b}$$

In the above equation, the terms $Z_{s0}^{'}$ and $Z_{r0}^{'}$ are defined as the pseudo depths for down-going *P*-wave and up-going *S*-wave respectively, i.e.

$$Z_{s0}^{'} = T_{s0} V_{p\,rms}, \tag{3-3a}$$

$$Z_{r0}^{'} = T_{r0} V_{s\,rms}. \tag{3-3b}$$

The true depth can be expressed as

$$Z_0 = T_{s0} V_{p\,ave}, \tag{3-4a}$$

$$Z_0 = T_{r0} V_{s\,ave}, \tag{3-4b}$$

where $V_{p\,ave}$ and $V_{s\,ave}$ are the *P*-wave and *S*-wave average (AVE) velocities respectively.

Substituting equation (3-4) into equation (3-3) yields the following:

$$Z_{s0}^{'} = Z_0 \frac{V_{p\,rms}}{V_{p\,ave}}, \tag{3-5a}$$

$$Z_{r0}^{'} = Z_0 \frac{V_{s\,rms}}{V_{s\,ave}}. \tag{3-5b}$$

From the above equation, the pseudo depths $Z_{s0}^{'}$ and $Z_{r0}^{'}$ are different from the true depth Z_0 except for a constant velocity model, and may be different from each other. $Z_{s0}^{'}$ and $Z_{r0}^{'}$ will be identical when the velocities V_p and V_s are constant or when the velocity ratio γ is constant. When the velocities vary with depth, the relative stability of γ will ensure similar values of V_{rms}/V_{ave} for the *P*- and *S*-wave velocities. Consequently the pseudo

depths $Z_{s0}^{'}$ and $Z_{r0}^{'}$ will be assumed close enough to be approximated by a single value $Z_0^{'}$.

3.2.2 Equivalent offset for converted waves

Because of the limitations of the RMS velocities as discussed in the above section, the *P*-wave and *S*-wave migration velocities are used in the discussion of this chapter. Here, the *P*-wave and *S*-wave migration velocities are defined as the velocities by which the best seismic image after prestack migration can be obtained. For the convenience, the pseudo depth $Z_0^{'}$ is donated as Z_0 .

The *P*-wave and *S*-wave migration velocities from source and receiver to CCSP are $V_{p\ mig}$ and $V_{s\ mig}$ respectively, then the migration velocity ratio is defined as

$$\gamma_{mig} = \frac{V_{p\ mig}}{V_{s\ mig}} \ . \tag{3-6}$$

In order to see the geometry more clearly, a cross section is shown in Figure 3-2 for the case in which the source, receiver and CCSP surface locations are on the same plane.

Following Bancroft and Wang (1994), the equivalent offset for converted-waves is computed by equating the travel time T from the source T_s and receiver T_r with the travel time T from co-located source T_{es} and receiver T_{er}, i.e.

$$T = T_s + T_r = T_{es} + T_{er} \ . \tag{3-7}$$

It can be expressed as

$$\frac{\left(Z_0^2 + h_e^2\right)^{1/2}}{V_{p\ mig}} + \frac{\left(Z_0^2 + h_e^2\right)^{1/2}}{V_{s\ mig}} = \frac{\left(Z_0^2 + h_s^2\right)^{1/2}}{V_{p\ mig}} + \frac{\left(Z_0^2 + h_r^2\right)^{1/2}}{V_{s\ mig}} \ . \tag{3-8}$$

Substituting equation (3-6) into equation (3-8) and solving for the equivalent offset h_e gives:

$$h_e = \left[\frac{1}{(1+\gamma_{mig})^2} \left(\left(Z_0^2 + h_s^2\right)^{1/2} + \gamma_{mig} \left(Z_0^2 + h_r^2\right)^{1/2} \right)^2 - Z_0^2 \right]^{1/2} \ . \tag{3-9}$$

When finding the value of h_e for a given input trace, the values of h_s and h_r are known, γ_{mig} is initially assumed to be 2.0 (until a more referred value is obtained) and

$V_{p\,mig}$ is obtained from conventional *P-P* processing. The value of Z_0 is estimated by splitting equation (3-8) into two equations, i.e.

$$T = \frac{\left(Z_0^2 + h_e^2\right)^{1/2}}{V_{p\,mig}} + \frac{\left(Z_0^2 + h_e^2\right)^{1/2}}{V_{s\,mig}}, \tag{3-10a}$$

$$T = \frac{\left(Z_0^2 + h_s^2\right)^{1/2}}{V_{p\ mig}} + \frac{\left(Z_0^2 + h_r^2\right)^{1/2}}{V_{s\ mig}}, \tag{3-10b}$$

which give:

$$Z_0^2 = \frac{C_2^2 - 2C_1 \pm C_2\left(C_2^2 + 4h_s^2 - 4C_1\right)^{1/2}}{2}, \tag{3-11a}$$

where C_1 and C_2 are coefficients given by:

$$C_1 = \frac{T^2 V_{p\ mig}^2 + h_s^2 - \gamma_{mig}^2 h_r^2}{1 - \gamma_{mig}^2}, \tag{3-11b}$$

$$C_2 = \frac{2TV_{p\ mig}}{1 - \gamma_{mig}^2}. \tag{3-11c}$$

By ensuring the value of Z_0^2 is real and positive, a unique solution of Z_0^2 in equation (3-11a) can be obtained. Substituting equation (3-11a) into equation (3-10a), and solving for h_e gives:

$$h_e = \left[\frac{T^2 V_{p\ mig}^2}{(1+\gamma_{mig})^2} - Z_0^2\right]^{1/2}. \tag{3-11d}$$

Equations (3-11) are used to calculate equivalent offsets.

3.2.3 The effect of velocity error on the accuracy of equivalent offset

In equations (3-11), it is shown that the equivalent offset h_e is the function of two-way travel time T, so it is depth-variant; the expression of h_e is also velocity-dependent. Hence, it is necessary to know what is the effect of the velocity error on the accuracy of equivalent offset h_e.

Shown in Figure 3-3b are the h_e curves at different CCSP surface locations, calculated using the equations (3-11). Figure 3-3a shows the geometry of the source,

receiver and CCSP surface positions in the source-receiver direction. In each curve, the start time is given by:

$$T_{start} = \frac{h_s}{V_{p\ mig}} + \frac{h_r}{V_{s\ mig}} = \frac{h_s}{V_{p\ mig}} + \frac{\gamma_{mig} h_r}{V_{p\ mig}} = \frac{1}{V_{p\ mig}} (h_s + \gamma_{mig} h_r). \tag{3-12}$$

Where $V_{p\ mig}$ and $V_{s\ mig}$ are the *P*-wave and *S*-wave migration velocities near the surface. In Figure 3-3b, it is seen that when the CCSP surface position (CCSP:0) is exactly at the midpoint between the source and receiver, h_e is time- and velocity-independent and equal to the source to receiver offset. As the CCSP surface position (CCSP:-1000 or CCSP:1000) moves away from the source-receiver midpoint, the variation of h_e with time or depth becomes greater. When the CCSP surface position (CCSP:-2000 or CCSP:2000) is close to the source or receiver position, the fastest variation of h_e with time occurs. With the CCSP location (CCSP:-3000, CCSP:3000, CCSP:-4000 or CCSP:4000) further away from the midpoint, the change becomes less rapid again. As expected, the h_e curves are not symmetric along the midpoint because the asymmetry of the *P*-*S* ray paths. In this example, the source-receiver offset is quite large (4000 m), so the depth-dependent property of h_e is significant. Generally, for a conventional migration aperture, h_e does not change very rapidly with time, as shown in Figure 3-3b, when the CCSP is located between 1000 m and -1000 m. Figure 3-4 shows how the velocity error affects the equivalent offset h_e. Beside each curve is the relative velocity error. From this figure, it is seen that the velocity error indeed has some effect on h_e, especially at early times, but with increasing time, this effect becomes negligible. If the target depth is not shallow, this equivalent offset error should be within half of the offset bin increment for a reasonable velocity error to be obtained.

3.2.4 Practical computation of CCSP gathering

The calculation of h_e based on equations (3-11) is not practical because the samples are moved to their equivalent offset bins by a sample-by-sample process, hence it is time consuming. In practice, the equivalent offsets are quantized into equivalent offset bins, as shown in Figure 3-5. A number of samples may have offsets that fall in the same offset bin. An improved procedure starts by computing the first offset with equations (3-11), then computing the time T_n when the later samples will be located in the next offset bin.

For a given h_{en}, $V_{p\ mig}$, γ_{mig}, h_s and h_r, solving for Z_{0n}^2 from equation (3-8) gives

$$Z_{0n}^2 = \frac{h_s^2 h_r^2 - b_n^2}{2b_n - h_s^2 - h_r^2}, \tag{3-13a}$$

where b_n is an intermediate value, i. e.

$$b_n = \frac{(1+\gamma_{mig})^2 h_{en}^2 - h_s^2 - \gamma_{mig} h_r^2}{2\gamma_{mig}}. \tag{3-13b}$$

Substituting Z_{0n}^2 into equation (3-10b) gives

$$T_n = \frac{\left(Z_{0n}^2 + h_s^2\right)^{1/2} + \gamma_{mig}\left(Z_{0n}^2 + h_r^2\right)^{1/2}}{V_{p\,mig}}. \tag{3-13c}$$

Instead of using equations (3-11), equations (3-13) are used to move sample blocks to appropriate offset bins.

3.3 Migration velocity analysis

Velocity analysis by conventional method for *P*-*S* waves is more complicated than that for *P*-*P* waves, because its normal moveout (NMO) is not hyperbolic. A time-shifted hyperbolic NMO equation (Slotboom and Lawton, 1989; Slotboom et al., 1990) is needed to implement *P*-*S* NMO correction and *P*-*S* velocity analysis, but the time-shifted hyperbolic NMO equation is only a second-order approximation. Assuming that the *P*-*S* root mean square (RMS) velocities are obtained from *P*-*S* velocity analysis, it is still difficult to derive accurately the *S*-wave RMS and/or interval velocities (Tessmer and Behle, 1988).

By rewriting the equation (3-11d), it was found that in CCSP gathers, the relationship between the *P*-*S* wave two-way travel time and equivalent offset is exactly hyperbolic. This encouraging property motivated the further study of converted-wave migration velocity analysis.

In this section, a new *P*-*S* prestack migration velocity analysis approach is proposed. At first, the relationship of migration velocity with RMS and average velocities is discussed to gain some basic knowledge about the possible value for migration velocity. Secondly, the principle of converted-wave migration velocity analysis is presented.

Finally, the practical velocity analysis procedure is tested and the convergence of velocity analysis result is studied.

3.3.1 Principle of migration velocity analysis

Equation (3-10a) can be written in another form, i. e.

$$T = \frac{\left(Z_0^2+h_e^2\right)^{1/2}}{V_{p\ mig}} + \frac{\left(Z_0^2+h_e^2\right)^{1/2}}{V_{s\ mig}}$$
$$= \left(\frac{(1+\gamma_{rms})^2 Z_0^2}{V_{p\ mig}^2} + \frac{(1+\gamma_{mig})^2 h_e^2}{V_{p\ mig}^2}\right)^{1/2} .$$

The above equation can be expressed as following form

$$T^2 = T_0^2 + \frac{(2h_e)^2}{V_{sem}^2} \quad , \tag{3-14a}$$

with

$$T_0 = \frac{(1+\gamma_{mig})Z_0}{V_{p\ mig}} \quad , \tag{3-14b}$$

and

$$V_{sem} = \frac{2V_{p\ mig}}{1+\gamma_{mig}} \quad . \tag{3-14c}$$

Obviously, the relationship between the two-way travel time (T) and full equivalent offset ($2h_e$) in equation (3-14a) is hyperbolic. In these equations, V_{sem} means the semblance velocity obtained from the velocity analysis on the CCSP gathers using conventional velocity analysis tools. It has the similar migration velocity form given by Eaton and Stewart (1991), i.e.

$$V_m = \frac{2V_pV_s}{V_p+V_s} = \frac{2V_p}{1+\gamma} .$$

From the *P*-wave migration velocity analysis on CSP gathers, $V_{p\ mig}$ can be obtained, and by velocity analysis, V_{sem} can be obtained. Then, from equation (3-14c), the migration velocity ratio γ_{mig} and the *S*-wave migration velocity can be calculated by:

$$\gamma_{mig} = \frac{2V_{p\ mig}}{V_{sem}} - 1, \tag{3-15a}$$

and

$$V_{s\ mig} = \frac{V_{p\ mig}V_{sem}}{2V_{p\ mig} - V_{sem}}. \tag{3-15b}$$

Shown in Figure 3-6 are an example CCSP gather and its corresponding semblance velocity spectrum for synthetic *P*-*S* data, as discussed in Chapter 2. The converted-wave events on the CCSP gather are indeed hyperbolic, for the precise *P*-wave and *S*-wave migration velocities in calculating the equivalent offsets while creating the CCSP gathers. This is expected by equations (3-14) and demonstrated by the highly focused velocity semblance. Then an accurate *S*-wave migration velocity function can be obtained using equation (3-15b).

Figure 3-7 shows another example of a CCSP gather and its velocity spectrum, using conventional *P*-*P* velocity analysis, for the 3-D *P*-*S* physical model data, which will be further studied in the next chapter. In the left panel of Figure 3-7, the event at 1100 ms is the *P*-*S* reflection from the bottom of the model, whereas the event at 740 ms is *P*-wave leakage. In this example it is seen that *P*-*S* event, which is non-hyperbolic in conventional CCP gather, appears to be hyperbolic in CCSP gather. This property is quite clear in the velocity spectrum, in which the velocity semblance is highly focused. However, in Figure 3-8, because the *P*-*S* event in a conventional CCP gather is not hyperbolic, the velocity spectrum is smeared due to the assumed hyperbolic NMO equation used to calculate the velocity spectrum.

3.3.2 Practical velocity analysis and convergence

Equations (3-15) show that by performing velocity analysis on the CCSP gathers using conventional velocity analysis tool, the *S*-wave migration velocities and/or migration velocity ratios can be obtained. However, in the calculation of equivalent offsets using equations (3-13), the *S*-wave migration velocities or migration velocity ratios need to be known. This gives rise to the questions of how to practically implement velocity analysis and how the velocity error in the calculation of equivalent offset affects the velocity analysis results.

Before processing the *P*-*S* section, the *P*-wave migration velocities are generally obtained from the processing of *P*-*P* data. However, the *S*-wave migration velocities are

not known and initial estimates need to be made. Because of this, the effect of initial velocity estimation error on velocity analysis and convergence to the true *S*-wave migration velocity need to be assessed

The physical model example was used to study the effect of the velocity error on velocity analysis result. Table 3-1 shows how the velocity error in the calculation of the equivalent offset affects the velocity analysis result.

Table 3-1. The effect of *S*-wave velocity error in the calculation of equivalent offset on the result of migration velocity analysis.

V_p (m/s)	V_s (m/s)	V_s error (%)	V_{sem} (m/s)	V_s (m/s) From V. A.	relative error (%)	iteration No.
2750	825	-40%	789	1106	19.6 %	1
2750	1100	-20 %	889	1314	4.4 %	2
2750	1237.5	-10 %	894	1324	3.7 %	3
2750	1375	0 %	905	1349	1.9 %	4

In this example the *P*-wave velocity was kept the same as the *P*-wave migration velocity while changing the *S*-wave velocity. From Table 3-1, it is known that when the velocity error is less than 20 %, reasonably accurate velocity result can still be obtained. This means that the CCSP gather and velocity analysis are fairly insensitive to the velocity error. In practice, after the velocity function is obtained by the velocity analysis on a CCSP gather, the output velocities are input to update the equivalent offset CCSP gather and the velocity analysis can be repeated. Very importantly, the updated velocity function converges through this iteration procedure, and an accurate velocity function can finally be reached. For example, with the initial *S*-wave migration velocity of 850 m/s, after 3 or 4 iterations, the final *S*-wave migration velocity with relative error less than 1.9% can be obtained. Because the algorithm is very fast and flexible, this kind of iterative procedure is practical.

3.4 Application and discussions

Numerical simulation might be the easiest way to evaluate the feasibility of experimental design and data processing without the cost of field acquisition. In this section, the new algorithm is applied to a 3C-3D numerical model. Then the comparison of this new method with conventional NMO+DMO+poststack migration or prestack migration is principally studied. Finally, based on the application, the effect of 3C-3D geometry design on prestack migration is discussed.

3.4.1 Application to 3C-3D numerical model

A synthetic data set created by using ray-tracing software was used to demonstrate the feasibility of the *P*-*S* prestack migration and migration velocity analysis by equivalent offsets and CCSP gathers. The model was described in detail in section 2.4.1. The model consists of four layers with depth variant velocities (*Vp* and *Vs*) and velocity ratio (γ). The third interface contains a pyramid with different dipping angles. The data acquisition geometry was also discussed in section 2.4.2. Because of the limitation of the modeling package and other facilities, the average fold using natural bin grid is relatively low and only about 18. The effect of the 3-D geometry design on the prestack migration is discussed in detail later in this chapter.

Before the application of converted-wave prestack migration, the only pre-processes applied were "geometry" and "front mute" using ProMax. For this kind of prestack migration algorithm, and perhaps for all of the prestack migration algorithms which are not based on full wave equation, converted-wave energy after critical angle will deteriorate the migration result, unless phase corrections are made.

As discussed previously, the *P*-wave velocities in the application of prestack migration should be the final *P*-wave migration velocities. However, the *P*-wave RMS velocities derived from the model were used as the *P*-wave migration velocities in this example due to the following reasons: Firstly, the *P*-*P* data set was not acquired or processed, so it was not possible to get the *P*-wave migration velocities. Secondly, the *P*-wave migration velocities are very close to the RMS velocities at the depth of interest and thirdly, the calculation of equivalent offset is fairly insensitive to the velocities, so the *P*-wave RMS velocities are accurate enough to yield a good migrated image. The *S*-wave migration velocities for the final iteration were obtained using the iterative procedure,

starting with a constant *S*-wave migration velocity. The final *S*-wave migration velocities are very close to the theoretically derived *S*-wave migration velocities.

Example *P*-*S* stacked sections after prestack migration corresponding to cross-sections in Figures 2-7a and 2-7b are shown in Figures 3-9 and 3-10 respectively. At first, by comparing the stacked sections after prestack migration with the model, it is demonstrated that this method can successfully migrate the dipping reflections to their true positions. Secondly, the image for the first reflection is spatially aliased in Figure 3-10, but it seems reasonably good in Figure 3-9. The possible explanations are (1) the critical offset (the offset at the critical angle) for the first layer is small, so the muted offset for this layer is small, only about 700 m; (2) because of this, the actual fold for this event is very low, so there are not enough spatial samples to recreate the seismic image by constructive or destructive interference in the prestack migration; (3) the bin size in cross-line direction is twice as large as that in in-line direction, therefore the spatial aliasing in Figure 3-10 is stronger than in Figure 3-9. Finally, as shown in Figure 3-9, there are two diffraction events at points A and B where the dip angles change very fast. They seem to be migration "noise", but they are caused by the fact that ray-tracing fails to simulate the diffractions at these points, so the prestack migration smears the energy of a spike along the converted-wave migration trajectory.

3.4.2 The comparison with conventional NMO+DMO+poststack migration or prestack migration

Compared with conventional NMO+DMO+poststack migration or prestack migration, this new algorithm is fast and stable. As discussed in the section of practical computation of equivalent offset and shown in Figure 3-5, blocks of samples are moved to the appropriate equivalent offset bins in this new algorithm, but in the conventional NMO+DMO+poststack migration or prestack migration processing, the energy at a given time sample is smeared out along the DMO or prestack migration trajectory. Although the equivalent offset bin size may affect the accuracy of the prestack migration result, especially for the early events and high frequency content, this kind of effect is negligible by using the appropriate bin size, at certain depth of interest and in conventional frequency band.

Generally, NMO+DMO+poststack migration is more stable than conventional prestack migration in the case of velocity uncertainty, particularly if the lateral velocity variation is not very strong. This can be better understood by analyzing their difference in repositioning a time sample to its "true" position. As shown in Figure 3-11, the two

approaches try to move the converted-wave energy from the recorded position to its "true" position, but the methods are different. In NMO+DMO+poststack processing, at first, the sample is vertically (time) moved to the so-called zero-offset position using velocity V_1, which is generally obtained from the velocity analysis. If the velocity model is not horizontally homogeneous, then the common conversion point approximation is no longer the common spatial point, so DMO processing is used to remove the dispersion of the common conversion point. After DMO processing and reverse NMO correction, velocity analysis can be repeated on the CCP gather and a more accurate velocity V_2 can be obtained. Finally, the new velocity is used for NMO and poststack migration. In conventional converted-wave prestack migration, the sample is directly moved to the "true" position. If the initial velocity V_1 is accurate and constant, this two approaches are almost identical. But if the initial velocity V_1 has some error, the NMO+DMO+poststack is more stable than conventional prestack migration, because (1) DMO processing has smaller aperture than that of prestack migration; (2) after DMO processing, the new velocity V_2 velocity analysis result is more accurate than V_1, therefore NMO correction and poststack migration are more accurate.

Prestack migration by equivalent offsets and CCSP gathers and its velocity analysis have advantages over the two approaches discussed above in the sense of stability to the velocity error. Comparison of Figure 3-12 and Figure 3-11 shows that as the first step in this new algorithm, CCSP gathering does not move the sample vertically, but only moves the sample horizontally to its corresponding offset bin to force the converted-wave event to be hyperbolic, so CCSP gathering is fairly insensitive to velocity error. Velocity analysis on these migrated CCSP gathers is more effective because the converted-wave events are hyperbolic whether the CCSP surface location is over a flat reflector or dipping reflector. So a more accurate migration velocity $V_2^{'}$ can be obtained and is used in NMO correction. More importantly, because the algorithm is very fast and flexible, it is possible to get a more accurate velocity functions by iteration procedure discussed early.

3.4.3 The effect of 3C-3D geometry design on prestack migration

Prestack migration, as well as DMO, is a process that reconstructs the seismic image by wavelet constructive or destructive interference. In order to achieve this, seismic data should have an adequate number and even distribution of time and spatial samples. Fold, offset and azimuth distributions are important factors that might affect 3D prestack migration result. These factors are more important in 3C-3D prestack migration than in conventional 3D prestack migration, because (1) the actual fold may be much lower than

the nominal one, and the fold distribution is depth-variant and generally not even; (2) the offset distribution may be quite uneven and sparse due to the inner and top mutes; (3) because of the above reasons, the azimuth distribution may be very poor. In the following, the effect of fold and offset distribution on prestack migration is briefly studied, based on the application of this new algorithm to the numerical model.

Figure 3-13a is the converted-wave fold map using asymptotic CCP binning with V_p/V_s ratio of 2.0. The fold map is calculated based on the data acquisition geometry as shown in Figure 2-8. From this fold map, it is seen that the average fold for the whole data acquisition is about 15. In the migration aperture zone, the fold range is from 18 to 32. Different from the fold distribution for *P-P* wave processing, the converted-wave fold map for this special data acquisition geometry has zero fold for every fourth in-line bins along the cross line direction if standard *P-S* bin sizes are used. But this fold distribution is not the actual fold distribution in the processing after applying front and inner mutes when the zone of interest falls in these mute zones. Figure 3-13b is the fold map after muting the offsets which are larger than 2000 m. Comparison between Figures 3-13a and 3-13b shows that the fold in the migration aperture zone is greatly reduced after mute. In order to mute the offsets after critical angle, the actual fold for shallow (early time) events is very low. As an example, Figure 3-13c is the actual asymptotic CCP fold map for the first event (corresponding to time of 400 ms). The maximum fold for this case is less than 10 and the average fold is surprisingly low. This can help to explain why the first reflection in the CCSP gathers as shown in Figures 3-14 is not as good as the second reflection, although they both are from flat interfaces.

The offset and azimuth distributions have significant effect on prestack migration result. In this Kirchhoff style migration algorithm, bad offset and azimuth distribution might result in bad image for some of the equivalent offset bins, because there are not enough spatial samples to reconstruct the new image by constructive or destructive interference. Shown in Figures 3-14 are the two CCSP gathers at different surface locations. Obviously, the nearest offset in Figure 3-14a is much larger than that in Figure 3-14b. By comparing the converted-wave events for different equivalent offset bins in the same CCSP gather, it is found that the result in some offset bins is better than the others, mainly due to uneven offset and azimuth distributions. This problem can be more understandable by comparing the CCSP gathers in 3C-2D case (Wang et al., 1995).

3.4.4. Application to Lousana 3C-2D field data set

In the numerical modeling example, the data are noise free, and the geometry is regular. This is rarely true in real data. To demonstrate the new algorithm further, it was applied to multicomponent seismic data from Lousana, Alberta. Data acquisition and previous processing were discussed in greater detail by Miller et al. (1994). In 1994, the data were reprocessed for both the vertical and radial components. The migrated *P*-*S* section processed in 1994 for Line EKW-002 is shown in Figure 3-17. *P*-*S* velocity analysis on conventional CCP super gather is shown in Figure 3-15, while the velocity analysis on CCSP gather after prestack migration discussed in this chapter using conventional *P*-*P* velocity analysis tool is shown in Figure 3-16. Although a CCP super gather with 9 CCP gathers was formed to perform velocity analysis in Figure 3-15, the result in Figure 3-16 is still better than in Figure 3-15. This improvement can be seen in the highly focused velocity semblance and higher signal-to-noise ratio.

The *P*-*S* stacked section for Line EKW-002 after prestack migration is shown in Figure 3-18. Compared with Figure 3-17, the bandwidth in this figure is approximately the same, but the Viking horizon (the peak at about 1550 ms) and the Nisku event (the peak at about 1990 ms) are improved and signal-to-noise ratio is also higher. The prestack migrated section in Figure 3-18 seems more interpretable than in Figure 3-17.

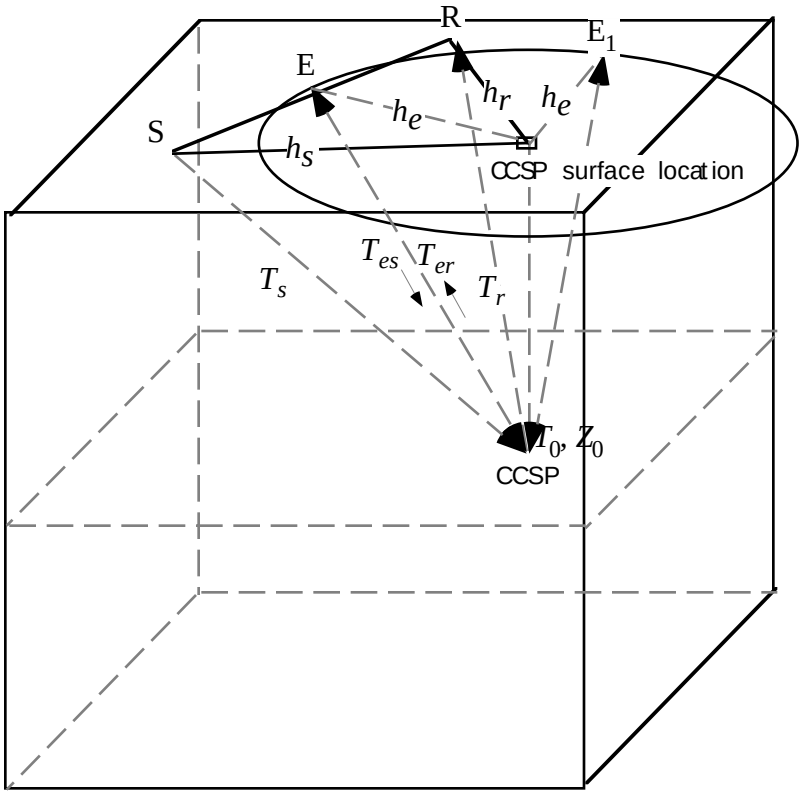

FIG. 3-1. Diagram showing the ray paths and travel times for a common conversion scatter point in a 3-D volume.

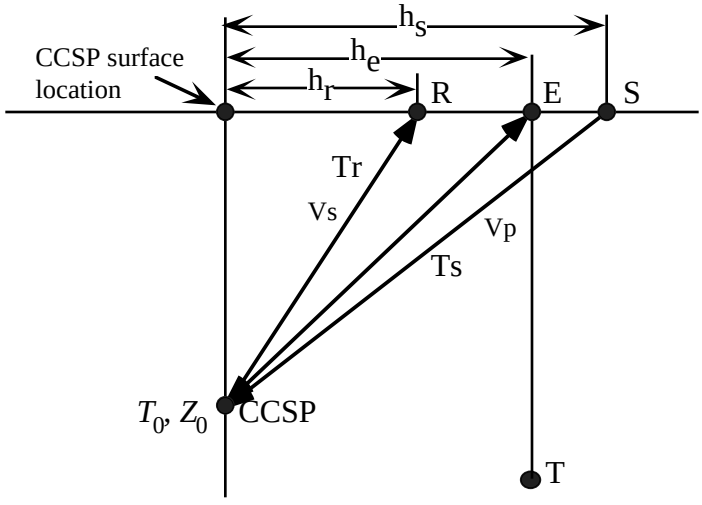

FIG. 3-2. The ray paths and travel times for a common conversion scatter point and the position of the equivalent offset when the source, receiver and CCSP are in the same plane.

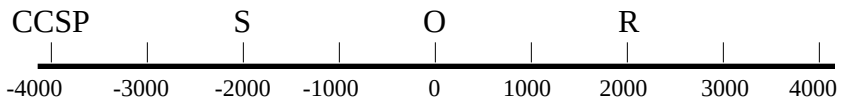

S: Source position
R: Receiver position
O: Midpoint of S to R

Vp=3000 m/s
Vs=1500 m/s
offset=4000 m

(a)

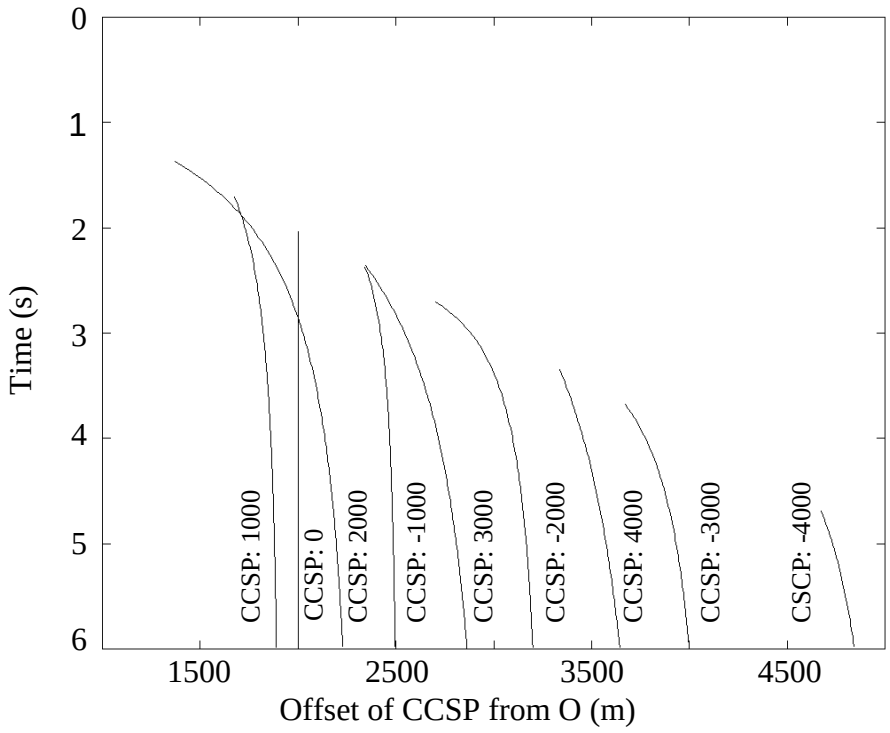

(b)

FIG. 3-3. The geometry of different CCSP locations on the surface (a) and the equivalent offsets at different locations as the function of time (b).

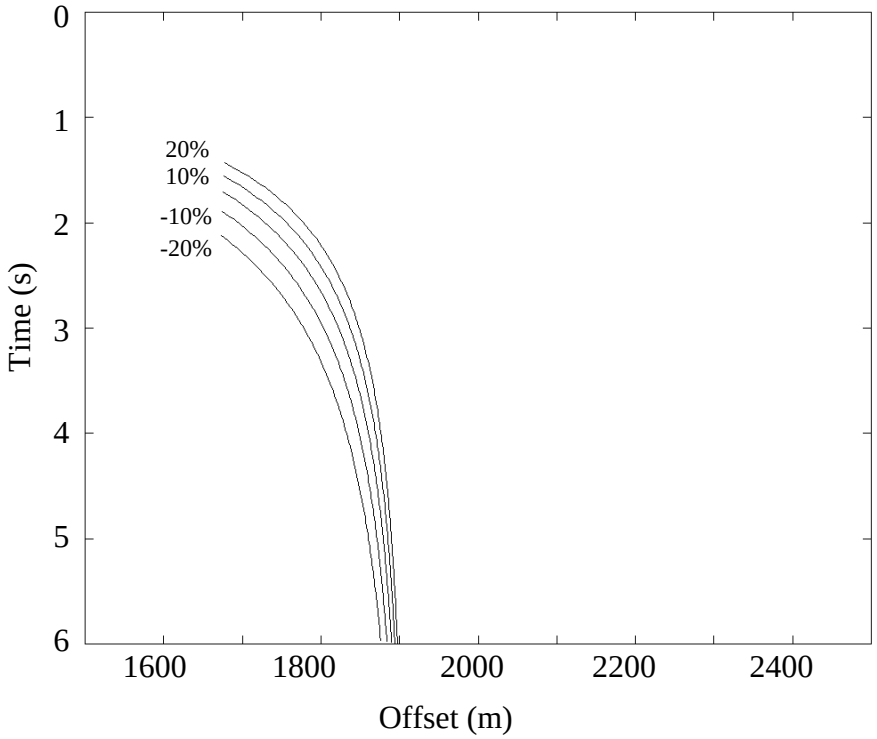

FIG. 3-4. The effect of velocity error on the accuracy of equivalent offset. The CCSP surface location is at 1000 m as shown in Figure 3-3a, and the other parameters are the same as in Figure 3-3a.

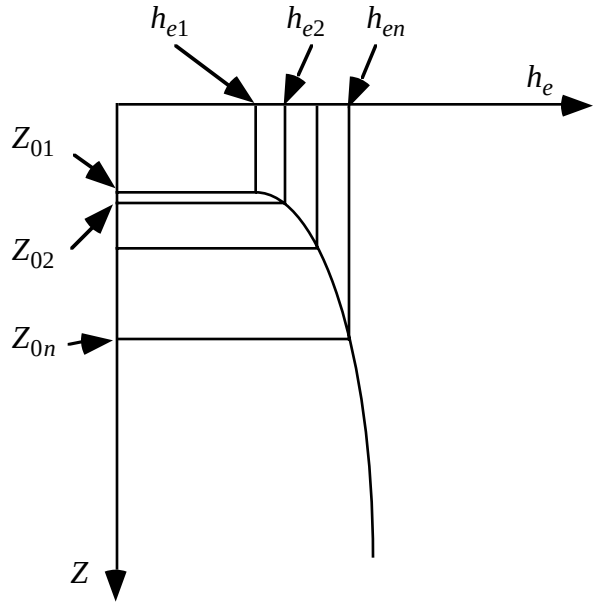

FIG. 3-5. Diagram showing how to implement calculation of equivalent offset.

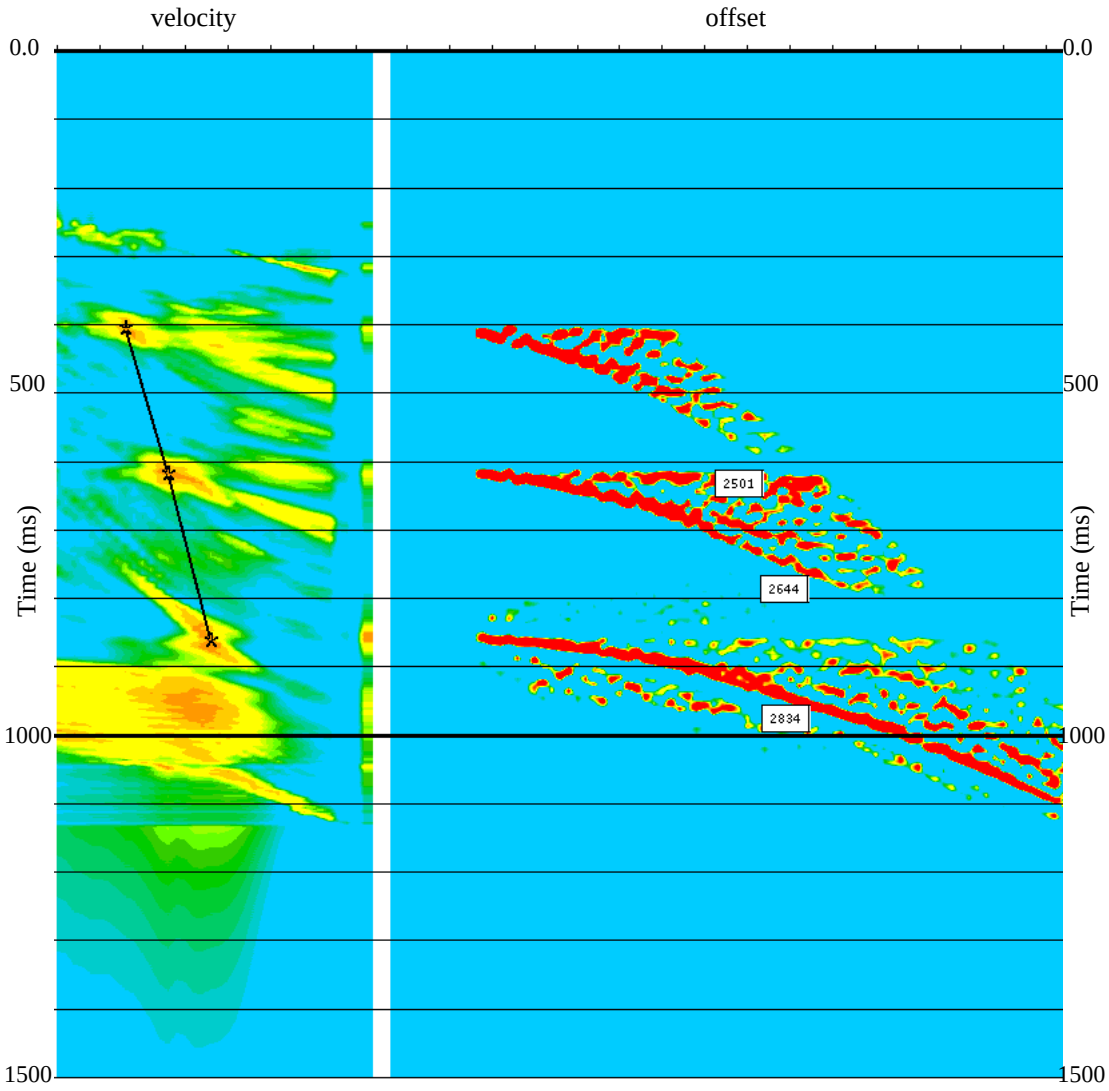

FIG. 3-6. 3-D *P-S* velocity analysis after CCSP gathering. On the left is the semblance velocity spectrum and the picked velocities. On the right is the CCSP gather. On the semblance display, the relatively strong noises are due to the coherent events with very small amplitude on the synthetic data.

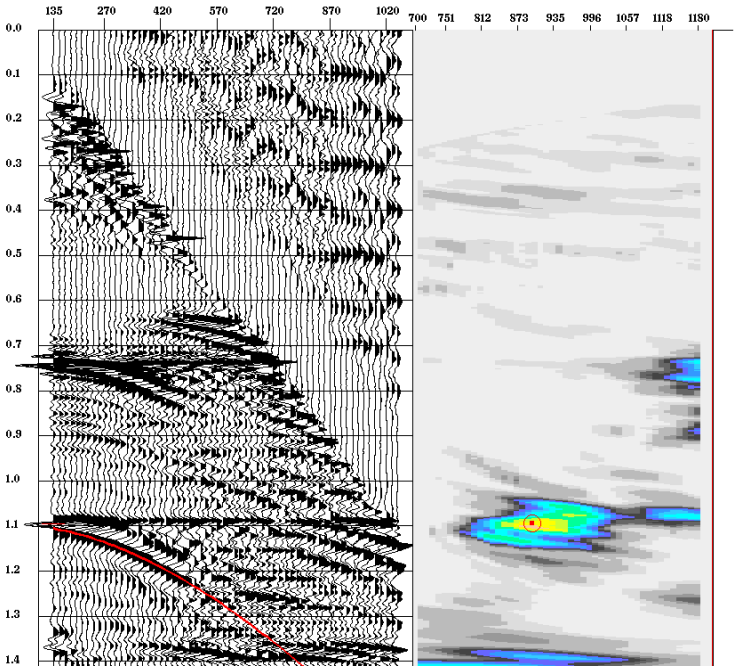

FIG. 3-7. The semblance velocity analysis of *P-S* CCSP gather using conventional velocity analysis method. Notice that in CCSP gather, *P-S* event is hyperbolic.

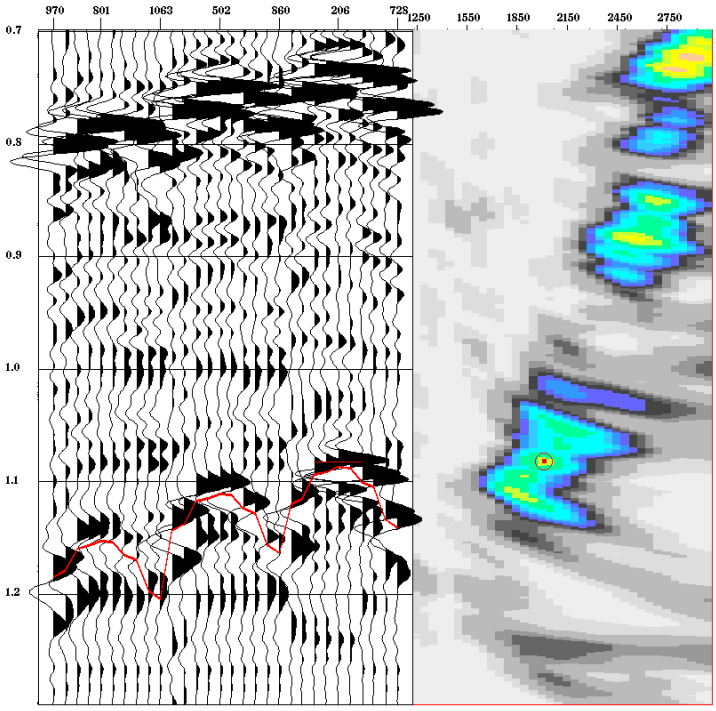

FIG. 3-8. The semblance velocity analysis of conventional CCP gather. Notice the smear of the semblance for the *P-S* event at time 1100 ms. This means that *P-S* event is not hyperbolic.

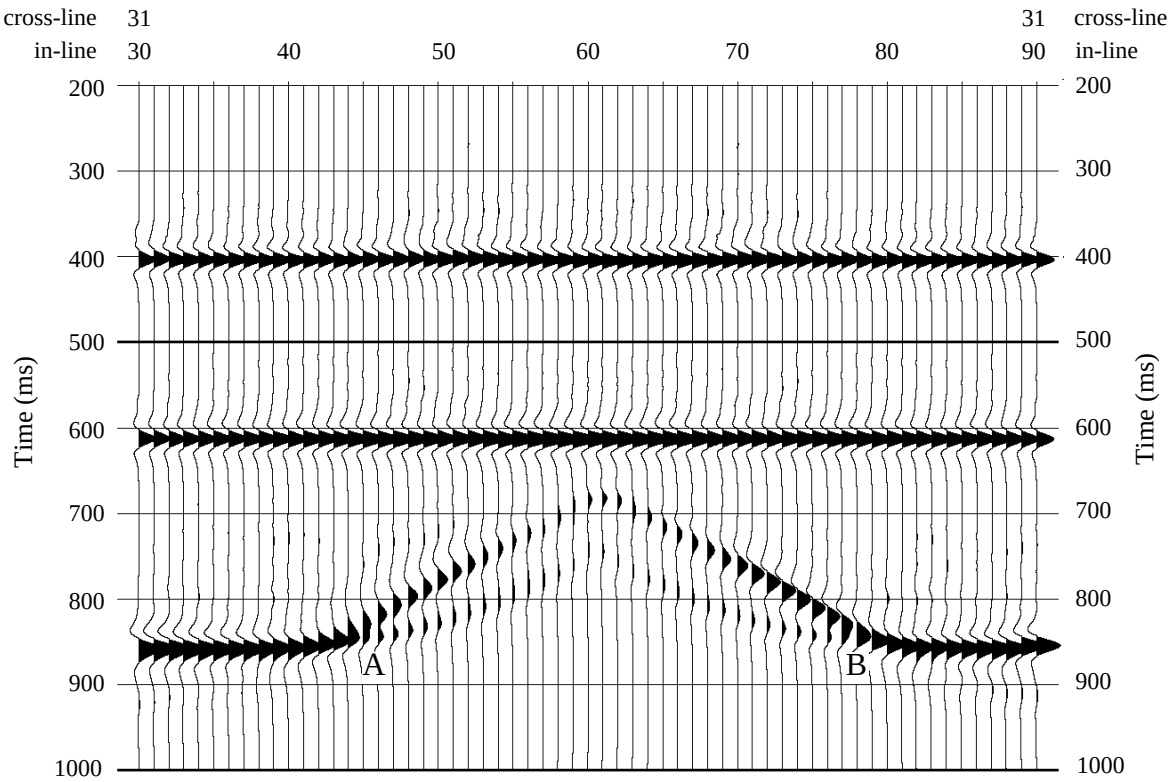

FIG. 3-9. Example of 3-D stacked section after prestack migration. The cross section is at the same position and direction as the cross section in Figure 2-7(a).

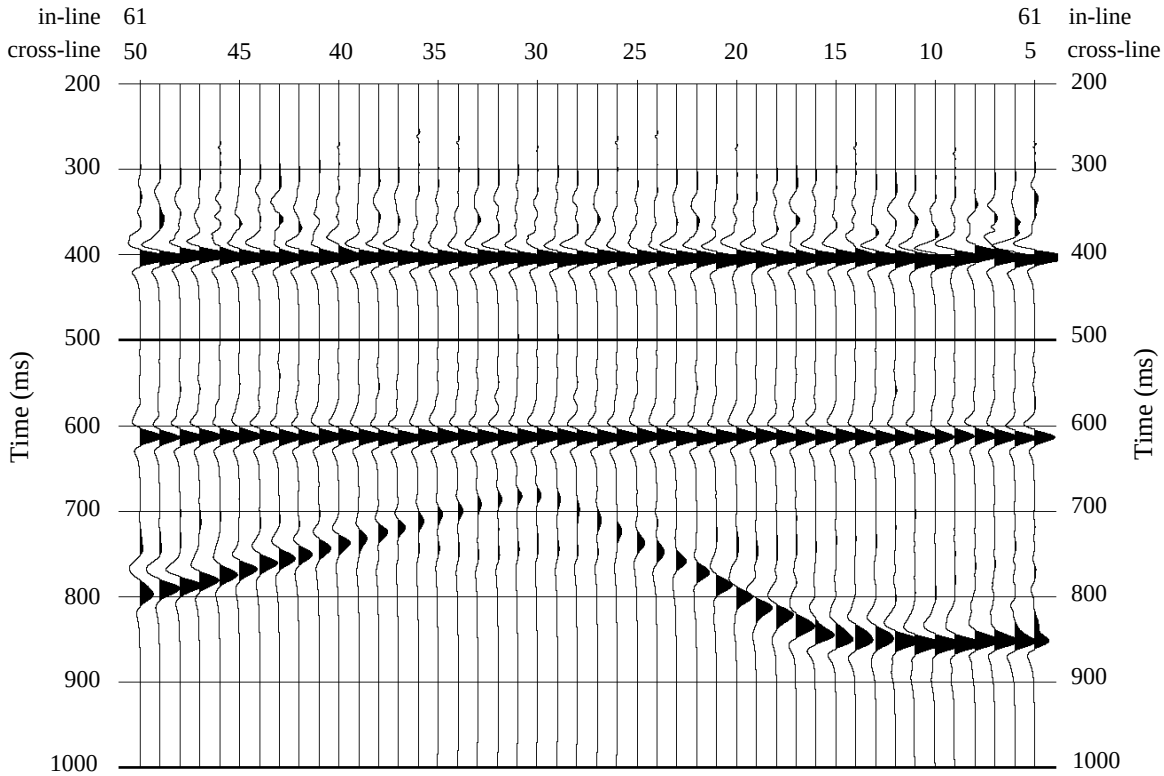

FIG. 3-10. Example of 3-D stacked section after prestack migration. The cross section is at the same position and direction as the cross section in Figure 2-7(b).

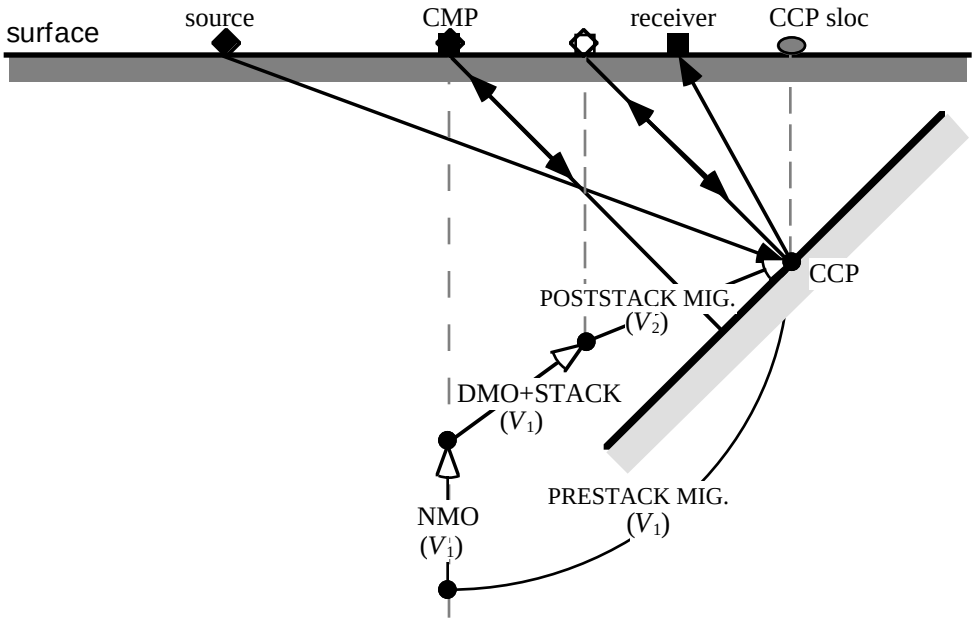

FIG. 3-11. The diagram showing how conventional converted-wave NMO, DMO, poststack migration and prestack migration move a time sample vertically and/or horizontally.

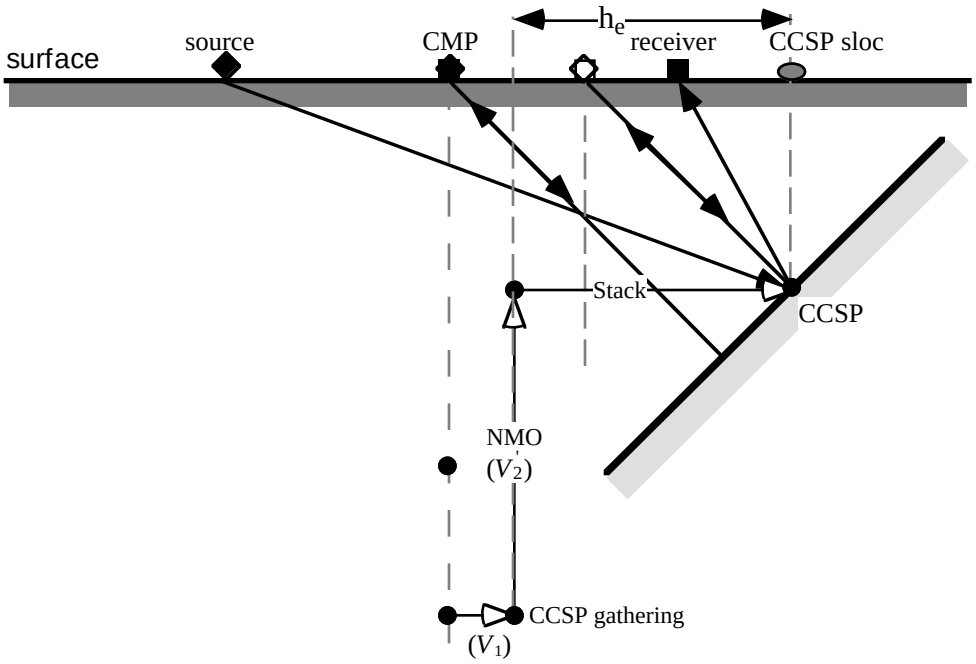

FIG. 3-12. The diagram showing how converted-wave prestack migration by equivalent offset CCSP gather (CCSP gathering, NMO and stack) moves a time sample vertically and/or horizontally.

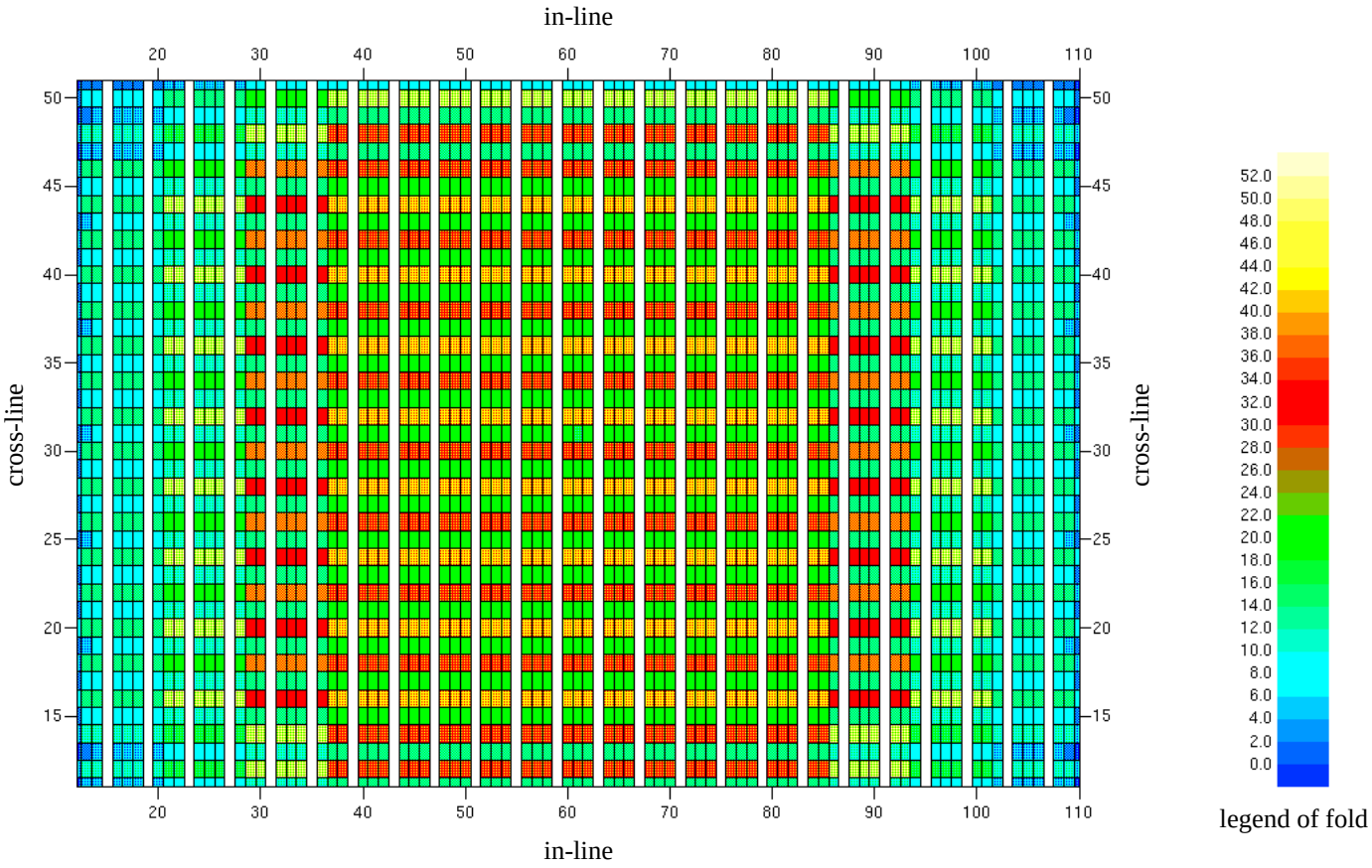

FIG. 3-13a. *P-S* converted-wave fold map after asymptotic CCP binning. All of the traces are used in the CCP binning.

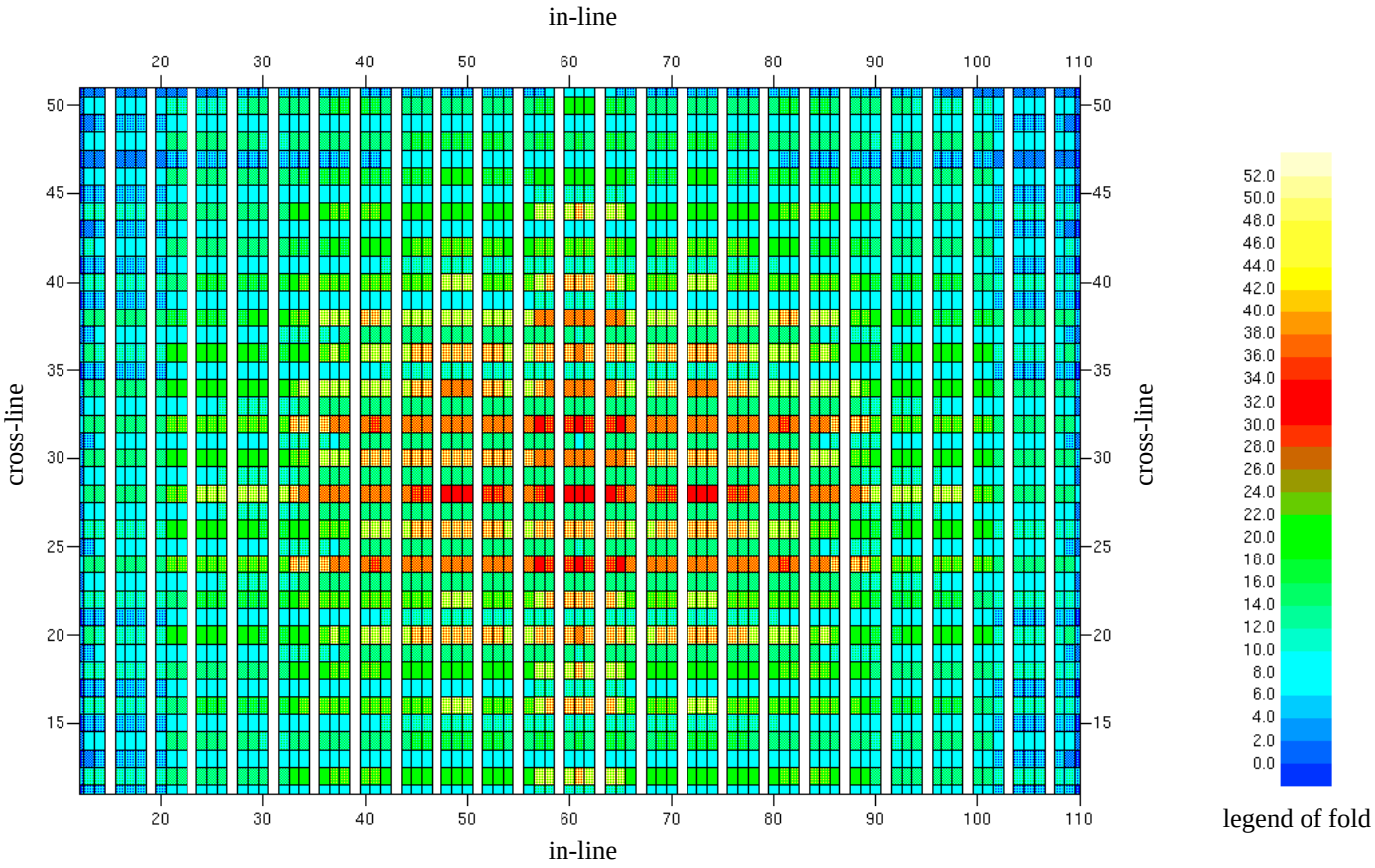

FIG. 3-13b. *P-S* converted-wave fold after asymptotic CCP binning. Only the traces with offsets of less than 2000 m, are used in the CCP binning.

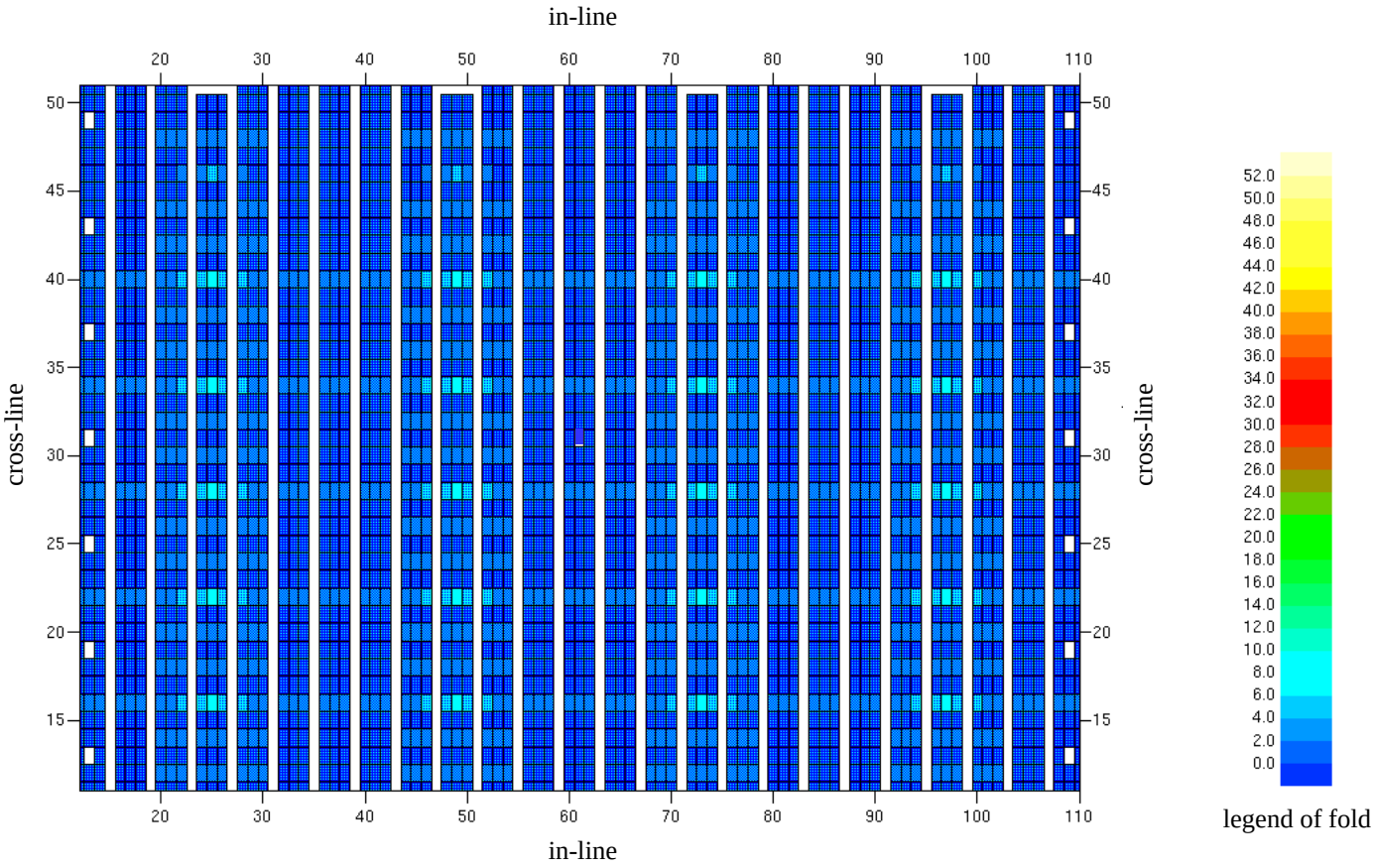

FIG. 3-13c. *P-S* converted-wave fold map after asymptotic CCP binning. Only the traces with the offsets are less than 700 m, are used in the CCP binning.

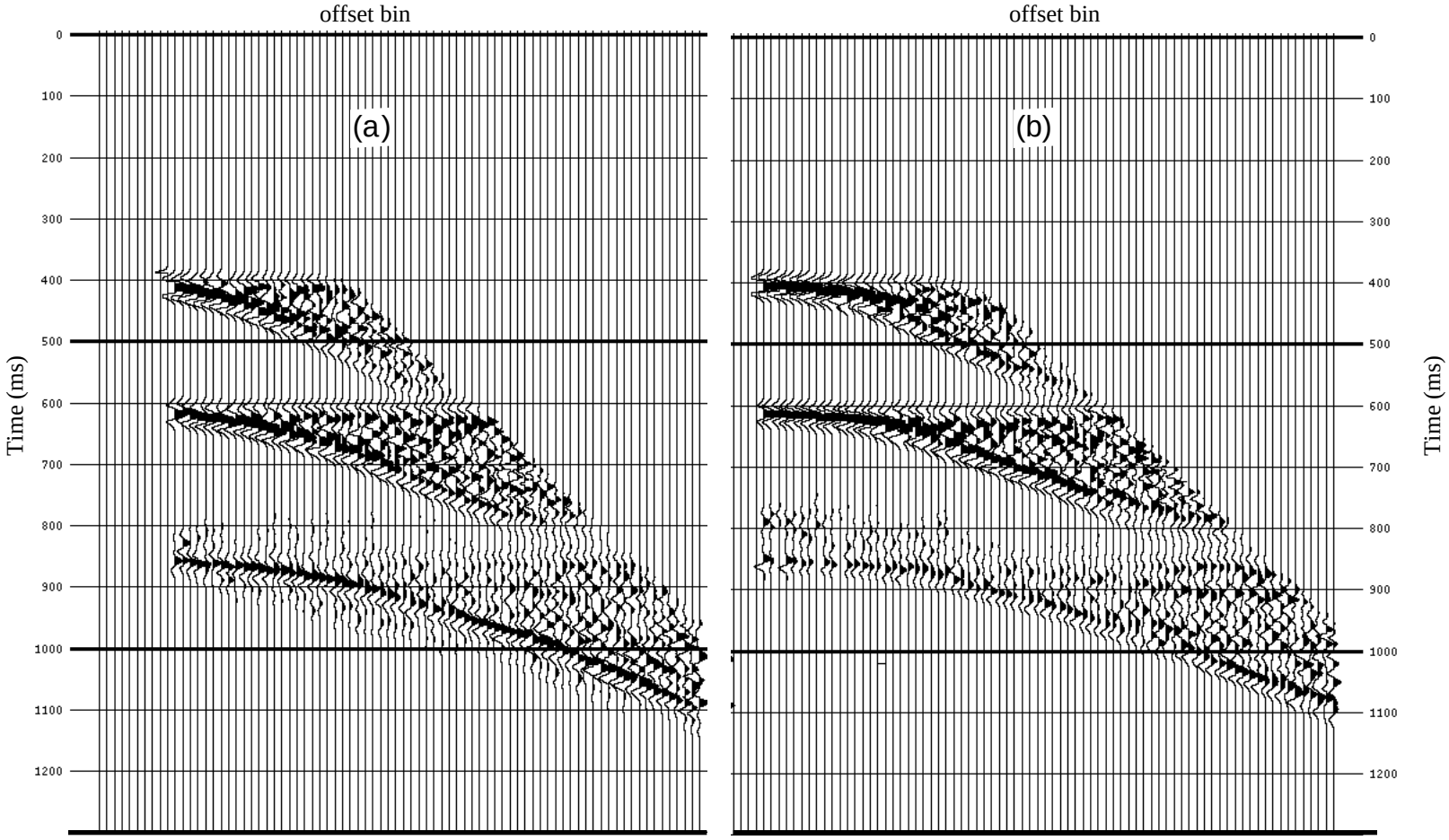

FIG. 3-14. Two CCSP gathers showing a difference in the nearest equivalent offsets, and qualities that vary with equivalent offset bins. (a). the CCSP gather is at CDP = 2967, Cross-line = 31, In-line = 32, and the nearest offset is 262.5 m; (b). the CCSP gather is at CDP = 2978, Cross-line = 31, In-line = 41, and the nearest offset is 112.5 m.

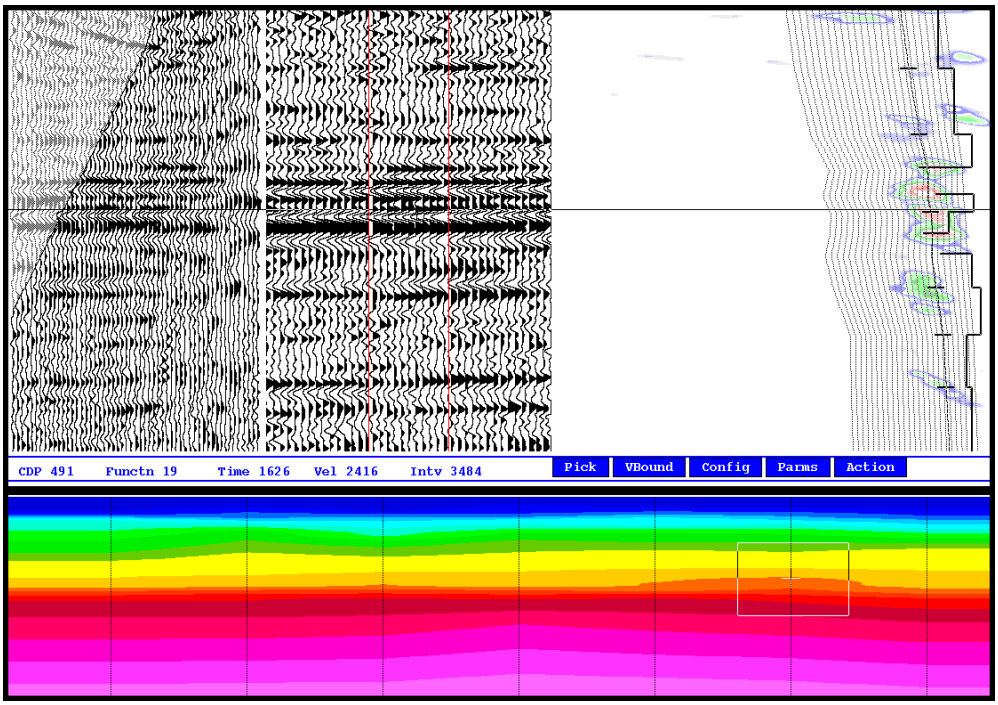

FIG. 3-15. *P-S* velocity analysis on conventional CCP super gather. The super gather consists of 9 CCP gathers.

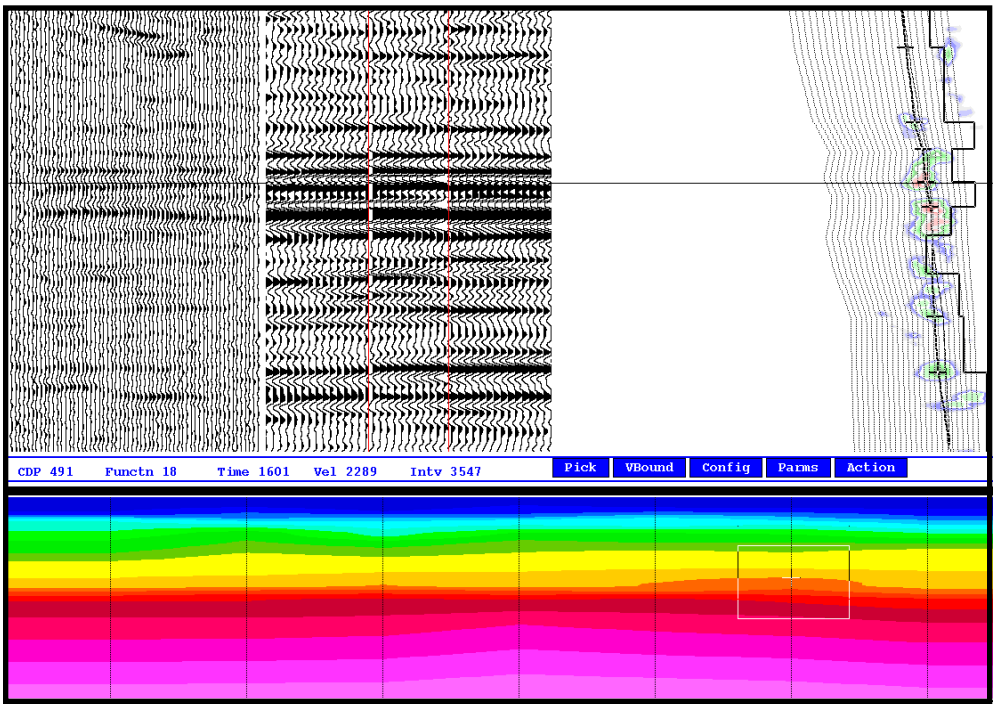

FIG. 3-16. *P-S* velocity analysis on CCSP gathered data discussed in this thesis using conventional velocity analysis tool. Note more focused velocity semblance than in Figure 3-17 and improved signal-to-noise ratio.

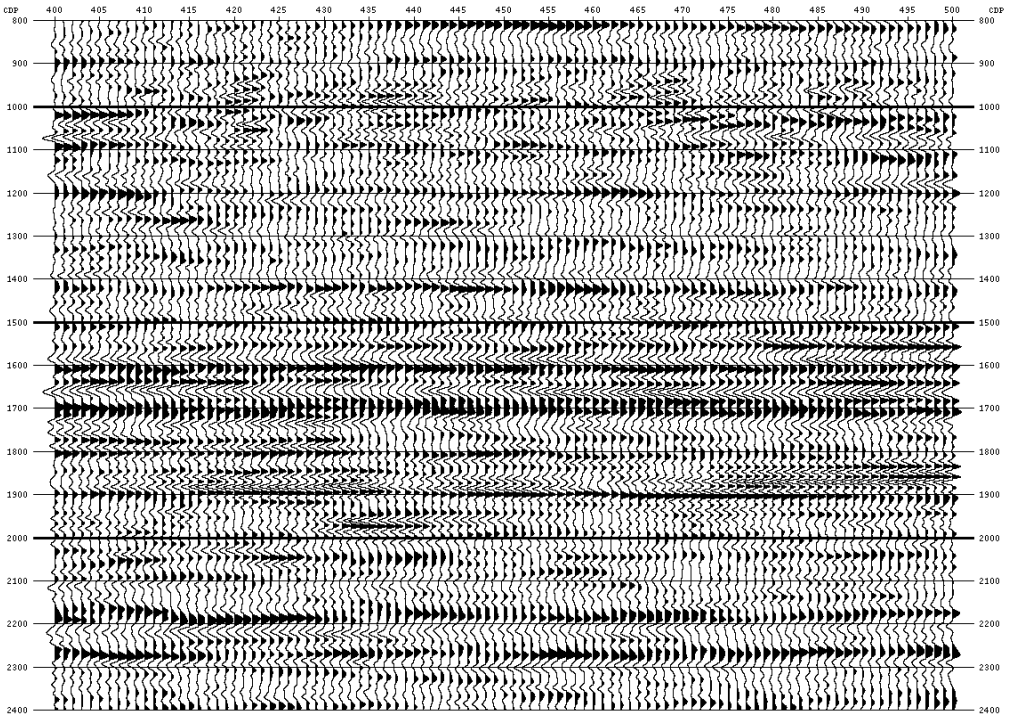

FIG. 3-17. The migrated section using conventional *P-S* processing

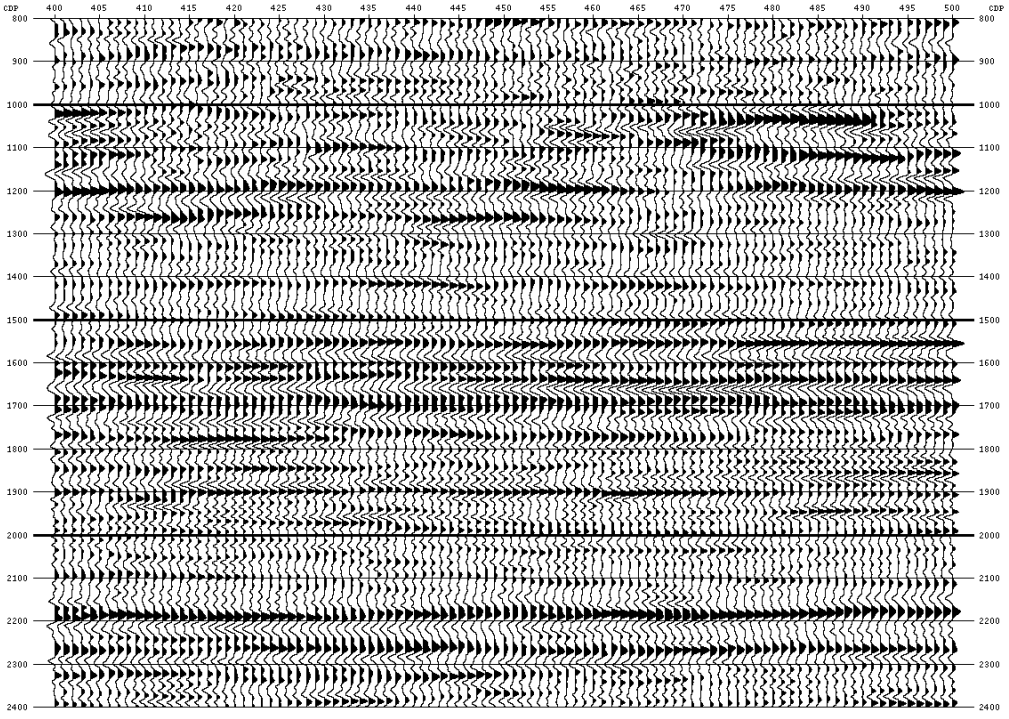

FIG. 3-18. The *P-S* stacked section for Line EKW-002 after CCSP gathering. Compared with Figure 3-17, it has almost the same bandwidth, but the imagings of the Viking horizon (the peak at about 1550 ms) and the Nisku event (the peak at about 1990 ms) are improved and the signal-to-noise ration is also improved.

Chapter 4 - Application of 3C-3D processing flow to physical model seismic data

4.1 Introduction

Numerical simulation and/or physical modeling are techniques which are often used to evaluate the feasibility of experimental design and data processing without the cost of field acquisition (Chen et al., 1993; Ebrom et al., 1990; Chon and Turpening, 1990). Physical modeling is a very useful way to evaluate experimental design, data processing algorithms and interpretation methods in that the model and acquisition geometry are controlled, yet the data have many of the characteristics of field data (Chen et al., 1993). In physical modeling, discretization in numerical modeling is not needed, approximations and assumptions may be avoided, and roundoff errors need not accumulate. Furthermore, compared to numerical modelling methods, physical models suffer from all of the experimental errors that plague actual field work, such as positioning uncertainties, dynamic-range limitations and undesired (but real) interfering events (Ebrom et al., 1990).

In this chapter, with the aid of a 3-D *P*-*S* physical modeling dataset over a three-dimensional model, two data processing flows for converted-waves are evaluated.

4.2 Model description

The 3-D physical model consists of a rectangular-shaped cavity milled into the base of a layer of plexiglas 9.8 cm thick; Plexglas has a *P*-wave velocity of 2750 m/s and an *S*-wave velocity of 1375 m/s. Cross-sections showing the geometry of the model are shown in Figure 4-1. The cavity is about 1.4 cm deep, 8.0 cm long, 5.0 cm wide and is air-filled. As seen in Figure 4-1, the model is symmetric in the in-line (receiver-line) direction and asymmetric in the cross-line (shot-line) direction. Other parameters about the model are also shown in Figure 4-1. World units are shown using a distance scaling factor of 10,000:1.

A time scaling factor of 10,000:1 and a velocity scaling factor of 1:1 were used to convert from experimental to world units.

4.3 Data acquisition

A three-dimensional, three-component dataset was acquired over the model using a *P*-wave transducer as the source. A plan view of the survey is shown in Figure 4-2. All dimensions and parameters are referred to in world units. There were 7 shot lines recorded with line spacing of 200 m, 19 shots per shot-line and shot spacing of 50 m. For each shot, data were acquired along 10 receiver lines with a spacing of 100 m, a near offset of 200 m, 18 receiver stations per receiver line and a receiver spacing of 50 m. Each shot line lay 200 m from the active receiver patch. The sample interval was 1 ms and the record length was 1.5 s. The survey was repeated three times to enable vertical, in-line and cross-line receiver components to be collected. Here, in-line refers to the receiver-line direction and cross-line refers to the shot-line direction.

Figure 4-3a is an example of the collected data, showing a shot gather for the in-line receiver component with a *P*-wave source located at station 9 of shot line 1. The receivers for this gather were along receiver line 5; i.e. the shot and receivers lie in the same plane. For this shot gather, which is located over the flat part of the model, the main reflection events are the *P*-*S* (event 2) and *P*-wave leakage (event 1) from the flat interface at the bottom of the model. By carefully examining event 2, it is clear that for near-offset traces, *P*-*S* amplitudes are smaller than traces with medium offsets. This is because at small offsets, the *P*-wave incident angle is small, and mode-converted energy is weak according to the principle of partitioning of energy at an interface.

Figure 4-3b shows another in-line component shot gather with a *P*-wave source at station 9 of shot line 3. The receivers are still along receiver line 5, but now cover the structured part of the model. In this figure, events 1 and 1a are the *P*-wave leakage from the flat interface and the top of the 3-D model respectively, whereas events 2 and 2a are *P*-*S* reflections from the flat basal interface and the top of the cavity respectively.

4.4 Data processing

After a quality data set is acquired, an appropriate processing flow is the key to yield an interpretable seismic image. Conventionally, the 3-D *P-P* volume is processed to the final migrated stack to get the *P*-wave stacking or migration velocities before processing the converted-wave volume. In this application, although 3C-3D data were collected, the primary interest in this experiment is to evaluate the 3-D *P-S* data processing flow. However, for the purpose of comparison, the *P-P* wave dataset was also processed using a conventional 3-D processing flow. In this section, the two processing flows are described and evaluated. One is the conventional 3-D *P-S* processing flow and the other is the 3-D *P-S* processing flow with prestack migration.

4.4.1 Conventional 3-D converted-wave processing

The processing flow chart developed for isotropic 3-D *P-S* data is shown in Figure 4-4. Some special processes, such as component rotation, *P-S* NMO correction and common conversion point (CCP) binning were applied. Component rotation (Lane and Lawton, 1993) was applied to transfer the in-line and cross-line components into radial and transverse components for each source-receiver azimuth. Asymptotic common conversion point (CCP) binning proved to be an adequate binning method for this dataset since the depth of interest is quite large compared to the offset range. A *P-S* NMO correction (Slotboom et al, 1990) was also implemented.

As shown in Figure 4-5, after recording two horizontal components for each source-receiver azimuth (in-line (X) and cross-line (Y) components), the data were rotated into radial and transverse components with respect to the source-receiver azimuth. The rotation was undertaken so that *P-P* events on the processed vertical component were of the same polarity as the *P-S* events on the processed radial component. In the isotropic case, the radial component will contain only *P-S* data while the transverse component should be nulled. Figures 4-6a and 4-6b are examples of data from in-line and cross-line component respectively for shot station 1 on shot line 1. In this example, only the data on the first 5 receiver lines are displayed. The *P-S* event is between times 1.05 s and 1.25 s and this event can be seen not only on the in-line component but also on the cross-line component. With different source-receiver azimuths, the amplitudes of the *P-S* event on different lines vary. With the receiver line number increasing, i.e. the receiver lines are away from the shot position and the source-receiver azimuths are increased, the *P-S* energy on in-line

component is weaker, whereas on cross-line component this event becomes stronger. After component rotation, it is clear that the *P*-*S* energy is almost all on the radial component (Figure 4-7a), whereas that on the transverse component is very weak (Figure 4-7b). Ideally, the *P*-*S* energy on the transverse component should be zero, but because of the large size of the transducer and minor positioning errors, some *P*-*S* energy leaked onto the transverse component.

A key step in *P*-*S* data processing is common conversion point (CCP) binning. As shown in Figure 2-1 in Chapter 2, the conversion point lies between the source and receiver, but is displaced toward the receiver position from the midpoint. The exact location depends on V_P/V_S and on the depth of the conversion point (Eaton et al., 1990). However, if the ratio of offset to depth of interest is not very large, we may consider the asymptotic location as a first approximation for binning and stacking purposes. As denoted in Figure 2-1 in Chapter 2, the horizontal distance (Xp) of the asymptotic location away from the source is given by

$$X_p = \frac{X_s}{1+V_s/V_p},$$

where X_s is the source-receiver offset and V_p and V_s are the *P*- and *S*-wave velocities respectively. For this experiment, the maximum horizontal position error between asymptotic common point and the true common point at the depth of interest is only 7 m, which is far smaller than the bin size (25 m).

The fold map for asymptotic CCP binning is shown in Figure 4-8. In this figure, the bin dimensions in in-line and cross-line directions are half of the receiver interval, and half of the shot interval, respectively (both are 25 m). From this fold map, it is seen that every fourth row in the receiver-line direction is empty. This is because when a conventional common midpoint bin size of half the receiver interval ($\Delta r/2$) is used, the fold distribution is highly variable and empty rows of bins parallel to the shot lines may result for the case when $V_p/V_s=2$ and the shot line spacing is an even integer multiple of Δr (Lawton, 1993). To overcome this problem, the optimum bin size in asymptotic CCP binning is proposed by Lawton (1993). In this method, the optimum bin size ΔX_c was given by:

$$\Delta X_c = \frac{\Delta r}{1+V_s/V_p}.$$

For this physical modeling dataset, Δr=50m, V_s/V_p=0.5, and the optimum bin size ΔX_c is 33.3 m. The fold map using asymptotic CCP binning with the optimum bin size is shown in Figure 4-9, in which the fold distribution is much more even than that with a bin size of 25 m and the empty bins have disappeared.

Before stacking, correction for normal moveout (NMO) was applied to the dataset. The *P*-*S* NMO curve differs from *P*-*P* NMO curve. The standard hyperbolic NMO formula has limited application to converted-wave NMO, particularly when data with high offset-to-depth ratio are used. Therefore, a time-shifted hyperbolic NMO formula (Slotboom, et al., 1990) was applied,

$$t = \frac{t_0}{2} + \sqrt{\frac{t_0^2}{4} + \frac{X_s^2}{2V_{ps}^2}},$$

where V_{ps} is the *P*-*S* stacking velocity. For a constant velocity model, it has the form of V_{ps}=$\sqrt{V_p V_s}$ (Slotboom and Lawton, 1989 and Tessmer and Behle, 1988). Figures 4-10 and 4-11 show examples of NMO-corrected data using the standard hyperbolic equation and time-shifted hyperbolic equation. Carefully examining the *P*-*S* event, it is seen that the result of using time-shifted hyperbolic equation with effective *P*-*S* stacking velocity is slightly better than that when the standard hyperbolic equation is used. This is because the offset-to-depth ratio in this case is not very large, so both of these methods will provide good results.

Figure 4-12 shows an example section of *P*-*S* stacked data in the receiver-line direction, gathered with a bin size of 25 m. For every four traces, there is an empty trace. After linear interpolation of these empty traces, the results are shown in Figure 4-13. When the optimum bin size of 33.3 m is used in the asymptotic CCP binning, an example section of *P*-*S* stacked data is shown in Figure 4-14, in which there are no empty traces, but the trace interval is greater than half of the receiver interval. After resampling the *P*-*S* stacked data with optimum bin size of 33.3 m (Figure 4-14) into that with bin size of 25 m, the resulting section is shown in Figure 4-15. In order to quantitatively compare the difference between these two methods, the data in Figure 4-13 were subtracted by that in Figure 4-15. The result is shown in Figure 4-16, in which it is seen that the differences are very small. Hence in data with high S/N and events with small dip, the interpolation of empty bins using a conventional CMP bin size is equivalent to using an optimum bin size and resampling after stack.

The poststack migrated section for *P*-*S* stacked data shown in Figure 4-13 is shown in Figure 4-17. A single-pass phase-shift migration was applied to the *P*-*S* stacked data using a migration velocity of $(V_p V_s)^{1/2}$. Figure 4-18 is a migrated section of the stacked data shown in Figure 4-15, in which the *P*-*S* data were stacked with optimum bin size of 33.3 m, and then resampled into a bin size of 25 m. Later, the data in Figure 4-17 were subtracted from that in Figure 4-18, and the difference is shown in Figure 4-19. It is seen that the difference between the migrated results of these two different processing flows is negligible. For comparison, the *P*-*P* data were also processed, using a conventional processing flow. The same receiver-line stacked section as in Figure 4-13 is shown in Figure 4-20 and the migrated section for Figure 4-20 is shown in Figure 4-21.

Based on above results, it is clear that single-pass phase-shift migration indeed collapsed the diffractions on the stacked section, and poststack migration algorithm for *P*-*P* processing is suitable for *P*-*S* processing given a good stacked section and an accurate velocity estimation.

4.4.2 3-D converted-wave processing flow with prestack migration

As an alternative, a 3-D *P*-*S* processing flow with prestack migration was applied to the 3C-3D physical model data set. The processing flow is shown in Figure 4-22. Instead of using common conversion point (CCP) binning, velocity analysis based on time-shifted hyperbolic moveout, converted-wave NMO and stack by CCP, the new processing flow uses prestack migration and migration velocity analysis to yield the final image.

As discussed in Chapter 3, the prestack migration algorithm used in this processing flow is a Kirchhoff style time migration by equivalent offsets and common conversion scatter point (CCSP) gathers. The algorithm includes three steps, i.e. CCSP gathering, conventional NMO correction and stacking by CCSP gathers. The *P*-wave migration velocity $V_{p\ mig}$ is obtained from the velocity analysis on common scatter point (CSP) gathers by processing the *P*-*P* section, and the final *S*-wave migration velocity $V_{s\ mig}$ used in CCSP gathering is derived from conventional velocity analysis on CCSP gathers. The final *P*-*S* migration semblance velocity V_{sem} is used for the NMO correction.

In the CCSP gathering, which is the main step of the prestack migration, the equivalent offset bin size was chosen to be 15 m, and the maximum equivalent offset was 1040 m. Generally, the equivalent offset bin size should be less than half of the receiver interval to preserve some high frequency content. The final converted-wave migration semblance velocity V_{sem} can be directly used in NMO correction.

The example CCSP gather and its velocity spectrum is shown in Figure 3-7 in Chapter 3, using conventional velocity analysis tool. It is seen that *P*-*S* event, which is non-hyperbolic in conventional CCP gather appears to be hyperbolic in CCSP gather. This property is clear in the velocity spectrum, in which the velocity semblance is highly focused.

Figures 4-23 is an example section of *P*-*S* migrated data in receiver-line direction using the processing flow in Figure 4-22. In Figure 4-23, only the central part of the whole section is plotted. Comparison of Figures 4-23 and 4-17 shows that: (1). The prestack migrated section is better than the poststack migrated section in imaging the 3-D structure and collapsing diffractions; (2). The events in the *P*-*S* stacked and migrated sections (Figure 4-13 and Figure 4-17 respectively) are asymmetric. After prestack migration, this asymmetry seems to be removed; (3). Both approaches failed to image the flanks of the cavity.

4.5 Discussion

From the *P*-*S* stacked section shown in Figure 4-13, it is clear that processed 3-D *P*-*S* data did successfully yield good reflections corresponding to the 3-D model and the base of the plexiglas layer. Comparison of the *P*-*S* (Figure 4-13) and *P*-*P* (Figure 4-20) stacked sections showed a very good correspondence between *P*-*S* and *P*-*P* events. However, for both *P*-*P* and *P*-*S* sections, the processed sections did not yield good events corresponding to the flanks of the cavity. For converted-wave section, prestack migration (Figure 4-23) also failed to improve the image of the flanks. This is mainly because of spatial aliasing, especially at the lower parts of the flanks where the dip angles reach 90 degrees. Another possible reason is that the steep dips of the flanks are such that the conversion points can not cover the flanks. The third possibility is that if there is some converted-wave energy from these flanks, it is also very weak.

From the sections in Figures 4-20 and 4-21, it is seen that the *P*-*P* events are almost symmetrical in the receiver-line direction. This is expected since the model is symmetrical in this direction (Figure 4-1). However, the events in the *P*-*S* stacked and poststack migrated sections (Figure 4-13 and Figure 4-17 respectively) are asymmetric. This is probably because of the asymmetry of downgoing *P*-wave and upgoing *S*-wave raypaths and the asymmetric geometry in the data acquisition. This can be further demonstrated by the stacked section (Figure 4-23) after prestack migration, in which the asymmetry of the

image of the flanks disappears. As discussed in Chapter 3, after prestack migration, the asymmetry characters due to the ray paths and data acquisition geometry are removed. Therefore, we should be able to obtain an objective image of the reflectors.

This study has shown that physical seismic modeling is a very useful way to evaluate experimental design and data processing algorithms for 3-D *P*-*S* data. A 3C-3D dataset over a 3-D model was collected, which can not only be helpful for the development of processing flow and the design of the survey, but also be used to test other processing algorithms.

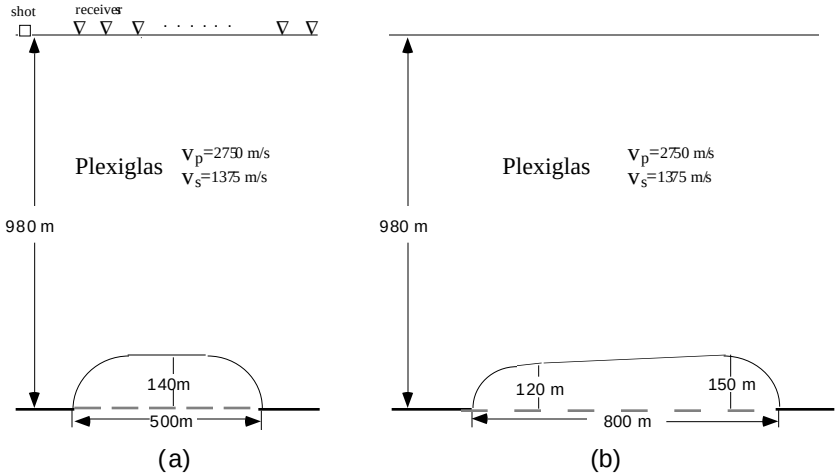

FIG. 4-1. Cross-sections of the model in receiver-line (a) and shot-line (b) directions across the center of the model.

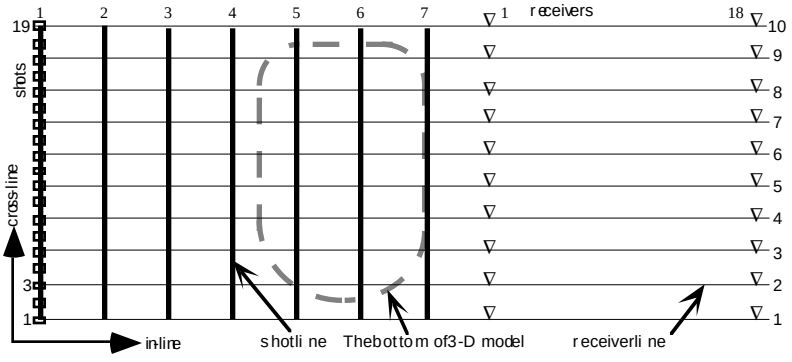

FIG. 4-2. Plan view of model showing acquisition geometry. Receiver locations are indicated for shot line #7.

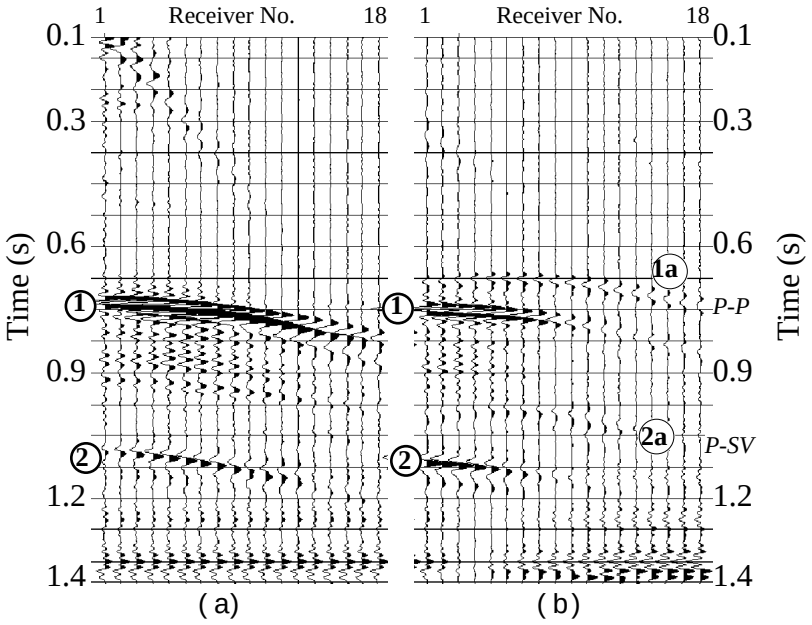

FIG. 4-3. Example of data collected for in-line receiver.
(a) Shot station 9, shot line 1 and receiver line 5
(b) Shot station 9, shot line 3 and receiver line 5

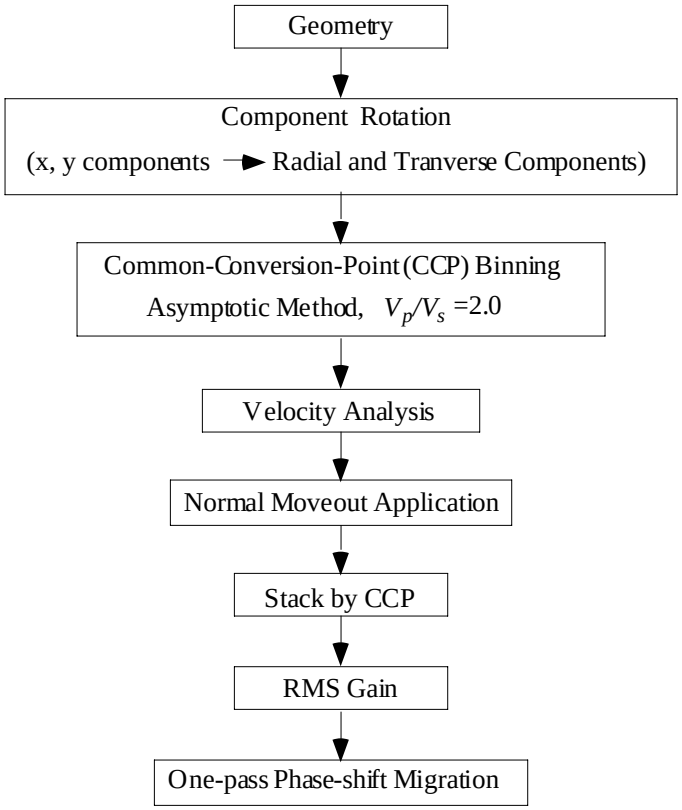

FIG. 4-4. Flow chart for 3-D isotropic *P-S* processing.

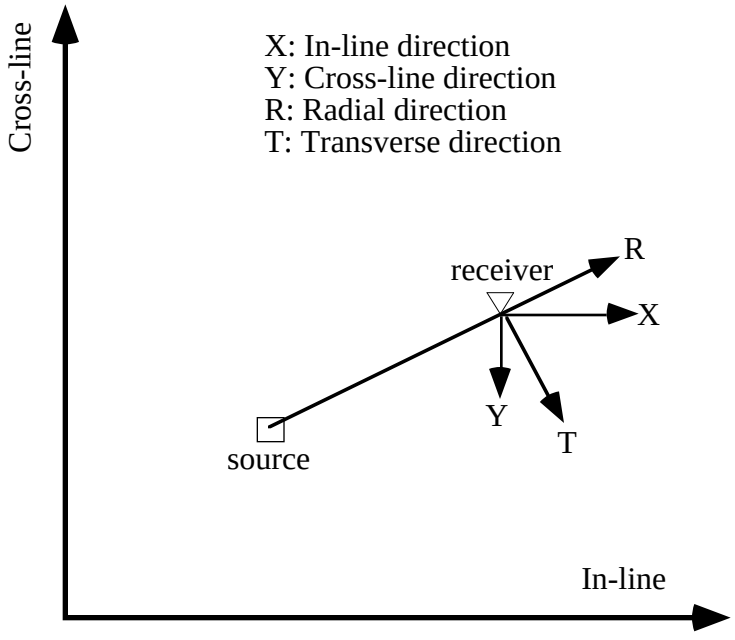

FIG. 4-5. Plan view of component rotation.

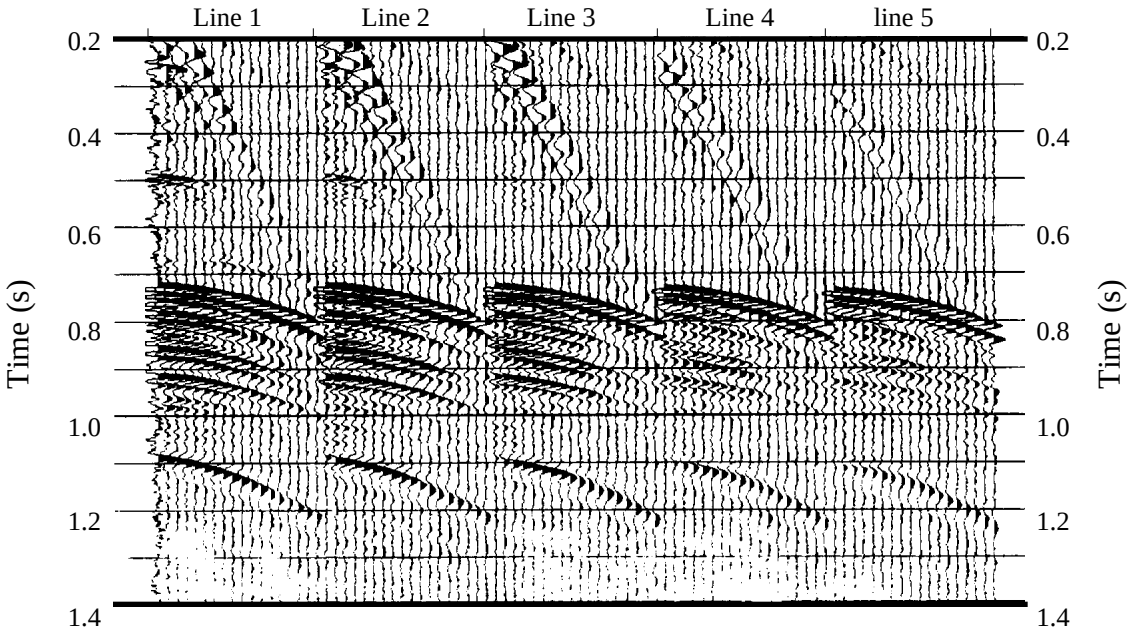

FIG. 4-6a. Example of In-line component *P-S* data.
Shot was at station #1 in shot line 1.

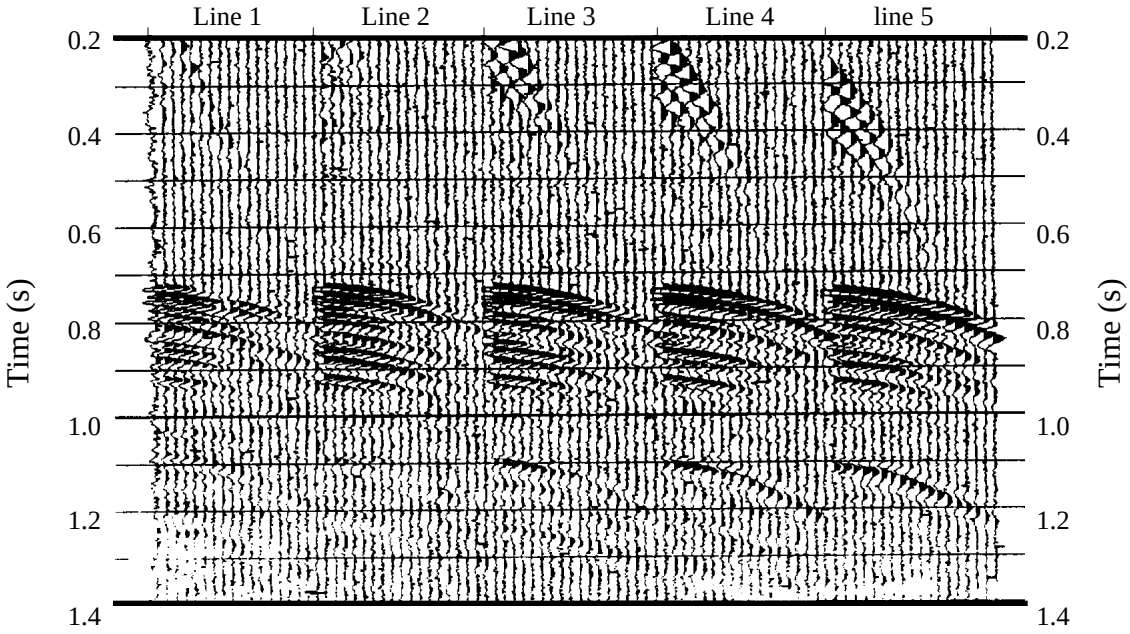

FIG. 4-6b. Example of Cross-line component *P-S* data.
Shot was at station #1 in shot line 1.

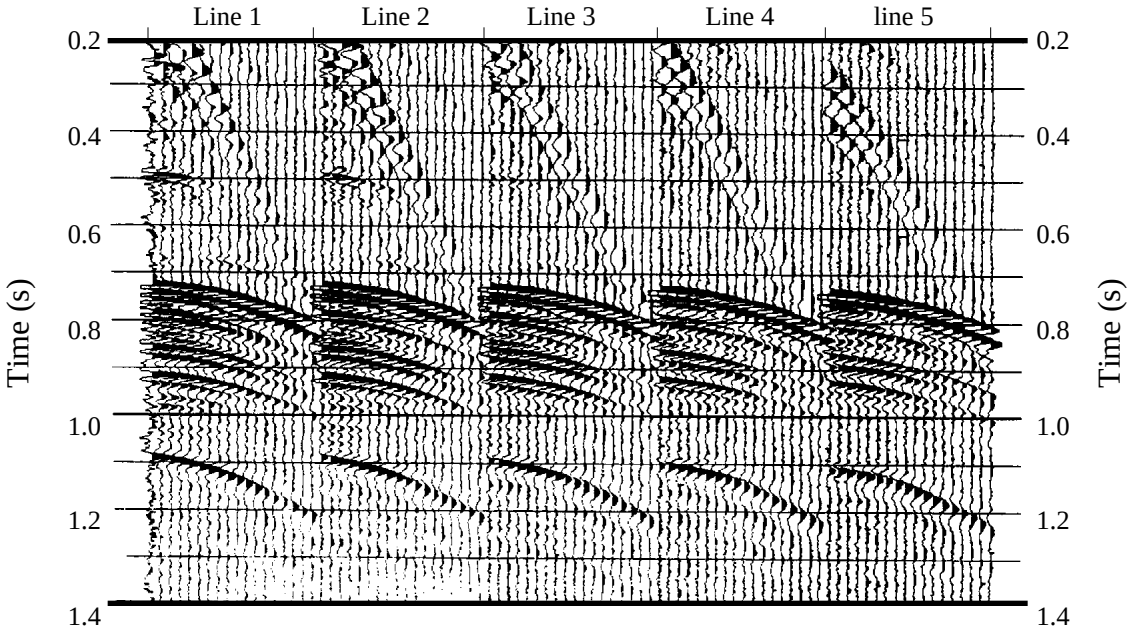

FIG. 4-7a. Example of radial component *P-S* data.
Shot was at station #1 in shot line 1.

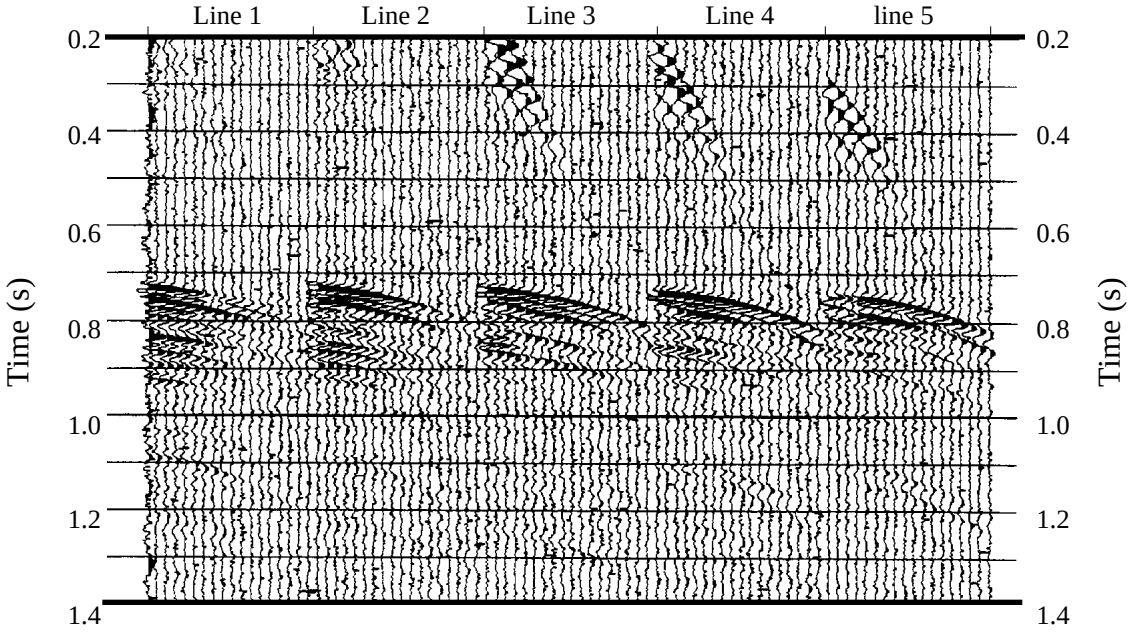

FIG. 4-7b. Example of transverse component *P-S* data.
Shot was at station #1 in shot line 1.

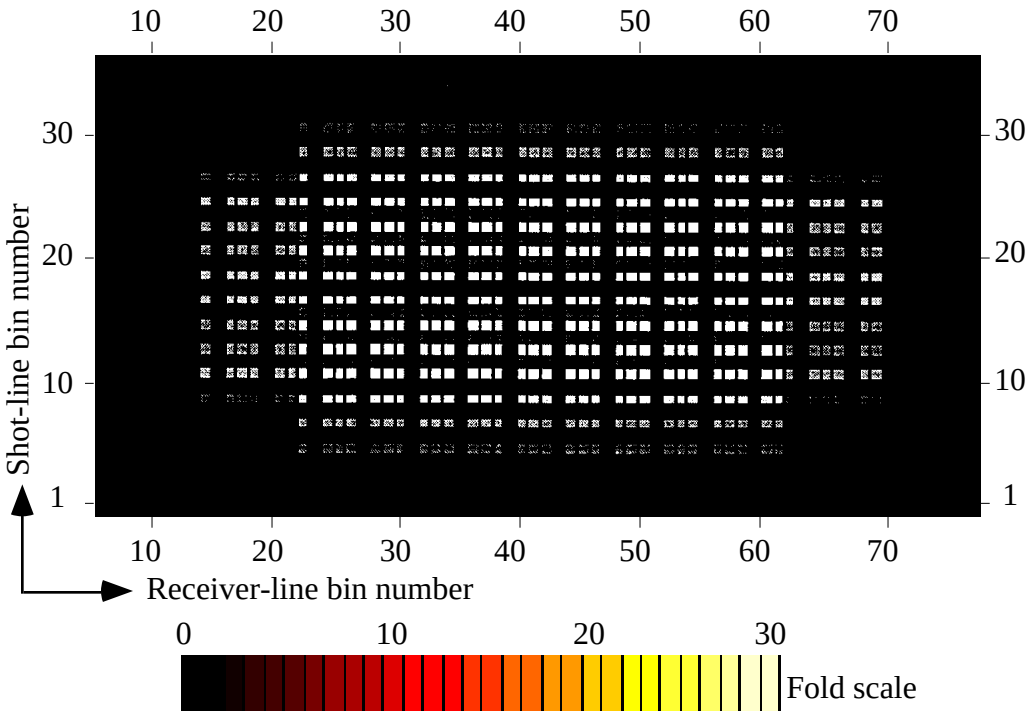

FIG. 4-8. Fold map of asymptotic common conversion point binning with bin size 25 m.

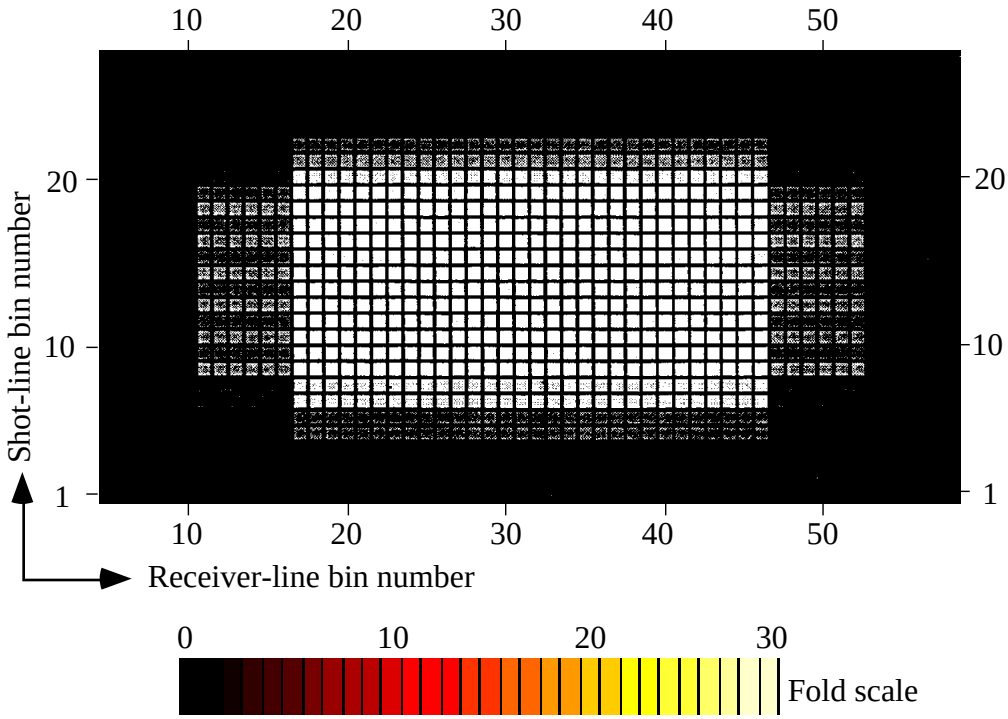

FIG. 4-9. Fold map of asymptotic common conversion point binning with bin size 33.3 m.

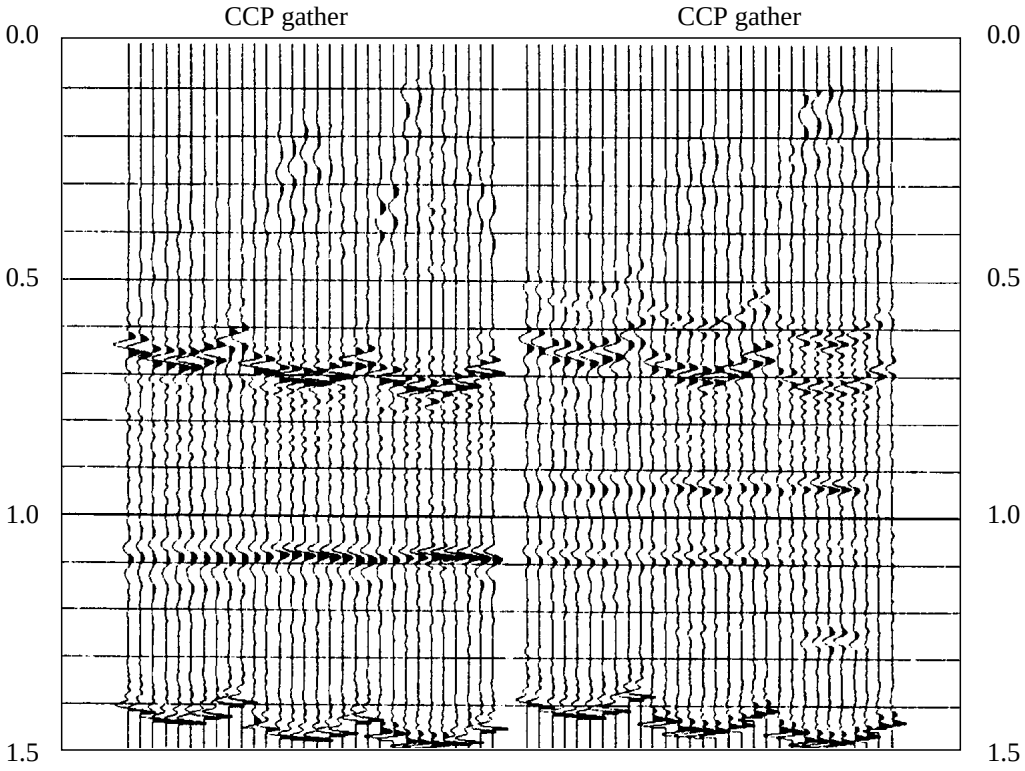

FIG. 4-10. Example of *P-S* normal moveout correction using standard hyperbolic equation

FIG. 4-11. Example of *P-S* normal moveout correction using time-shifted hyperbolic equation

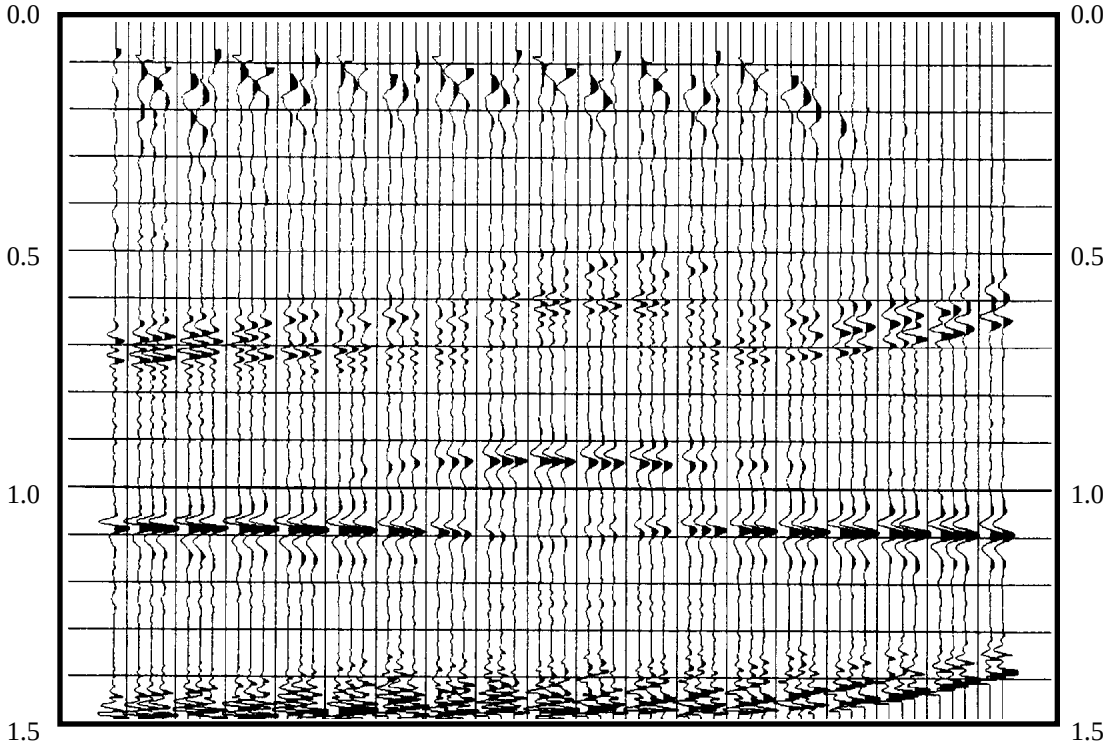

FIG. 4-12. Example section of *P-S* stacked data in receiver-line direction with bin size 25 m, without interpolation of empty traces

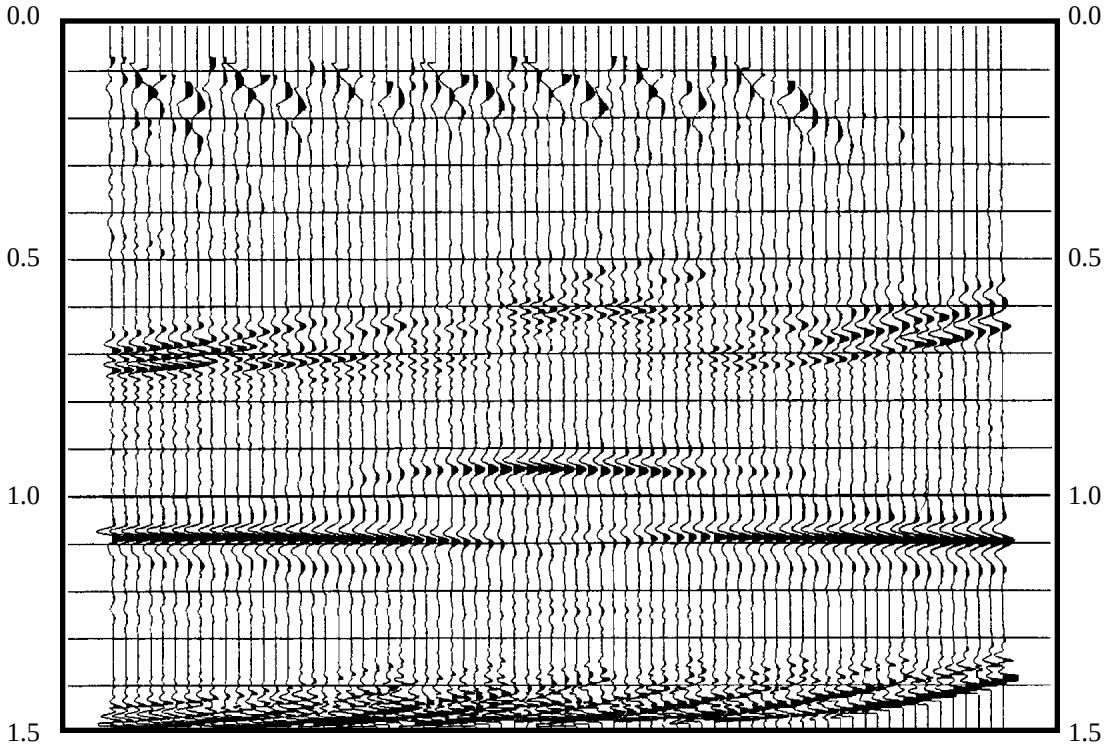

FIG. 4-13. Example section of *P-S* stacked data in receiver-line direction with bin size 25 m after interpolation of the empty traces

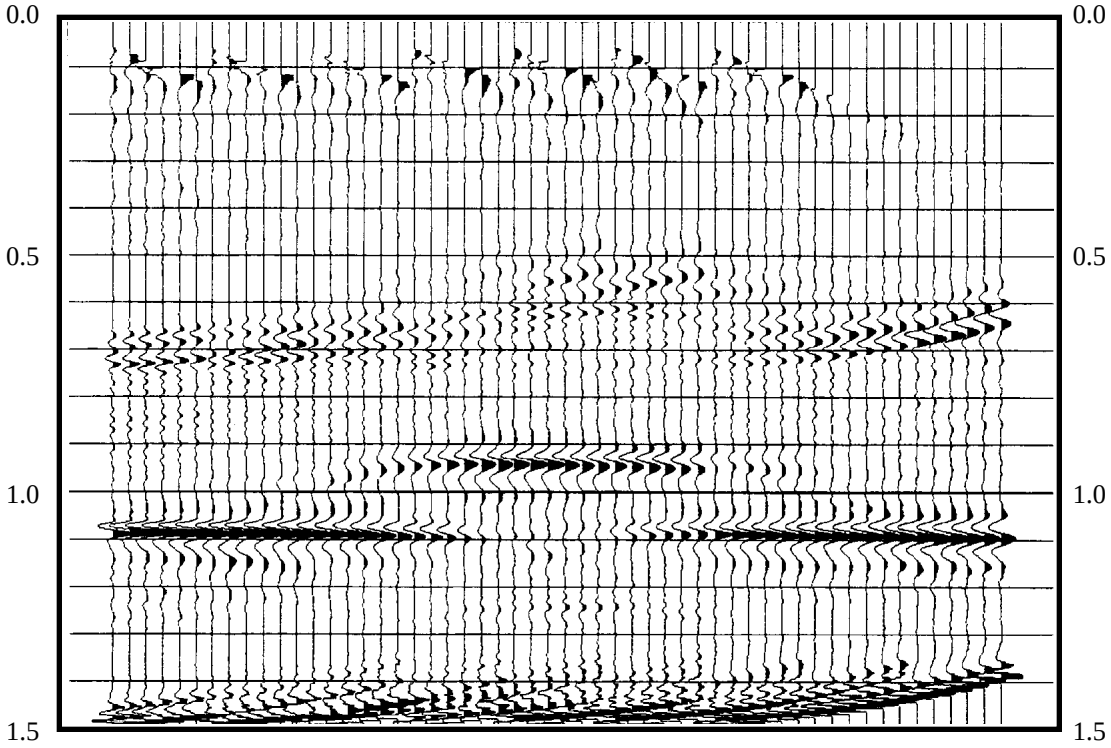

FIG. 4-14. Example section of *P-S* stacked data in receiver-line direction with optimum bin size 33.3 m

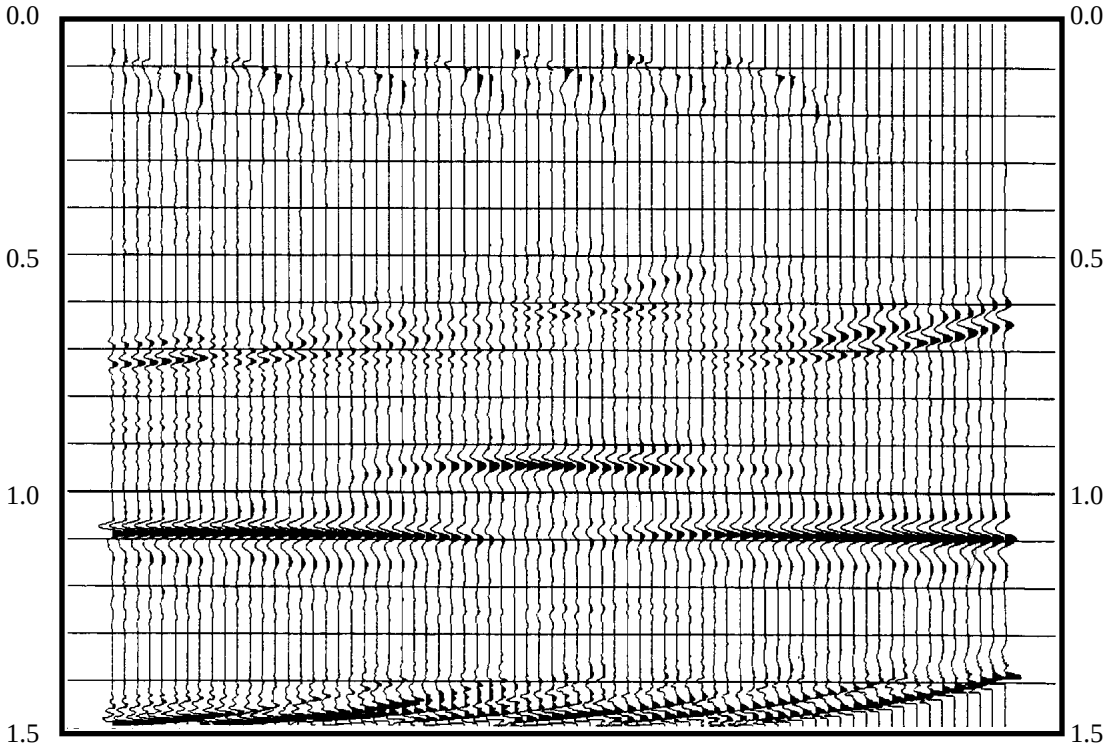

FIG. 4-15. Example section of *P-S* stacked data in receiver-line direction with optimum bin size 33.3 m, then resample the data with bin size 25 m

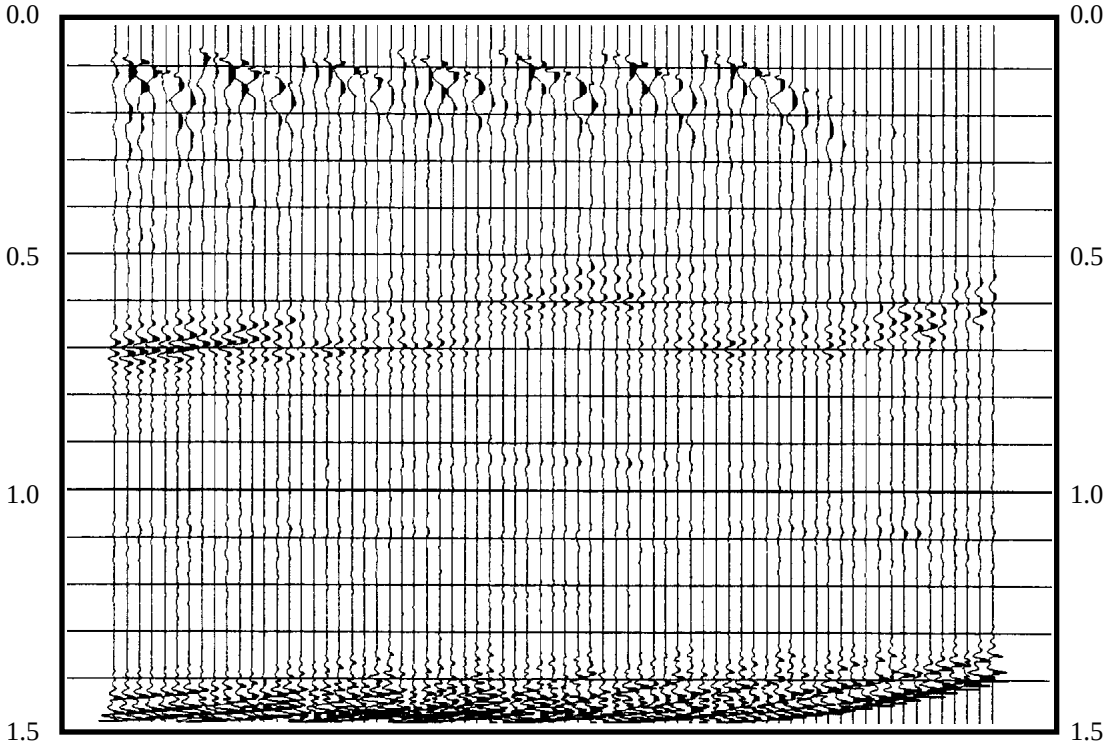

FIG. 4-16. The subtraction between Figure 4-15 and Figure 4-13

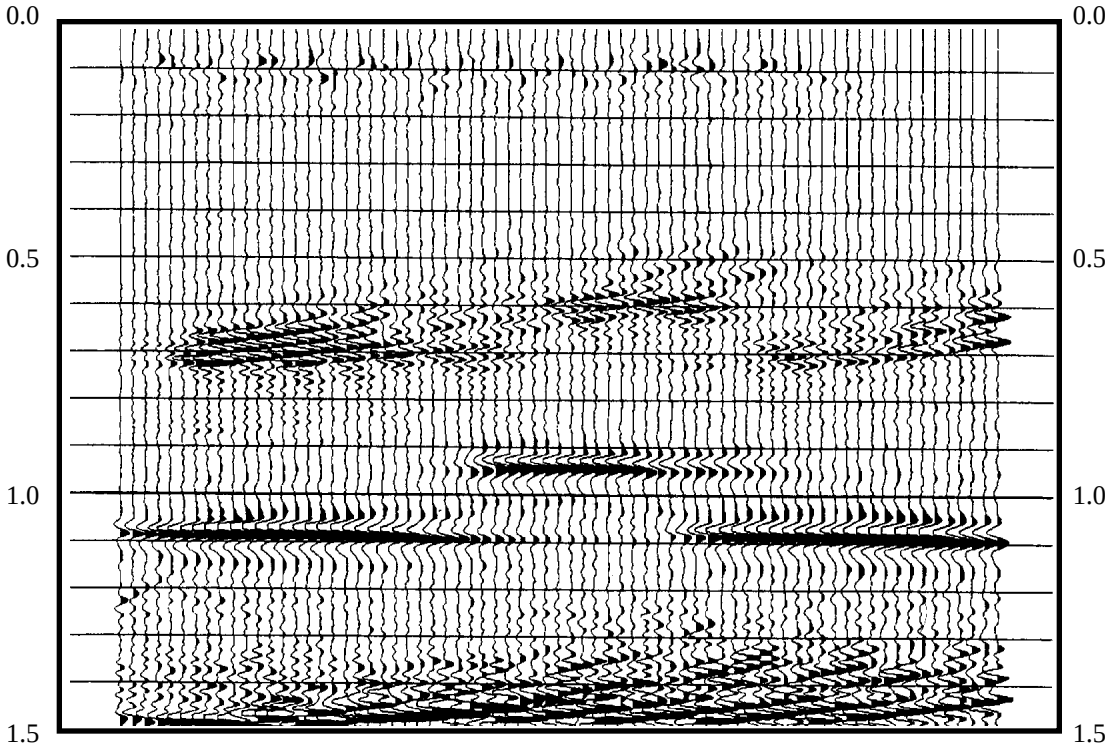

FIG. 4-17. Example section of *P-S* migrated data in receiver-line direction after interpolation of the empty traces

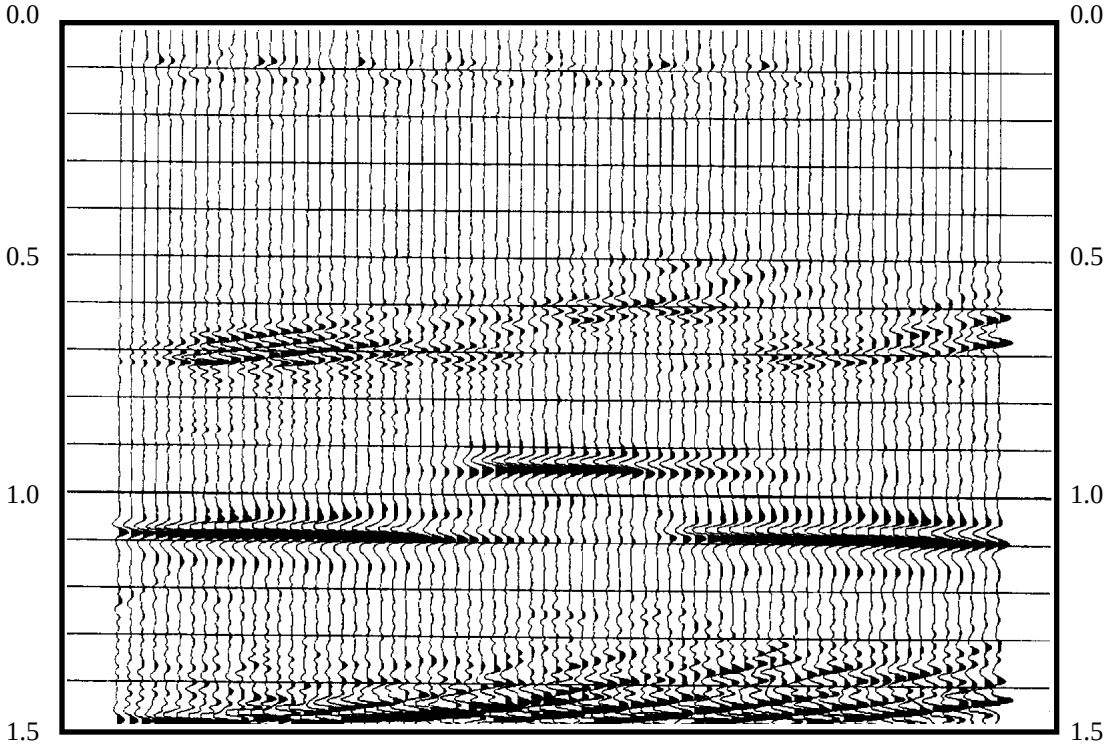

FIG. 4-18. Example section of *P-S* migrated data in receiver-line direction with optimum bin size 33.3 m, after interpolating the data with bin size 25 m and migrating this data set

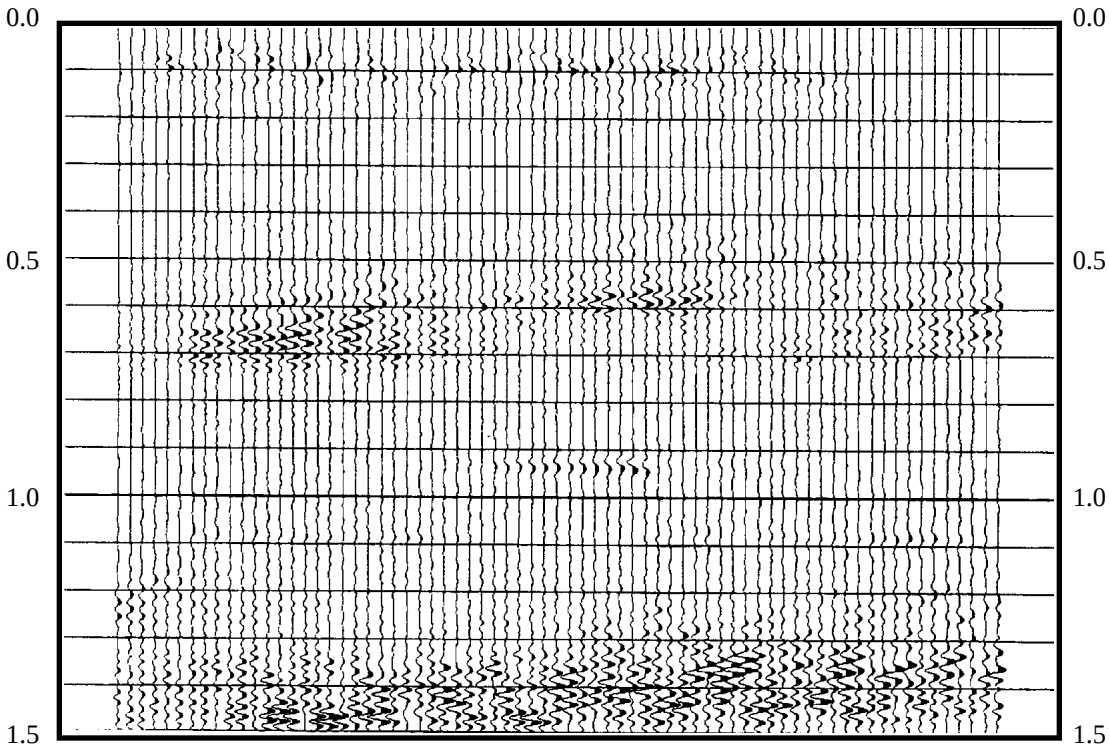

FIG. 4-19. The subtraction between Figure 4-18 and Figure 4-17

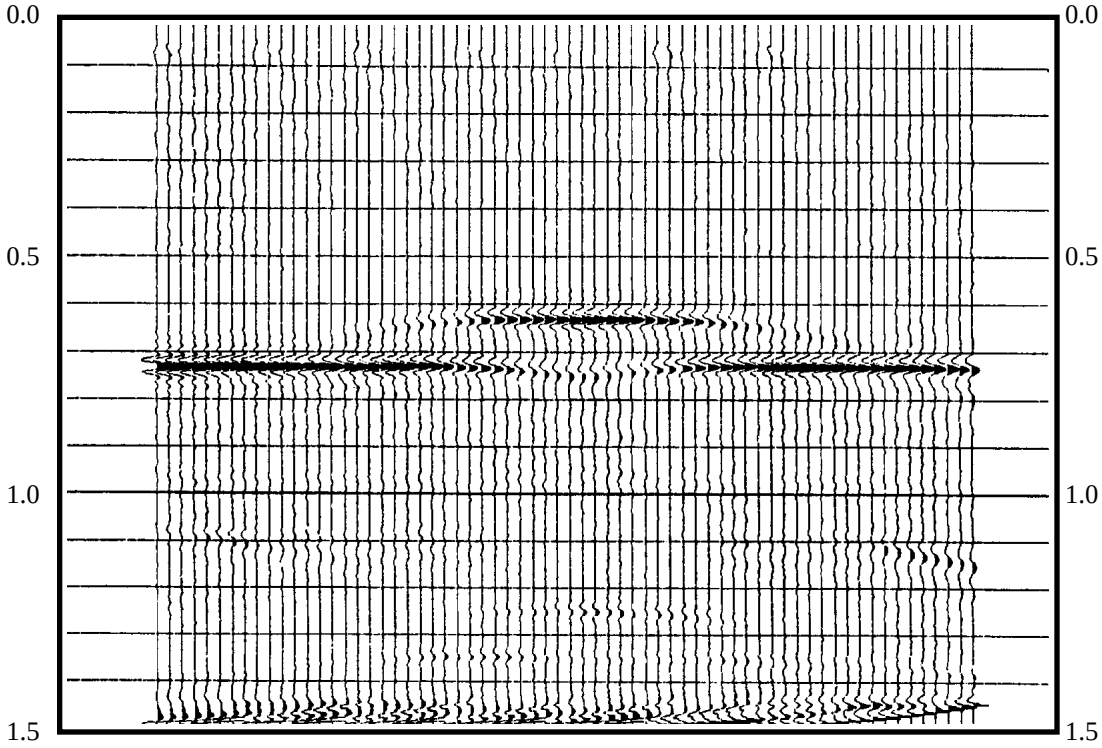

FIG. 4-20. Example section of *P-P* stacked data in receiver-line direction with bin size of 25 m

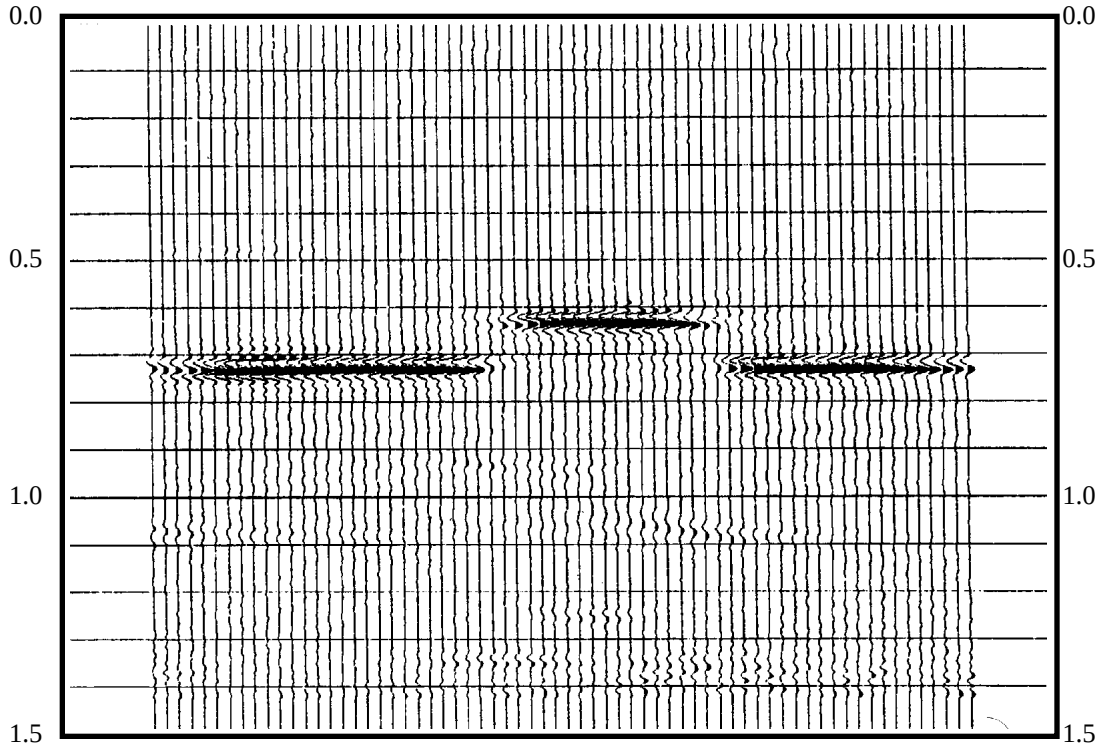

FIG. 4-21. Example section of *P-P* migrated data in receiver-line direction with bin size of 25 m

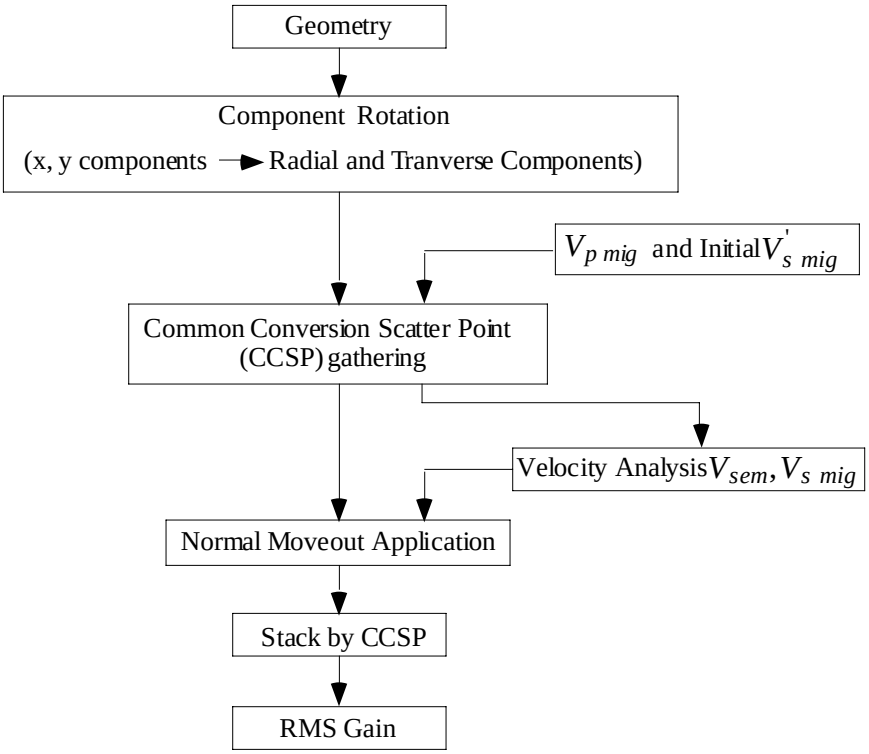

FIG. 4-22. Processing flow for 3-D isotropic *P*-*S* data with converted-wave presatck time migration.

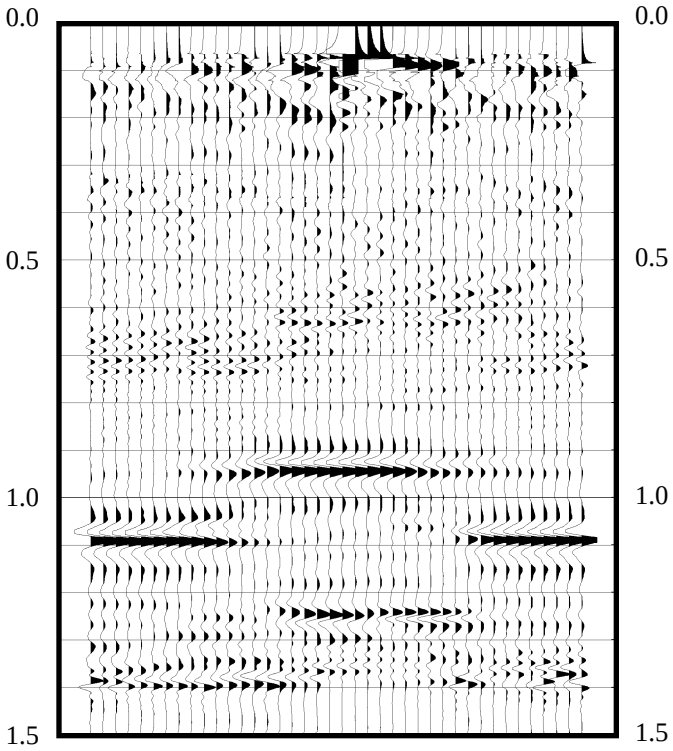

FIG. 4-23 . Example stacked section of *P-S* prestack migrated data in receiver-line direction.

Chapter 5 - Conclusions

The main objectives of this thesis work are to provide some insight into the 3-D converted-wave processing, to develop algorithms for converted-wave processes and to simplify the 3-D converted-wave processing procedures.

5.1 Fast 3-D *P-S* depth-variant CCP binning

(1) In order to improve the stacked section of the converted-wave data, whether for 2-D or 3-D, depth-variant common conversion point stacking is necessary. The fast 3-D converted-wave depth-variant CCP stacking method described in Chapter 2 provides an efficient and easy way to achieve this goal.

(2) The implementation gains considerable speed through the mapping of samples in blocks instead of individually, while not losing the accuracy of conventional depth-variant binning.

(3) With reasonable constraints on velocities and their ratio, the algorithm was modified to deal with depth-variant velocity model.

(4) A 3-D converted-wave numerical model has demonstrated the feasibility of the new method.

5.2 Prestack time migration and migration velocity analysis

(1) The calculation of the equivalent offset for *P-S* waves is proved to be more complex than that for conventional *P-P* waves, but an explicit expression can still be obtained. The equivalent offset is not only depth-dependent but also velocity-dependent. The depth-dependent characteristic of the equivalent offset becomes significant when the CCSP surface location is close to the source or receiver. Velocity error has an effect on equivalent offset, especially at early times, but with increasing time or depth, this effect becomes negligible.

(2) As the most important step of this new algorithm, the practical computation of CCSP gathering greatly speeds up the algorithm by moving blocks of data into equivalent offset bins. By incorporating the front mute, the start time for the calculation of equivalent offset increases with the increasing equivalent offset. This can further reduce the computation time.

(3) In CCSP gathers, the relationship between the two-way travel time and equivalent offset is hyperbolic. This makes conventional *P-P* velocity analysis suitable to *P-S* velocity analysis. The iterative procedure proposed in this study is practical, because the CCSP gathering is fast and flexible. This new approach provides a convenient but powerful way to perform migration velocity analysis for converted-waves.

(4) The algorithm is very stable. The CCSP gather and its velocity analysis are fairly insensitive to the velocity error, the velocity analysis is convergent and the convergence speed is fast. When the velocity error is as large as 40%, an accurate velocity function can still be obtained by a couple of iterations.

(5) The 3-D numerical model and 2-D field data examples demonstrated the feasibility of the new algorithm. Prestack migration by equivalent offsets and CCSP gathers indeed collapses the diffractions and correctly migrates the dipping seismic reflections to the right spatial locations. It is proved that this prestack migration and migration velocity analysis algorithm can simplify the *P-S* processing, as well as improve the image of the *P-S* reflections. The field data example shows not only the improvement of signal-to-noise ratio but also the improvement of velocity analysis and the continuity of the seismic events, while not reducing the bandwidth.

(6) The numerical model examples also helps to understand the effect of 3C-3D data acquisition geometry on the prestack migration result. For converted-wave processing, among the other factors, the actual fold, offset and azimuth distributions might be quite different from the nominal fold, offset and azimuth distributions due to the different mute pattern from *P-P* waves. Low fold, bad offset and azimuth distributions may result in a poor image after prestack migration, so special consideration should be taken about the effect of these factors on converted-wave prestack migration in the design of the 3C-3D.

5.3 3C-3D physical modeling

(1) Component rotation successfully transferred the *P-S* wave energy distributed in both in-line and cross-line components into radial component in the case of isotropic medium. Time-shifted hyperbolic equation with effective *P-S* stacking velocity for *P-S* NMO correction improved the result of *P-S* NMO application, even when the offset-to-depth ratio is not large.

(2) Asymptotic common conversion point (CCP) binning proved to be a fast binning method and the horizontal position difference from the true conversion point can be small, when the depth of interest is large compared to the offset range. Compared with CCP binning with conventional bin dimensions, the CCP binning method using optimum bin size made the fold distribution more even and removed the empty bins. The interpolation of empty bins using a conventional CMP bin size was found be equivalent to using an optimum bin size and resampling after stack.

(3) Because of the asymmetry of the *P-S* raypaths and the particular design of this survey, converted-wave events in the receiver-line direction in both stacked and migrated sections were found to be asymmetric over the flanks of the cavity, although the model in this direction is symmetrical. After prestack migration, this asymmetry was eliminated.

(4) The application of 3-D poststack migration made a significant improvement to the image of the cavity, and standard poststack migration using *P-S* migration velocities gave good stacked section.

(5) 3-D *P-S* processing flow with prestack migration also improved the image of the *P-S* section. With the application of prestack migration, the asymmetry of the image of the cavity was removed.

5.4 Future work

For the converted-wave prestack migration and migration velocity analysis by CCSP gathers and equivalent offsets, issues of amplitude and phase need to be addressed and properly incorporated into the CCSP gathering. This would help to preserve the amplitude information after prestack migration. More work is needed to be done about the effect of offset, azimuth and fold distribution on the results of prestack migration and

migration velocity analysis. In the image of 3-D complex structure using converted-wave, the energy beyond critical angle might strongly affect the migration result, hence further work on this topic would assist in improving the image of the 3-D structure.

A 3-D physical model with depth-variant *P*-wave and *S*-wave velocities and 3-D structure of different dipping angles would be more effective to evaluate same processing algorithms and processing flow. The study of imaging 3-D structure using converted-wave would provide a more effective use of 3-D converted-wave in the area with complex structure.

References

Bancroft, J.C., Geiger H.D., Wang, S., and Foltinek, D.S, 1995, Prestack migration by equivalent offsets and CSP gathers: an update: CREWES project research report, **7**, 23-1-23-29.

Bancroft, J.C., Geiger H.D., Foltinek, D.S., and Wang, S., 1994, Prestack migration by equivalent offsets and CSP gathers: CREWES project research report, **6**, 27-1-27-18.

Bancroft, J.C., and Wang, S., 1994, Converted-wave prestack migration and velocity analysis by equivalent offsets and CCP gathers: CREWES project research report, **6**, 28-1-28-7.

Buchanan, R, 1992, Three-dimensional seismic: The application of new technology to oil field development: Bull. Amer. Assoc. Petrol Geol., **76**, 1855-56.

Cary, P.W., 1994, 3-D converted-wave seismic processing: CREWES project research report, v.**6**, 31-1-31-10.

Chen, How-Wei, and McMechan, G.A., 1993, 3-D physical modeling of seismic common-source data volumes: Geophysics, **58**, 121-133.

Chon, Y.T., and Turpening, W.R., 1990, Complex salt and subsalt imaging: A seismic physical model study in 2-D and 3-D: 60th SEG, Expanded Abstracts, 1569-1571.

Dankbaar, J.W.M., 1985, Separation of P and S waves: Geophys. Prosp., **33**, 970-986.

Deregowski, S. M., 1982, Dip moveout and reflector point dispersal: Geophysical Prospecting, **30**, 318-322.

Eaton, D.W.S., and Stewart, R.R., 1989, Aspects of seismic imaging *P-SV* converted waves: CREWES project research report, **1**, 68-92.

Eaton, D.W.S., Slotboom, R.T., Stewart, R.R., and Lawton, D.C., 1990, Depth variant converted wave stacking: 60th SEG, Expanded Abstract, 1107-1110.

Eaton, D.W.S., and Lawton, D.C., 1990, *P-SV* stacking charts and binning periodicity: CREWES Research Project, **2**, 36-44.

Eaton, D.W.S. and Stewart, R.R., 1991, The Fresnel zone for *P-S* wave: Geophysics, **56**, 360-364

Ebrom, D.A., Tatham, R.H., Sekharan, K.K., McDonald, J.A., and Gardner, G.H.F., 1990, Hyperbolic travel time analysis of first arrivals in an azimuthally anisotropic medium: A physical modeling study: Geophysics, **55**, 185-191.

Ferber, R.-G., 1994, Migration to multiple offset and velocity analysis: Geophysical Prospecting, **42**, 99-112.

Forel, D., and Gardner, G.H.F., 1988, A three-dimensional perspective on two-dimensional dip moveout: Geophysics, **53**, 604-610.

Gardner, G.H.F., Wang, S.Y., and Randazzo, S., 1987, Example of DMO for 3-D data over 3-D structure: 57th SEG, Expanded Abstracts, 309-312.

Gardner, G.H.F., Purnell, G.W., and Cariou, H., 1989, Velocity analysis after migration: 59th SEG, Expanded Abstracts, 555-558.

Gardner, G.H.F., and Forel, D., 1990, Amplitude preservation equations for dip moveout: Geophysics, **55**, 485-487.

Harrison, M.P., 1992, Processing of *P-SV* surface-seismic data: Anisotropy analysis, dip moveout, and migration. Ph.D. thesis, The University of Calgary.

Kuo, J. T., and Dai, T., 1984, Kirchhoff elastic wave migration for the case of noncoincident source and receiver: Geophysics, **49**, 1223-1238.

Lane, M.C., and Lawton, D.C., 1993, 3-D converted wave asymptotic binning: CREWES project research report, **5**, 29-1-29-5.

Lawton, D.C., Cheadle, S.P., Gallant, E.V., and Bertram, M.B., 1989, Elastic physical seismic modeling: CREWES project research report, **1**, 273-276.

Lawton, D.C., 1993, Optimum bin size for converted-wave 3-D asymptotic mapping: CREWES project research report, **5**, 28-1-28-14.

Lawton, D.C., Wang, S., 1994, Converted-wave (*P-SV*) processing and interpretation for 3-D surveys: A physical modelling example: SEG International Exposition & 64th Annual Meeting, Los Angeles, U.S.A., Expanded Abstracts, 1445-1448.

Miller, S.L.M., Harrison, M.P., Szata, K.J., and Stewart, R.R., 1993, Processing and preliminary interpretation of multicomponent seismic data from Lousana, Alberta: CREWES Research Report, **5**, 16.1-16.17

Miller, S.L.M., Harrison, M.P., Lawton, D.C., Stewart, R.R., and Szata, K.J, 1994, Analysis of *P-P* and *P-S* seismic data from Lousana, Alberta: CREWES Research Report, **6**, 7.1-16.24

Schafer, A.W., 1992, A comparison of converted-wave binning methods using a synthetic model of the Highwood structure, Alberta: CREWES Research Project, **4**, 9, 1-9.

Slotboom, R.T., and Lawton, D.C., 1989, Depth-variant mapping and moveout correction of converted-wave data: CREWES project research report, **1**, 55-67.

Slotboom, R.T., Eaton, D.W., and Lawton, D.C., 1990, Improving converted-wave (*P-S*) moveout estimation: CREWES project research report, **2**, 80-88.

Stolt, R.H., and Benson, A.H., 1986, Seismic migration, Theory and Practice: Geophysical Press.

Sumner, B., and Bleistein, N., 1988, Prestack elastic Kirchhoff migration and parameter estimation: 58th SEG, Expanded Abstracts, 963-965.

Tatham, R.H., and Stoffa, P.L., 1976, Vp/Vs - A potential hydrocarbon indicator: Geophysics, **41**, 837-849.

Tatham, R.H., 1982, Vp/Vs and lithology: Geophysics, **47**, 336-344.

Tatham, R.H., Goolsbee, D.V., Massell, W.F., and Nelson, H.R., 1983, Seismic shear-wave observations in a physical model experiment: Geophysics, **48**, 688-701.

Tatham, R.H., and Goolsbee, D.V., 1984, Separation of *S*-wave and *P*-wave reflections offshore western Florida: Geophysics, **49**, 493-508.

Tatham, R.H., and Stewart, R.R., 1993, Present status and future directions of shear-wave seismology in exploration: CREWES project research report, **5**, 1-1-1-22.

Taylor, G.G., 1989, The point of P-S mode-converted reflection: An exact determination: Geophysics, **54**, 1060-1063.

Tessmer, G., and Behle, A., 1988, Common reflection point data-stacking technique for converted waves: Geophys. Prosp., **36**, 671-688.

Tessmer, G., Krajewski, P., Fertig, J., and Behle, A., 1990, Processing of PS-reflection data applying a common conversion-point technique: Geophysical Prospecting, **38**, 267-286.

Wang, S., Bancroft, J.C., Lawton. D.C. and Foltinek, D.S., 1995, Converted-wave (*P-SV*) prestack migration and migration velocity analysis: CREWES project research report, **7**, 27-1-27-21

Zhong, B., Zhou, X., Liu, X., and Jiang, Y., 1994, One step common conversion point stacking technique for *P-SV* reflection data: 64th SEG, Expanded Abstracts, 1453-1456.